CRANFIELD UNIVERSITY

Elio Fonti

MEASUREMENTS OF AIRCRAFT WAKE VORTICES IN GROUND PROXIMITY WITHIN AN ATMOSPHERIC BOUNDARY LAYER WIND TUNNEL

SCHOOL OF ENGINEERING

MSc THESIS

Academic Year: 2009-10

Supervisors: K.P. Garry, N.J. Lawson

CRANFIELD UNIVERSITY

SCHOOL OF ENGINEERING

MSc by Research

MSc Thesis

Academic Year: 2009-10

Elio Fonti

Measurements of Aircraft Wake Vortices in Ground Proximity within an Atmospheric Boundary Layer Wind Tunnel

Supervisors: K.P. Garry, N.J. Lawson

This thesis is submitted in partial fulfilment of the requirements
for the degree of Master of Science.

Abstract

The vortex wake characteristics of aircraft during landing and take-off are of interest in connection with both the safety of following aircraft penetrating the vortex and the dispersion of engine exhaust plumes. A series of measurements were carried out in an Atmospheric Boundary Layer Wind Tunnel (ABLWT) to identify and characterise both the mean and turbulent flow field of a pair of wake vortices in ground proximity. The ABLWT simulation at 1:200th scale utilised a flat plate delta plan-form wing to produce a wake vortex system with an initial vortex core separation (b_0) consistent with that expected for the DLR VFW614 ATTAS aircraft during the final stages of the approach and flare prior to landing in order to aid possible future full scale validation. Evaluation of the mean flow field was obtained in vertical planes downstream of the model $0.18B_s < x < 7.48B_s$ (B_s is the wing span) using a traversing 5-hole pressure probe. Vortex trajectory, circulation decay, vorticity decay and core radius evolution were tracked at wing heights $0.93B_s < H < 2.24B_s$ within the wind tunnel working section, showing the ground proximity effect on the vortex system. The vortices were seen to sink behind the wing and diverge moving downstream, as expected. The rate of descent was shown to decrease as the wing model approaches the ground. The circulation was fitted to a straight line with enough accuracy for all the wing heights investigated. An inviscid model for the prediction of the trajectory of a vortex pair was developed. It uses an infinite vortex sheet to simulate the interaction between the vortices and the ground when these are in the ground effect region. The experimental results were compared to the model showing good agreement. Measurements of the instantaneous flow field were acquired by means of a Stereo Particle Image Velocimetry (SPIV) system and were used to investigate the effect of turbulence on the vortex system. The mean field was compared to the fluctuating field showing the random and intermittent nature of the turbulence. Turbulence intensity, Reynolds stresses, spatial velocity correlations and correlation lengths were calculated and discussed. However further work is needed to acquire a more comprehensive set of PIV data in the ABLWT to draw stronger conclusions.

Table of Content

List of Figures

List of Tables

Notation

a	core radius
A_B	characteristic area Greene's model
A_{ij}	deviatoric Reynolds stress tensor
B	wing span
b	vortex separation
c	wing chord length
C	Sarpkaya's model constant (*C=0.45*)
C_D	drag coefficient Greene's model
Cp_{static}	static pressure coefficient
Cp_{total}	total pressure coefficient
Cp_{θ}	pitch coefficient
Cp_{φ}	yaw coefficient
d	separation between a pair of co-rotating vortices
D (D_x, D_y, D_z)	physical particle displacement
d (d_x, d_y, d_z)	particle image displacement
e	ratio *tanα/tanδ* Smith's model
f	scale factor (*1/200*)
f_c	Coriolis force parameter ($f_c = 2\Omega \sin \phi$)
F_c	Coriolis force
g	acceleration of gravity
h	atmospheric boundary layer height
H	wing model height
I (I_u, I_v,I_w)	turbulence intensity
J	angular momentum
k	turbulent kinetic energy
k_a	Von-Karman constant
L	lift generated by a generic aircraft
L'	lift per unit span
L_B	characteristic length Greene's model
L_T	turbulence correlation length

M	magnification factor
n	Vatistas model coefficient
N	Brunt–Väisälä frequency
N^*	non-dimensional Brunt–Väisälä frequency
p_0	centre hole pressure
p_1	bottom hole pressure
p_2	right hole pressure
p_3	top hole pressure
p_4	left hole pressure
q	turbulence parameter Greene's model
Q^*	non-dimensional turbulence parameter Greene's model
r	radial distance from the vortex centre
Re	Reynolds number
Re_L	turbulence Reynolds number
R_{ij}	two-point spatial velocity correlation
$R^{(t)}_{ij}$	temporal velocity correlation
R^T_{ij}	Reynolds stress tensor
s_s	wing model thickness
$\bar{S}_{ij}$	mean rate of strain
t	time
T	non-dimensional time
T_e	evaluation time
T_G	time vortices enter in ground effect region
T_τ	correlation time
T^*	vortex lifespan
u_*	skin friction velocity
u_{ref}	reference velocity for time-space conversion
$\mathbf{V}(u, v, w)$	velocity vector
V_z	velocity at height z within the ABL
V_0	vortex initial descent speed
V_{10}	velocity at *10 m* height within the full scale ABL
$V_{0.05}$	velocity at *0.05 m* height within the scale model of the ABL

$V_{0.107}$	velocity at *0.107 m* height within the scale model of the ABL
V_{θ}	vortex tangential velocity
$v_{sheet\text{-}vort1}$	lateral velocity induced by the vortex sheet on the right vortex
w_{12}	velocity induced by the right vortex on the left vortex
w_{21}	velocity induced by the left vortex on the right vortex
w_G	vertical velocity component induced over the ground
$w_{vort1\text{-}G}$	vertical velocity induced by the right vortex on the ground
$w_{vort2\text{-}G}$	vertical velocity induced by the left vortex on the ground
$w_{sheet\text{-}G}$	vertical velocity induced by the vortex sheet on the ground
$w_{sheet\text{-}vort1}$	vertical velocity induced by the vortex sheet on the right vortex
u, v, w	velocity components along x, y and z
x, y, z	wing reference system
x_G, y_G, z_G	ground reference system
x_v, y_v, z_v	vortex reference system
X, Y, Z	non-dimensional wing reference system
X_G, Y_G, Z_G	non-dimensional ground reference system
X_v, Y_v, Z_v	non-dimensional vortex reference system
y_c, z_c	vortex centre coordinates
z_0	roughness parameter

Greek symbols

α	angle of attack
β	wing model bevelling angle
γ	vortex sheet intensity per unit of length
Γ	vortex circulation
δ	delta wing half apex angle
ε	turbulence dissipation rate
ε^*	turbulence parameter
θ	pitch angle
ϑ	angle between normal to the ground and radial distance, see [4.1.1]
Θ	potential temperature
Λ	delta wing sweep angle

μ	dynamic viscosity
ν	cinematic viscosity
ν_T	turbulent cinematic viscosity
ρ	fluid density
ρ_{ij}	non-dimensional two-point velocity correlation
$\rho_{ij}^{(t)}$	non-dimensional temporal velocity correlation
σ	standard deviation
τ	shear stress
τ_0	shear stress at the ground
φ	yaw angle
ϕ	local latitude
$\boldsymbol{\omega}$ $(\omega_x, \omega_y, \omega_z)$	vorticity
Ω	angular velocity of the Earth

Subscripts

0	initial value
ATTAS	ATTAS aircraft value
exp	experimental data
fitting	fitting function
s	scaled value
∞	free-stream value

Superscripts

$(\bar{\ })$	mean value with respect to time
$(')$	on velocity components or pressure means turbulent fluctuation

Abbreviations

ABL	Atmospheric Boundary Layer
AIM	Advanced In-flight Measurements
ATTAS	Advanced Technologies Testing Aircraft System
ESDU	Engineering Science Data Unit
PBL	Planetary Boundary Layer

PIV	Particle Image Velocimetry
PTV	Particle Tracking Velocimetry
SL	Surface Layer
SPIV	Stereo Particle Image Velocimetry
TKE	Turbulent kinetic energy

Introduction

In the past thirty years many theoretical and experimental studies, together with numerical simulations have been carried out to investigate the behaviour of aircraft vortex wake systems. This interest is associated primarily with air traffic and airport efficiency because of the potentially dangerous wake vortex encounter for aircraft during landing or take-off. As a consequence the FAA (*Federal Aviation Administration of the USA*) and ICAO (*International Civil Aviation Organization*) have established four different aircraft categories depending on the weight, and established safe separation distances and time intervals between following aircraft (ICAO [26]). More recently airport local air quality issues have become of interest and studies have been carried out in relation to the modelling of an aircraft wake vortex interacting with the jet engine exhaust plume. The complex vortical wake generated by aircraft is considered to be an important factor when considering the dispersion of pollutants in proximity to airports.

Few of the previous studies took account of the interaction between the vortex wake in ground proximity and a complete representation of the atmospheric boundary layer. The vertical velocity profile and turbulence characteristics of the atmospheric boundary layer are thought likely to influence both the decay and trajectory of the vortex wake. These factors were considered by Bernon [6] and shown to be potentially significant.

The aim of the current research is to extend the initial simulation study to include near ground effect, i.e. heights associated with the final stages of the approach to land and first stage climb. It is intended to establish the feasibility and validity of modelling experimentally a trailing vortex wake at the scales normally used in an atmospheric boundary layer wind tunnel. In this initial simplified model the interaction between the trailing vortices and the jet exhaust plume is neglected as are the vortices associated with the aircraft high lift systems. The study is split in two parts. The first one will show the results concerning the mean flow obtained using a five-hole probe. The data are then compared to theoretical/empirical models for wake vortex decay, and a model for the trajectory of the vortex wake in ground effect is presented. The second

part shows the properties of the fluctuating/instantaneous flow field due to turbulence, using data collected by means of a SPIV system.

1 Literature Review

In this first chapter key concepts and definitions will be given and discussed. This will include the theoretical base of the experimental data processing, interpretation and discussion which will be presented in the next sections. Definition and characteristics of aircraft wake vortices will be given as well as a description of the ambient wind profile and atmospheric turbulence in which airplane wakes naturally generate. A description of the Cranfield Atmospheric Boundary Layer Wind Tunnel (ABLWT) used to carry out the measurements will also be included in a dedicated section. In addition, ATTAS aircraft characteristics flow over delta wings as well as measurement techniques used within this project will be discussed.

1.1 Wake vortex system

Before proceeding with the description of wake vortices generation and characteristics, it is necessary to define the reference coordinate systems that will be used to refer the flow variables in this work. Three different coordinate systems are used in the present study, all of them are orthogonal Cartesian and normal: (i) wing reference system, (ii) ground reference system and (iii) vortex reference system, see Figure 1.

- The wing reference system (x, y, z), one of the most common in literature, is a normal orthogonal Cartesian system with origin located at the centre line of the wing trailing edge, x axis points downstream along the centre-line, y axis is along the wing-span and z axis points upward and is orthogonal to the wing plan at zero incidence.
- The vortex reference system (x_v, y_v, z_v,) origin is the mid-point of the initial vortex spacing. The axis directions are obtained by a 180° rotation of the y-z plane of the wing reference system about x. Thus z points downward and y points the opposite side with respect the wing reference system.

- The ground reference system (x_G, y_G, z_G) origin is obtained translating the vortex reference system origin to the ground along z, the x axis points downstream along the main flow direction, y axis points in the wing span-wise

direction and z is orthogonal to the plane defined by x and y (the ground) pointing upward.

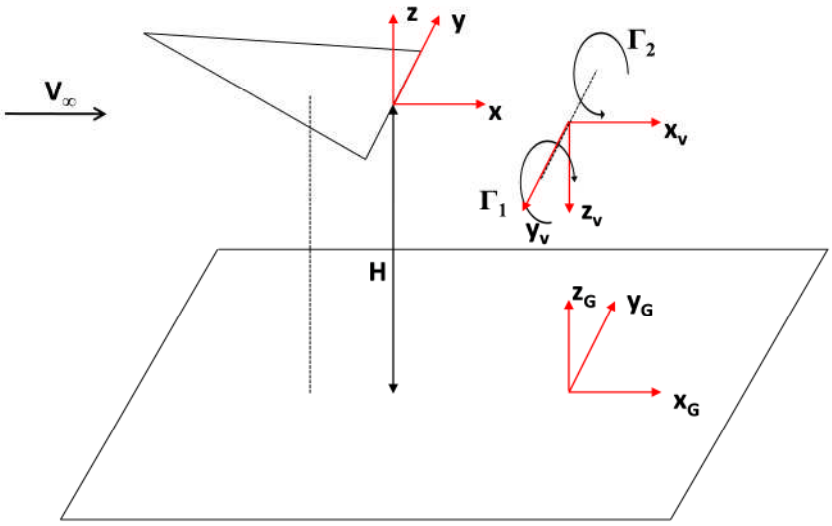

Figure 1 Schematic of the main reference systems used in this work

1.1.1 Vortex characteristics and parameters

A vortex is a complex three-dimensional flow characterised by a distribution of vorticity (ω), which is the curl of the velocity and is defined by:

$$\boldsymbol{\omega} = \boldsymbol{\nabla} \times \mathbf{V} \tag{1.1}$$

The strength of a vortex is identified as its circulation which is defined (Anderson [1]), by:

$$\Gamma = \oint \boldsymbol{V} \cdot \boldsymbol{dl} \tag{1.2}$$

The above integral is calculated over a closed line *c* which is usually placed at a cross-section of the stream tube. Since the stream-wise component of the vorticity and circulation is of primary interest in the study of wake vortices (Rossow [41]), applying the Stokes theorem to the previous formulation, the expression for the circulation which we will refer up to the end is obtained:

$$\Gamma = \oiint \omega_x dS = \oiint \left(\frac{\partial w}{\partial y} - \frac{\partial v}{\partial z}\right) dydz \tag{1.3}$$

where the integral is calculated over an area A enclosed by the line c.

The vortex flow structure is made up of two regions: (i) the *core* and (ii) the outer part of the vortex. The core is the region in which most of the vorticity is concentrated, where velocity and vorticity gradient are intense and characterised by a relatively low average velocity. On the contrary in the external region, much larger than the first one, low vorticity and lower gradients are found. Vortex *core radius* is defined by the location of maximum tangential velocity (V_θ), (Schell et al. [43], Gerz et al. [21]). According to Meunier et al. [32], it also can be defined using the angular momentum (J) by the following relation:

$$a^2 = \frac{1}{\Gamma} \oiint [(y - y_c)^2 + (z - z_c)^2] \omega_x dS \tag{1.4}$$

In the above formulation y_c and z_c are the coordinates of the vortex centre. Those can be determined whether by searching the peaks of maximum vorticity magnitude or computing the centroids of vorticity (Gerz et al. [21]), as follow:

$$y_c = \frac{1}{\Gamma} \int_{-\infty}^{\infty} \int_{0}^{\infty} y\omega_x dydz \qquad z_c = \frac{1}{\Gamma} \int_{-\infty}^{\infty} \int_{0}^{\infty} z\omega_x \, dydz \tag{1.5}$$

Vortices, due to viscous effect, dissipate and increase in core at the same time according to the following low (Meunier et al. [32]):

$$a^2 = 4\nu t \tag{1.6}$$

Finally when considering a vortex, one parameter of absolute importance is the vortex Reynolds number which, as explained in the next sections, greatly affects the vortex time and space evolution. It is defined by:

$$Re = \frac{\Gamma}{\nu} \tag{1.7}$$

1.1.2 Vortex formation

Wake vortices may be considered as a ‘dissipative structure’ that is, an energetic and self-organized pattern which develops temporarily while the flow returns to equilibrium, (Jacquin [27]). Wake vortices formation is a result of the lift generation by

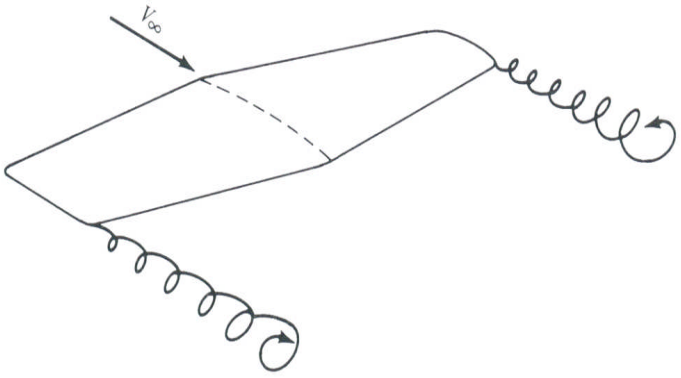

Figure 2 Schematic of the trailing vortices, taken from Anderson [1]

a finite wing. Generation of wake vortices starts at the wing tips (Figure 2) where the flow is driven by a favourable pressure gradient, due to the pressure difference between the lower and upper surface of the wing. The resulting high velocity gradients at the tips generate areas with a high concentration of vorticity. Furthermore, they result in energy transfer from the longitudinal plane (x-z) to the transversal plane (y-z). Although peaks of vorticity are found in the tip regions, vortex formation also involves the span of the wing. This results in a thin vorticity layer that is generated at the trailing edge. Because of the flow structure instability, this trailing edge layer rolls up determining a number of well-shaped vortices downstream the wing. The number of vortices depends on the wing geometry and configuration (slats, flaps and ailerons). Those regions in which the wing surface is discontinuous can generate vortices. The formation of trailing vortices is well explained by the Prandtl’s theory. Although it is an inviscid theory, it is one of the best known theoretical methods for predicting the flow characteristics over a finite wing placed at incidence. According to theory a lifting wing can be replaced by a lifting line which is obtained as a superimposition of an infinite number of horseshoe vortices of infinitesimal circulation ($d\Gamma$). Every horseshoe vortex is made up of a bound vortex and a pair of trailing vortices which depart at the lifting line tips in agreement with Helmotz’s theorem which dictates that a vortex filament must extend to infinity or form

a closed loop. A superimposition of an infinite number of horseshoe vortices determines a vortex sheet departing from the trailing edge of the wing which due to its instability rolls up, see Figure 3.

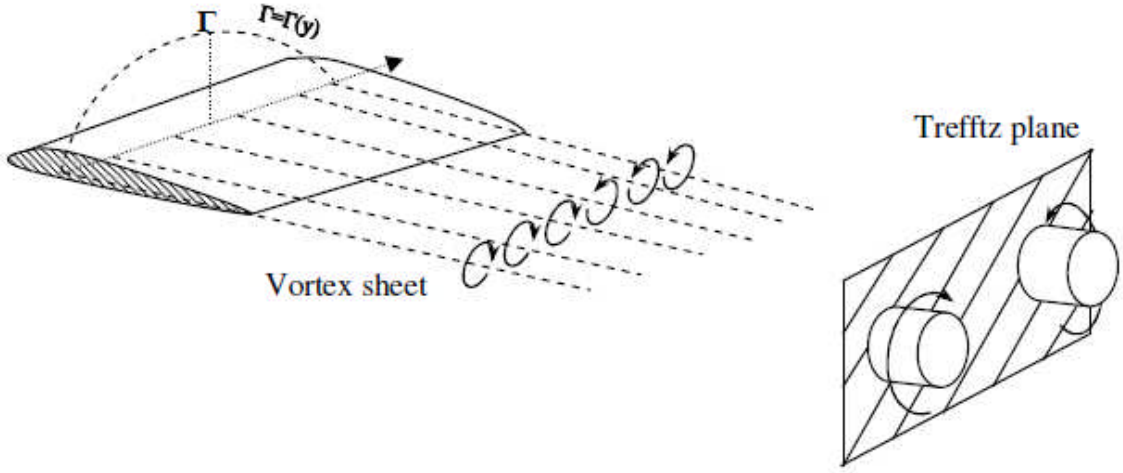

Figure 3 Sketch of the Prandtl's theory for finite wings, taken from Khalifa [28]

Summing the infinitesimal vortex filament circulation in the vortex sheet over half wing, the wake vortex circulation is obtained. Finally, this circulation equals the wing root circulation (Γ_{root}). The Kutta-Joukowski theorem asserts that the lift per unit span is equal to:

$$L' = V_\infty \rho_\infty \Gamma \tag{1.8}$$

Where Γ is the circulation calculated over a closed line around the airfoil. Integrating this formulation along the wing span, and assuming that the circulation is a function of the position along the wing span, the total lift generated by the wing is obtained.

$$L = V_\infty \rho_\infty \int_{-\frac{B}{2}}^{\frac{B}{2}} \Gamma(y)\, dy \tag{1.9}$$

In conclusion the vortex strength (circulation) is proportional to the lift generated by the aircraft or to its weight for fly level condition (not accelerating vertically).

1.1.3 Vortex configuration in the near field of an airplane

The thin vortex sheet at the trailing edge of a lifting surface rapidly rolls up to reach a stable state at a certain distance from the trailing edge. Roll-up phenomenon leads to the formation of a certain number of discrete vortex structures. The number and characteristics of wake vortices in the near field of an airplane depends on the wing geometry and the horizontal tail. It is possible to deal with wakes that account for one pair of counter-rotating vortices just downstream the wing, for example as is the case of a flaps-up configuration. A possible lift distribution over the wing that leads to this configuration is shown in Figure 4a. Figure 4b shows a typical lift distribution obtained with all the flaps down. This wing configuration may lead to the formation of two vortex pairs, co-rotating on each side of the airplane or multiple vortex pairs co-rotating and counter-rotating per each side of the airplane, Crouch [10]. Every sudden jump in the lift distribution graph corresponds to the formation of one vortex.

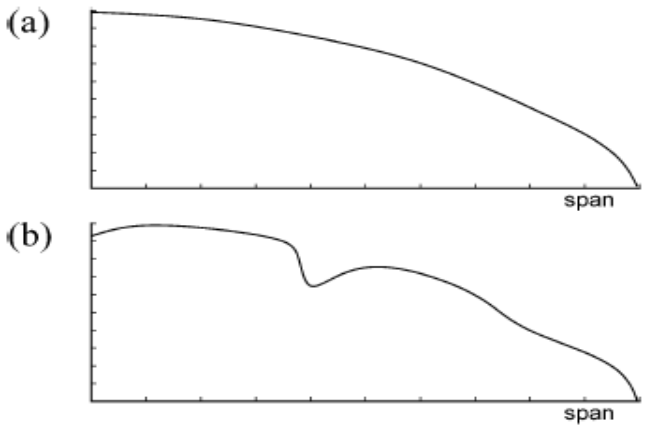

Figure 4 Span-loads for different wing configurations: (a) flaps up, (b) flaps down. (taken from Crouch [10])

1.1.4 Vortex space evolution: decay, merging and breakdown

Trailing edge vortex generation is a continuous phenomenon in time. Vortex flow is highly three-dimensional and is characterised by spiral streamlines. It may be sketched as a conical structure flow. A given vortex will dissipate because it is subject to viscosity, that at the same time makes it both, increase in core radius, involving a higher mass of fluid and decrease in circulation. This phenomenon also occurs with multiple vortices, such as when flaps are down. In this case, if two pairs of co-rotating

vortices form downstream of the wing, the vortices of each pair start rotating around each other, interacting as the ratio of the core radius to the vortex separation (a/d) increases (Meunier et al. [32]). As the above ratio reaches a critical value which varies into the range *0.25-0.3*, the vortex wrap around a core area. Following this, the vortex cores merge generating one single vortex, as shown in Figure 5.

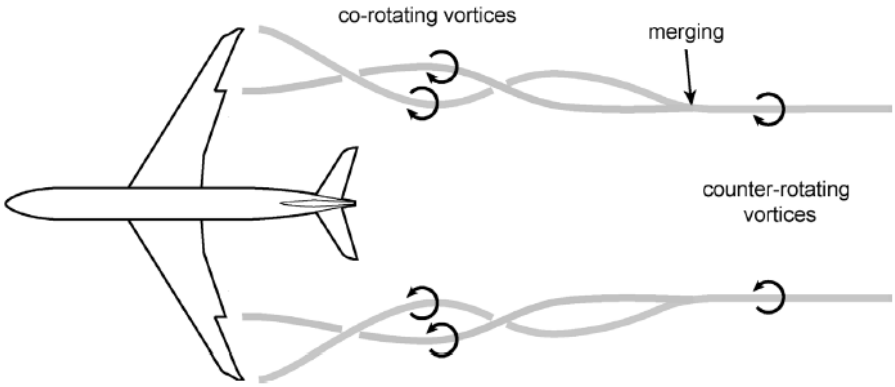

Figure 5 Wake vortex evolution behind an aircraft, taken from Meunier et al. [32]

The vortex merging time, according to Meunier et al. [32], Orlandi [34] and Fonti [20] strongly depends on the initial vortex separation as well as the vortex Reynolds number. After merging together, across the wing span, a single pair of counter-rotating vortices remains in the wake. These vortices move downward as a solid body inducing downward velocity. During their descent phase they keep dissipating energy and increasing in core diameter. At this stage these may undergo flow instabilities which eventually lead to the final breakdown of the vortices with the formation of multiple vortex rings.

Two well studied and known instabilities are considered in the present work: (i) Vortex Burst and (ii) Crow instability. Vortex burst is a sudden expansion of the vortex core. It may be happen to just one or both vortices.

Crow instability causes the vortex cores to draw together in a wavy pattern until they connect at the nearer points to form a series of vortex rings (see Crow [11]). The study carried out by Crow led to some theoretical predictions: 1) the trailing vortices distort into symmetric waves of length *8.6b*, for elliptical lift distribution, the instability grows by a factor e in a time equal to $1.21(2\pi b^2/\Gamma_0)$ and the perturbed vortices are confined to fixed planes which are inclined to the horizontal of *48°*, Crow [11]. Figure 6 shows a picture of the Crow instability.

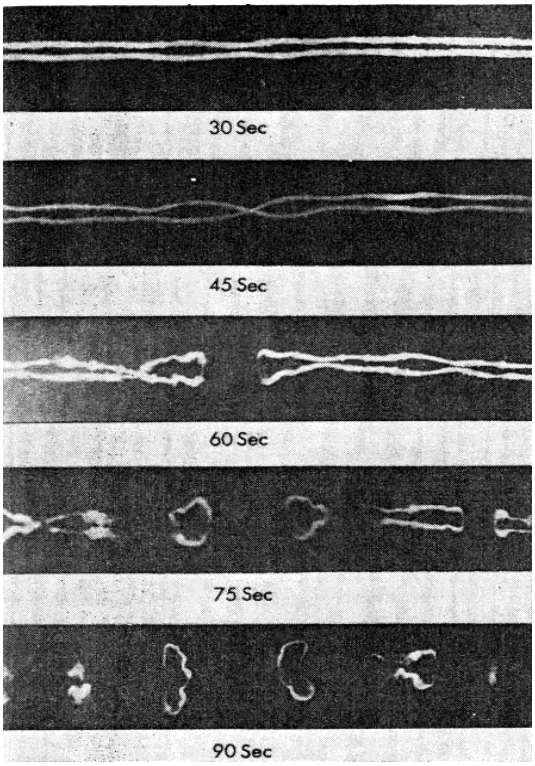

Figure 6 Crow instability, taken from Crow [11]

1.1.5 Wake vortex models

The most common formulations for radial profiles of the tangential velocity (V_θ) used to model a vortical wake of an aircraft are listed here. These vortex models are particularly useful to fit the experimental data collected.

- *Rankine model*

$$V_\theta(r) = \frac{\Gamma}{2\pi a}\frac{r}{a} \qquad for\ r \le a \tag{1.10-a}$$

$$V_\theta(r) = \frac{\Gamma}{2\pi r} \qquad for\ r > a \tag{1.10-b}$$

- *Lamb-Oseen model*

$$V_\theta = \frac{\Gamma}{2\pi r}\left(1 - e^{-\left(\frac{r}{a}\right)^2}\right) \tag{1.11}$$

- *Burnham-Hallock model*

$$V_\theta = \frac{\Gamma}{2\pi r}\frac{r^2}{r^2 + a^2} \tag{1.12}$$

- *Vatistas model*

$$V_\theta = \frac{\Gamma}{2\pi a}\frac{\frac{r}{a}}{\left(1 + \left(\frac{r}{a}\right)^{2n}\right)^{\frac{1}{n}}} \tag{1.13}$$

In Figure 7 the radial profile of the tangential velocity is reported for the four models here presented.

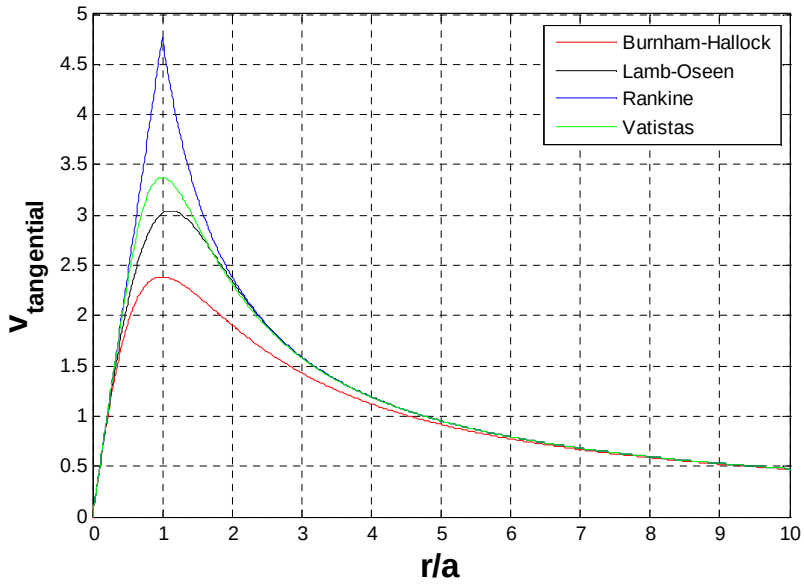

Figure 7 Vortex models: (red) Burnham-Hallock, (black) Lamb-Oseen, (blue) Rankine and (green) Vatistas

1.2 Atmospheric Turbulence

Atmospheric motions lead to the formation of a turbulent boundary layer attached to the earth's surface that is called planetary boundary layer (PBL). The mean speed profile and the turbulent profile along its height are functions of the earth morphology (mountains, hills, seas, oceans and so on). In the real case wake vortices generate and interact in the Atmosphere and in ground proximity (landing and take-off) they are flooded in the PBL, thus a realistic simulation should account for the effects of the atmospheric motions. Detailed knowledge and characterisation of the atmospheric

boundary layer (ABL) is required to assess the eventual effects on the wake vortices, but before some definitions regarding turbulent flows must be given.

1.2.1 Turbulence: definitions and general information

In analysing turbulence it is found that two flows starting with initial conditions that are slightly different will eventually become very dissimilar. A turbulent flow is characterised by random fluctuations so is not possible to predict its detailed evolution however some of its statistical properties can be predicted. Thus it is useful to consider averages and probability distributions of flow quantities. Due to the stochastic nature of turbulent flows under the hypothesis of steady flow, the flow variables are considered to be made up of two components: (i) a steady component and (ii) a superimposed fluctuating component. The steady component is the temporal average over some period of time T_e of the instantaneous quantities, which is defined by (Mathieu & Scott [31]):

$$\overline{u_i} = \frac{1}{T_e}\int_0^{T_e} u_i(t)dt \tag{1.14}$$

where u_i is a generic velocity component. The fluctuation of velocity is defined by:

$$u'_i = u_i - \overline{u_i} \tag{1.15}$$

and is usually interpreted as representing the turbulence, whose intensity in different directions is measured by the non-dimensional standard deviations:

$$I_{u_i} = \frac{\sigma_{u_i}}{|\bar{\boldsymbol{V}}|} = \frac{\left(\overline{u'^2_i}\right)^{1/2}}{|\bar{\boldsymbol{V}}|} \tag{1.16}$$

Another way to evaluate the overall turbulence intensity is by means of the turbulent kinetic energy (TKE) per unit mass which is defined by:

$$k = \frac{1}{2}\sum_{i=1}^{3}\overline{u'^2_i} = \frac{1}{2}(\sigma_u^2 + \sigma_v^2 + \sigma_w^2) \tag{1.17}$$

Furthermore turbulence contains a wide range of different scales. Different scales of motion coexist and are superimposed in the flow, with smaller ones living inside larger ones. A measure of the large scales of turbulence is given by means of the characteristic

length scale, or correlation length (L_T). This quantity provides a measure of the distance over which the velocity fluctuations differ significantly. Although the measurements of fluctuations from two spatially separated points, within the same flow, seem unrelated, a proper statistical analysis reveals that they are correlated. The degree of statistical correlation is measured using the velocity spatial correlations calculated by:

$$R_{ij}(\boldsymbol{x}, \boldsymbol{x}', t) = \overline{u'_i(\boldsymbol{x}, t) u'_j(\boldsymbol{x}', t)} \tag{1.18}$$

R_{ij} forms a 3x3 matrix of correlations between different velocity components, that is a tensor. As the distance of the two points considered increases, velocity correlations approach to zero, indicating that velocities de-correlate more and more the more they are separated (Mathieu & Scott [31]). Assuming a homogeneous turbulent flow characterized by having velocity fluctuations whose statistical properties do not depend on position, R_{ij} should not change if both x and x' are shifted by the same vector which implies that R_{ij} is a function of the only vector $r = x\text{-}x'$:

$$\overline{u'_i(\boldsymbol{x}, t) u'_j(\boldsymbol{x}', t)} = R_{ij}(\boldsymbol{r}, t) \tag{1.19}$$

Where the de-correlation condition is defined by:

$$R_{ij}(\boldsymbol{r}, t) \to 0 \quad as \quad |\boldsymbol{r}| \to \infty \tag{1.20}$$

Typical trend of an element of the two point velocity correlation tensor is shown in Figure 8. It has to be borne in mind that similar trends are for the other components that together form a three-dimensional field.

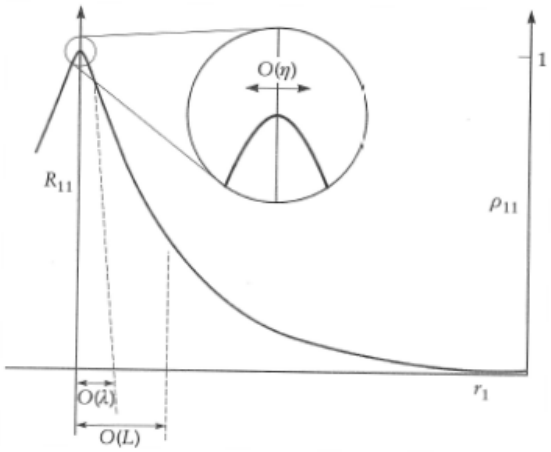

Figure 8 Sketch of the spatial velocity correlations as a function of the radial distance (r), taken from Mathieu [31]

Non-dimensionalising the velocity correlations by means of the standard deviations of the velocity components, and integrating this new variable along one of the three possible directions, a quantity with the dimensions of length is obtained.

$$L_{Tij}^{[k]} = \int_{-\infty}^{\infty} \rho_{ij}(r,t)dr_k = \int_{-\infty}^{\infty} \frac{R_{ij}(r,t)}{\sigma_i \sigma_j} dr_k \tag{1.21}$$

All the quantities $L_{ij}^{[k]}$ are supposed to be of the same order of magnitude and provide a quantitative measure of the correlation length scale or integral scale, which characterises the largest scales of turbulence (Mathieu & Scott [31]). In addition to spatial velocity correlations it is useful to define temporal velocity correlations, at a single point and two different times:

$$R_{ij}^{(t)}(\boldsymbol{x}, t, t') = \overline{u'_i(\boldsymbol{x}, t) u'_j(\boldsymbol{x}, t')} \tag{1.22}$$

Following the same non-dimensionalisation procedure as for the spatial correlation and under the hypothesis of steady flow, which implies that the correlations become function of the time delay $\tau = t - t'$, the correlation time is defined by:

$$T_{\tau ij} = \int_{0}^{\infty} \rho_{ij}^{(t)}(\boldsymbol{x}, \tau) d\tau \tag{1.23}$$

and represents the order of magnitude of the time needed for temporal de-correlation.

Turbulent flows are highly rotational and vorticity has intense small-scale random variation in space and time. The magnitude of these vorticity fluctuations is much larger than the mean vorticity and they are randomly orientated. Velocity derivatives are dominated by the smallest scales of turbulence. This scale is known as the Kolmogorov length scale and viscosity, which has little influence on the larger scales, become decisive at this scale, where dissipation of mechanical energy to heat occurs. Indeed when a turbulent flow is established, flow instabilities are responsible for keeping generation of turbulence, producing large-scale eddies which being unstable, give rise to smaller ones inside them and so on until the smallest scales are reached (Kolmogorov scale) where energy is dissipated via the viscosity effect. This process of transferring energy from the larger scales to smaller and smaller ones is known as the

Richardson cascade of energy. Since turbulence is a highly dissipative phenomenon it must be continuously supplied with energy to keep high the turbulent Reynolds number Re_L which is defined by:

$$Re_L = \frac{\sigma L_T}{\upsilon} \tag{1.24}$$

where L_T is the correlation length scale and σ is the intensity of one of the turbulent components. Turbulence is guaranteed if the above quantity is high enough. If the turbulent Reynolds number drops too low the energy cascade cannot longer operate and only the larger scales remain in the flow which, when affected by viscous action, decay progressively. Turbulence cannot longer exist without a source of energy that keeps active the energy cascade.

Finally turbulence is intrinsically three-dimensional. In two-dimensional flows that start with random initial conditions, the flow tends to coalesce to form larger structures. In this case, the energy cascade will not take place and the flow behaves in an opposite sense to three-dimensional turbulent flows in which large scales produce smaller ones (Mathieu & Scott [31]).

1.2.2 Atmospheric Boundary Layer

Atmospheric motions are slowed down in the lowest 1-2 km layer of the Atmosphere, due to the shear stress caused by viscosity, which is maximum at the ground where the wind velocity approaches to zero, creating a velocity profile function of the height. This layer is called planetary boundary layer (PBL) and is typically turbulent. Its height generally depends on wind strength and surface topography. The lowest part of the PBL, approximately the first 10% of its height is called the surface layer (SL) and is most relevant to this thesis, because aircraft land and take-off in this region.

1.2.2.1 Mean wind speed profile in the Surface Layer

In the surface layer all the vertical fluxes of momentum, heat and moisture are negligible, assumption that makes the equations of motion and the correspondent solution simpler. Its height depends on wind strength, Coriolis force and shear stress at

the ground, which is maximum and is equal to the drag force per unit surface area as defined by, (ESDU [16]):

$$\tau_0 = \rho u_*^2 \tag{1.25}$$

where u_* is the skin friction velocity, which is proportional to the wind speed, is a function of the surface characteristics and is defined by:

$$u_* = \frac{V_{10}}{2.5\, ln\left(\frac{10}{z_0}\right)} \tag{1.26}$$

In this formulation z_0 is the surface roughness parameter and takes account of the ground morphology. It is a measure of surface roughness and represents eddy size at the surface. It is dependent on height, shape and distribution of the surface features (Panofsky & Dutton [36]). Table 1 gives a list of the roughness length over uniform terrains.

Ground Cover	**Roughness parameter (m)**
City centres Forests	0.7
Small town Wooded country	0.3
Villages Countryside	0.1
Farmland	0.03
Fairly level grass plains	0.01
Runway area of airports Flat area with short grass	0.003
Flat desert Snow covered farmland Rough sea in storms	0.001

Table 1 Roughness parameter for different terrains

The Coriolis force per volume unit is defined by:

$$F_c = 2\rho V \Omega \sin\phi = \rho V f_c \tag{1.27}$$

Where $\Omega=72.9\cdot10^{-6}$ [rad/s] is the angular velocity of the Earth and ϕ is the local latitude.

According to ESDU [16] a particular solution of the full equations of motion returns the following relations in terms of velocity profile, thickness of the Atmospheric Boundary Layer (h) and mean wind speed at the gradient height (h):

$$\frac{V_z}{u_*} = 2.5\left[ln\left(\frac{z_G}{z_0}\right) + a_1\frac{z_G}{h} + \left(1-\frac{a_1}{2}\right)\left(\frac{z_G}{h}\right)^2 - \frac{4}{3}\left(\frac{z_G}{h}\right)^3 + \frac{1}{4}\left(\frac{z_G}{h}\right)^4\right] \tag{1.28}$$

$$\frac{V_h}{u_*} = 2.5\left[ln\left(\frac{u_*}{f_c z_0}\right) - A\right] \tag{1.29}$$

$$h = \frac{u_*}{B f_c} \tag{1.30}$$

The constants *A=-1* and *B=6* were established empirically by analyzing measured wind profile data, while a_1 is given by the following relation:

$$a_1 = 2(ln\,B - A) + \frac{1}{6} \approx 5.75 \tag{1.31}$$

Ignoring all the terms of order greater than one, the non-dimensional mean wind profile in the Atmospheric Boundary Layer is given by:

$$\frac{V_z}{u_*} = 2.5\left[ln\left(\frac{z_G}{z_0}\right) + 34.5\frac{f_c z_G}{u_*}\right] \tag{1.32}$$

This relation can be used up to z_G*=300 m*, so it well represents the wind profile within the Surface Layer. Also up to *30 m* above the ground the first order term in the last expression can be neglected making the wind profile exactly logarithmic.

The above description of the PBL and SL is valid as long as the boundary layer is in equilibrium which means that the wind has blown over a fetch of at least *100 km* over uniform terrain (ESDU [16]). If the boundary layer is in equilibrium its profile does not change as the fetch increases. If the wind blows over grounds with roughness changes, the boundary layer, being directly dependent on the roughness length, undergoes modifications in terms of shape and height. Downwind of a roughness

change, a new layer starts growing within the previous one. This new layer is not in equilibrium, thus it grows as x increases. When a fetch of at least *100 km* away from the place in which the wind experienced the terrain change is reached, the boundary layer is again in equilibrium and will keep its features as long as the reference wind speed and the terrain roughness are fixed, see Figure 9.

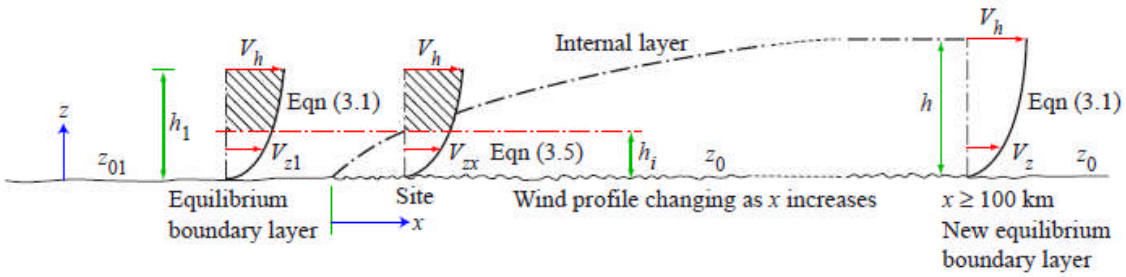

Figure 9 Developing wind profile, taken from ESDU [16]

1.2.2.2 Turbulence profile in the Surface Layer

According to ESDU [18], manipulating the definition of turbulence intensity in x direction, we can express I_u as follow:

$$I_u = \frac{\sigma_u}{u_*}\frac{u_*}{V_z} \tag{1.33-a}$$

where

$$\frac{\sigma_u}{u_*} = \frac{7.5\eta\left[0.538 + 0.09\,ln\left(\frac{z}{z_0}\right)\right]^p}{1 + 0.156\,ln\left(\frac{u_*}{f_c z_0}\right)} \tag{1.33-b}$$

$$\eta = 1 - \frac{6f_c z}{u_*} \quad and \quad p = \eta^{16} \tag{1.33-c}$$

V_z/u_* is given in the previous paragraph. These expressions are valid if the terrain is uniform upwind of the site in analysis for at least *30 km*. It is interesting to notice that near the ground the ratios σ_v/σ_u and σ_w/σ_u are generally constant irrespective of the nature of the terrain, and their value is given by:

$$\frac{\sigma_v}{\sigma_u} = 1 - 0.22cos^4\left(\frac{\pi}{2}\frac{z}{h}\right) \quad (1.34\text{-a})$$

$$\frac{\sigma_w}{\sigma_u} = 1 - 0.45cos^4\left(\frac{\pi}{2}\frac{z}{h}\right) \quad (1.34\text{-b})$$

This means that turbulence intensity in y and z directions are functions of the turbulence intensity along x and can be obtained by evaluating I_u.

1.2.3 Vortex decay in the Atmosphere

Aircraft move within the Planetary Boundary Layer, and as a result, the wake vortex systems they generate, naturally develop in a stratified ambient, with vertical flux of momentum and energy, where shear stress and turbulence intensity are increasingly strong as the ground is approached. Turbulence is a highly dissipative phenomenon so every flow structure dissipates energy much faster compared to the laminar case so do wake vortices. Turbulence accelerates the onset of Crow instability and vortex burst which destroy the coherence of vortex systems that eventually dismiss. The vortex lifespan is a function of the vortex strength, Reynolds number and turbulence intensity through a turbulence parameter defined by Crow & Bate [12]:

$$\varepsilon^* = \frac{(\varepsilon b_0)^{\frac{1}{3}}}{V_0} \quad (1.35)$$

where b_0 and V_0 are respectively the vortex spacing and initial descent speed defined by:

$$V_0 = \frac{\Gamma_0}{2\pi b_0} \quad (1.36)$$

and ε is the turbulence dissipation rate given by (Mathieu [31]):

$$\varepsilon = \frac{1}{2}\upsilon\overline{\left(\frac{\partial u'_\iota}{\partial x_J} + \frac{\partial u'_J}{\partial x_\iota}\right)\left(\frac{\partial u'_\iota}{\partial x_J} + \frac{\partial u'_J}{\partial x_\iota}\right)} \quad (1.37)$$

Greene [22] introduced a model for the prediction of vortex circulation decay and vortex descent that under the hypothesis of constant vortex separation, takes account of the viscous effects, atmospheric stratification effects and turbulent effects. Its model

considers the wake as a descending solid body that experiences equivalent viscous force as the real wake, see Figure 10, and states that the rate of change of impulse per unit length of wake is equal to the sum of the viscous drag force supposed acting on the solid body, the buoyancy force due to the Atmosphere stratification and a turbulent viscous force that is expressed in terms of vortex system descent as:

$$\frac{d^2Z_v}{dT^2} + \frac{C_D L_B}{4\pi b}\left(\frac{dZ_v}{dT}\right)^2 + 0.82Q^*\left(\frac{dZ_v}{dT}\right) + \frac{A_B(N^*)^2}{2\pi b^2}Z_v = 0 \qquad (1.38)$$

where the above formulation is in non-dimensional form and all the variables and parameters are non-dimensionalised using vortex spacing (considered constant) and initial descending velocity (V_0), see Table 2.

Variable	Symbol	Value
Descent	Z_v	z_v/b_0
Time	T	tV_0/b_0
Stratification parameter	N*	Nb_0/V_0
Turbulence parameter	Q*	q/V_0

Table 2 Variables and parameters non-dimensionalisation

C_D is the drag coefficient of the solid body which is considered to replace the wake in the model and is *0.2* for *Re > 600,000* and *1.4* for *Re < 400,000* but its validity must be evaluated experimentally. L_B and A_B are respectively the characteristic length of the solid body and its area, see Figure 10.

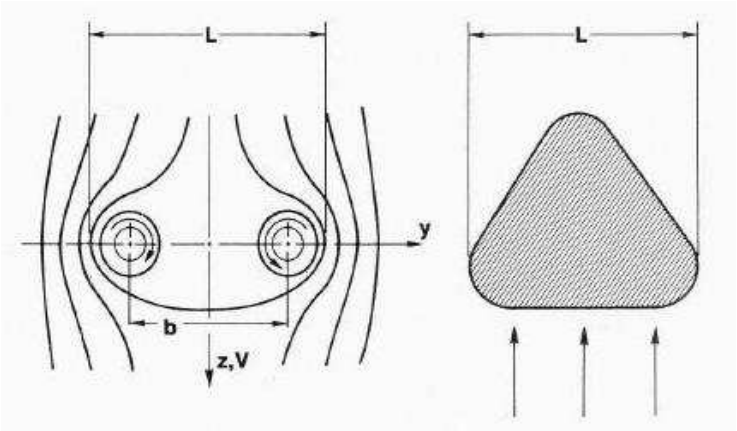

Figure 10 Sketch of the wake and the solid body which is considered to replace the wake, taken from Greene [22]

Sarpkaya [42], proposed a new model which states that the rate of change of impulse per unit length is equal to the sum of the buoyancy force due to the atmospheric stratification and the force due to the rate of change of circulation. The viscous drag coefficient in Greene's model is eliminated because it is not hydro-dynamically defensible. The relation for the descent is given by the following ordinary differential equation:

$$\frac{d^2 Z_v}{dT^2} + \omega^2 N^{*2} Z_v + \frac{C}{T^*} e^{-\frac{C}{T^*}T} = 0 \tag{1.39}$$

whereas the circulation decay is given by:

$$\frac{\Gamma}{\Gamma_0} = e^{-\frac{C}{T^*}T} \tag{1.40}$$

where C and ω are constants and T* is the time at which a "catastrophic demise event" occurs (Crow instability or core bursting). T* appears to be a function only of the turbulence parameter ε* and is expressed in various intervals by the following relations:

For T* < 2.25 or ε* > 0.2535

$$\varepsilon^* T^{*\frac{4}{3}} = 0.7454 \tag{1.41-a}$$

For 2.25 < T* < 7 or 0.0121 < ε* < 0.2535

$$\varepsilon^* = T^{*\frac{1}{4}} e^{-0.70T^*} \tag{1.41-b}$$

For 7 < T* < 9 or 0.001 < ε* < 0.0121

$$T^* = -180\varepsilon^* + 9.18 \tag{1.41-c}$$

And T* = 9 for all values of ε* < 0.001.

In Figure 11 the vortex lifespan versus turbulence parameter is shown. The predictions based on the Sarpkaya [42] and Crow & Bate [12] models are compared to some experimental and numerical data.

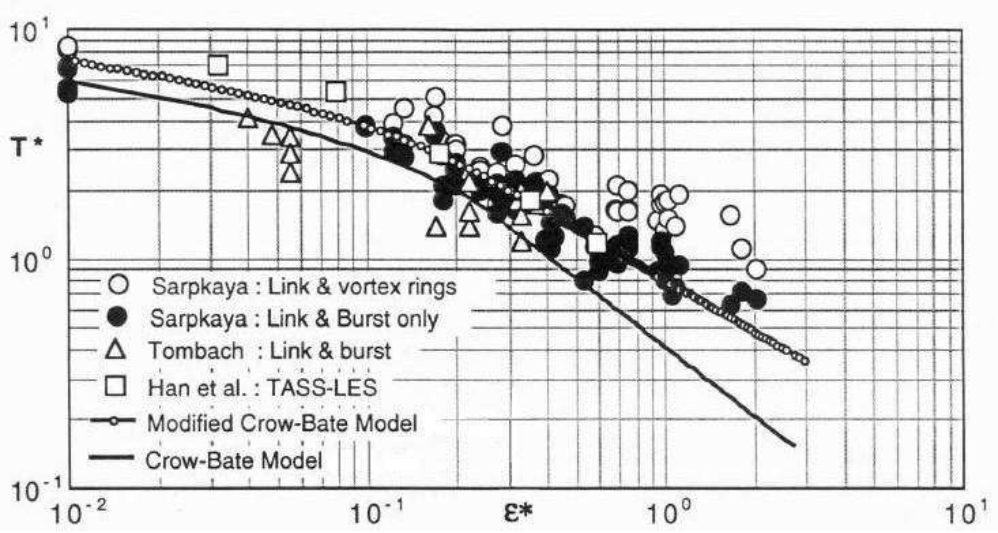

Figure 11 Vortex lifespan versus turbulence parameter, taken from Sarpkaya [42]

The model takes also in account the ground effect. Sarpkaya defined the ground effect region as the region between the ground and a height equal to *1.5 times* the initial vortex separation. When the vortices reach a height of $1.5b_0$ they continue to decay at a constant rate equal to that at $z_G=1.5b_0$. As a result the circulation decay and vortex descent in ground effect are given by:

$$\frac{d\Gamma}{dT} = -\frac{C}{T^*}\Gamma_0 e^{-\frac{C}{T^*}T_G} \tag{1.42-a}$$

$$\frac{d^2Z_v}{dT^2} + \omega^2 N^{*2} Z_v + \frac{C}{T^*} e^{-\frac{C}{T^*}T_G} = 0 \tag{1.42-b}$$

Where T_G is the non-dimensional time at which the vortices enter in the ground effect region.

By having knowledge of all the parameters involved in these two models for vortex decay in the Atmosphere, it is possible to integrate numerically the relevant differential equations to obtain point by point, the descent profile of a pair of aircraft wake vortices.

1.2.4 Vortex in ground effect: Vortex rebound

When a system of wake counter-rotating vortices is close enough to the ground, the vortices start diverging progressively while descending at the same time. Each vortex induces a cross-flow which has its velocity peak somewhere beneath the vortex.

This cross-flow at the interface with the ground determines a boundary layer which encounters an adverse pressure gradient outboard the peak of velocity. As the vortex system approaches the ground the pressure gradient increases and eventually the boundary layer separates creating a "bubble" of opposite vorticity (Figure 12). This secondary vortex quickly grows pushing up the primary vortex. This phenomenon called rebound for the first time was observed by Harvey & Perry [23]. Vortex rebound was also observed by Barker & Crow [4] in 1977 carrying out flow visualisations in water tank. In the latter case, they found vortex rebound occurring after the wake vortex spacing has reached four times the initial spacing. They also found the vortex trajectory in ground effect diverging from the prediction given by the vortex line theory given by Lamb [29]. This was confirmed by the study carried out by Atias & Weihs [3], who developed a new model for vortex rebound. They built an inviscid model using infinite vortex sheets to simulate the boundary layer at the ground and vortex images. In this way they could model the phenomenon by obtaining the secondary vortex rotating around the primary one but the results correspondent to the looping phase were not in agreement with the experimental studies. However the vortex rebound appears to be far more complex than what at the beginning was found. Indeed, according to Orlandi [35] that carried out 2D numerical simulations in 1990, the primary vortex after the first rebound from which a secondary vortex is created and after a loop might undertake several successive rebounds that lead to creation of tertiary vortices that slow down the lateral translation of the main vortex. Unfortunately these results were not compared to experimental results that show a quicker dissipation of the vortices before the multiple rebounds occur.

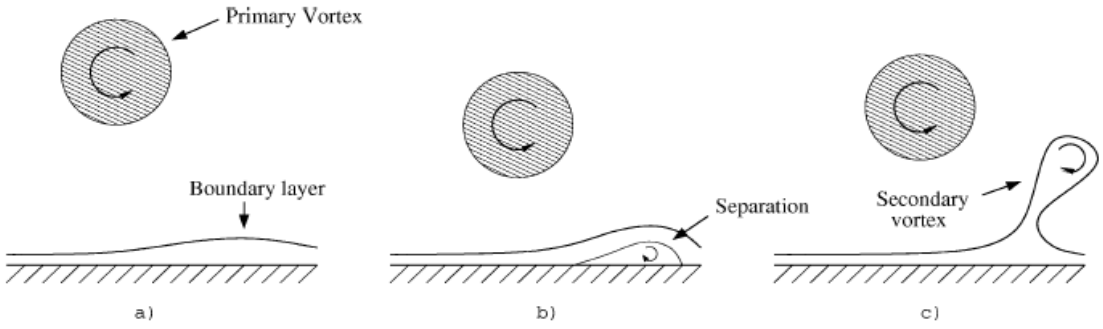

Figure 12 Sketch of vortex rebound, taken from Puel [39]

1.3 ABLWT

1.3.1 Simulating the ABL

The structure of the wind within a few hundred meters above the ground is highly complex and an adequate simulation of it would require knowledge of some key parameters: mean velocity profile, turbulence intensity along the three main directions, integral scales of turbulence, micro-scales of turbulence and velocity correlations. A wind tunnel simulation of the Atmospheric Boundary Layer requires equality of the turbulent Reynolds number which assures flow dynamic similarity. To achieve this condition it is necessary to scale by the same factor all the lengths involved, which means, once a desirable scale factor is chosen, the height, the characteristics lengths of turbulence and the roughness parameter must be scaled by the same factor. Making the ABL develop naturally generally implies prohibitively long wind tunnels (Armitt & Counihan [2]). As a consequence to reproduce the ABL at great scale factors it is necessary to accelerate its development. This is achieved using a number of roughness, barrier and mixing devices (Armitt & Counihan [2] and Cook [8]).

1.3.2 Cranfield ABLWT

The Atmospheric Boundary Layer Wind Tunnel (ABLWT) at Cranfield, Figure 13, has a *2.4m* wide and *1.2m* high test section downstream a *14.5m* long flow development section in which a combination of ground roughness elements, turbulence grids and elliptical vortex generators are to create the $1/200^{th}$ scale model of the atmospheric boundary layer which develops in typical open pastureland (roughness, $z_0=0.03$). Refer to Bernon [6], for a full description of the tunnel.

The longitudinal turbulence intensity profile and mean wind speed profile within the ABLWT are compared with those given by ESDU [16-19] in Figure 14.

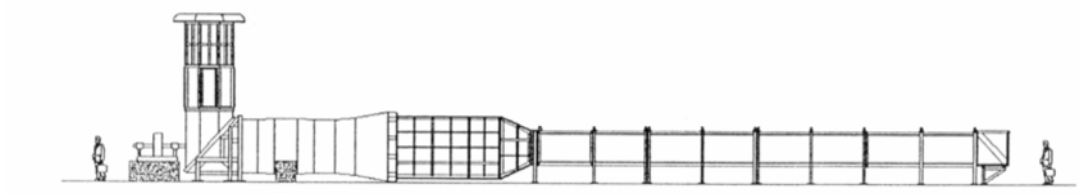

Figure 13 Representation of the Cranfield ABLWT, taken from Bernon [6]

The boundary layer results to be compressed along its height in the tunnel with a *1/200*th scale factor. The mean speed profile and turbulence profile are in good agreement with the ESDU model up to *120 m* of the full scale model. However, the turbulent dissipation rate, which depends on the velocity gradients within the flow in the region close to the ground (if it is assumed that the production and dissipation of turbulent kinetic energy are almost equal), is not simulated. As a result the scaled model obtained is *5-6 times* more dissipative than the real one. Thus this is a key point for analysing, interpreting and eventually comparing the experimental results and must not be neglected. Also it should be emphasised that the relative movement between the wing and the ground and boundary layer is not simulated in this quasi-static experiment. In the real case the wing moves at a certain speed within the ABL therefore the entire flow field in the wing reference system is a superimposition of the uniform flow dependent on the wing speed and the ABL profile. A moving-model simulation would be required for a more realistic representation of full scale.

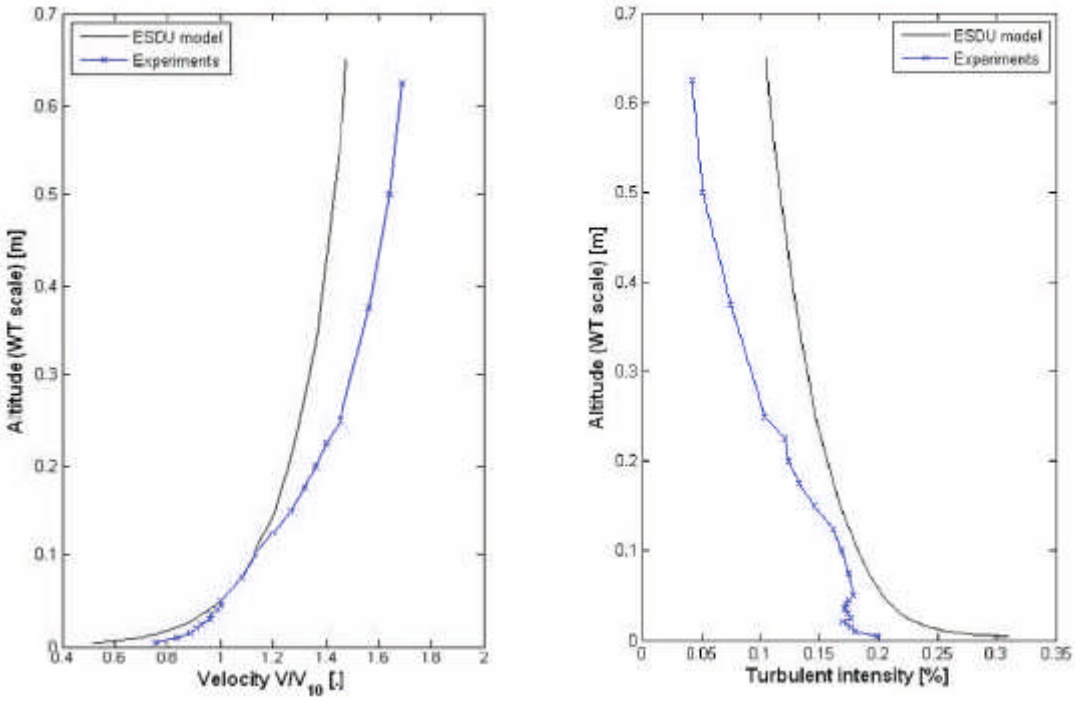

Figure 14 Mean velocity profile and turbulence profile within the ABLWT, taken from Bernon [6]

1.4 Experimental Test Case – ATTAS Aircraft

1.4.1 General Information

The VFW 614 ATTAS (Advanced Technologies Testing Aircraft System) owned by the DLR (German Aerospace Center) was designed to serve as an in-flight simulator for a wide range of different experiments. It is based on the 44-seater, twin-engine VFW 614 developed by Bremen-based VFW Fokker (DLR [14]). Figure 15 shows a picture of the ATTAS while in Table 3 a detailed description of the aircraft characteristics and performance is outlined.

Figure 15 ATTAS aircraft

1.4.2 ATTAS wake: previous wake measurements

In landing and take-off the aircraft uses high-lift systems including flaps and as consequence generates a wake, that in the region close to the wing trailing edge, is made up of a number of vortex pairs depending on its exact wing configuration. Moreover, the horizontal tail surface generates further vortices so in the vicinity of the aircraft the wake is complex and it is difficult to model. However, after a number of spans downstream, the wake can be modelled by a pair of counter-rotating vortices. Within the S-Wake research programme (2000-2003), in-flight measurements of the ATTAS wake were carried out both in cruise and in landing phase. During the S-Wake project evaluation of the ATTAS wake was taken using the Do128 as wake encounter. In Figure 16 some results from the S-Wake programme are reported: circulation, core radius,

vortex spacing and maximum tangential velocity trends versus non dimensional time, are found.

1.4.3 Reproducing the ATTAS wake within the wind tunnel

To reproduce the wake of an aircraft within a wind tunnel it is necessary to scale it in terms of geometry and strength. If dynamic similarity (same Reynolds number as the full scale flow) were assured a geometric scale model of the aircraft would be needed. In our case due to constraints imposed by the scale model of the Atmospheric Boundary Layer, and the quasi-static nature of the experiment (model fixed within the working section of the tunnel) a geometric scale model of the ATTAS aircraft would not return a realistic scale model of the wake. Because of this, a flat plate delta wing placed at incidence will be used to achieve this aim. The delta will be designed to obtain a geometric scale model of the wake. The scale factor used is *1/200* because a well established simulation of the Atmospheric Boundary Layer is available for the ABLWT in Cranfield University [1.3]. The key parameters to be scaled to obtain a *1/200*th geometric scale model of the ATTAS wake are: (i) initial vortex spacing (b_0), (ii) initial vortex circulation (Γ_0) and (iii) initial vortex core radius (a_0). The *1/200*th scale model of the wake is characterised by the following parameters:

$$b_{0s} = f\, b_{ATTAS} \tag{1.43-a}$$

$$a_{0s} = f\, a_{ATTAS} \tag{1.43-b}$$

$$\Gamma_{0s} = f\, \Gamma_{ATTAS} \tag{1.43-c}$$

where f is the scale factor which in the present case is equal to *1/200*. The values correspondent to the ATTAS wake, were extrapolated from Figure 16 at non-dimensional time 1.

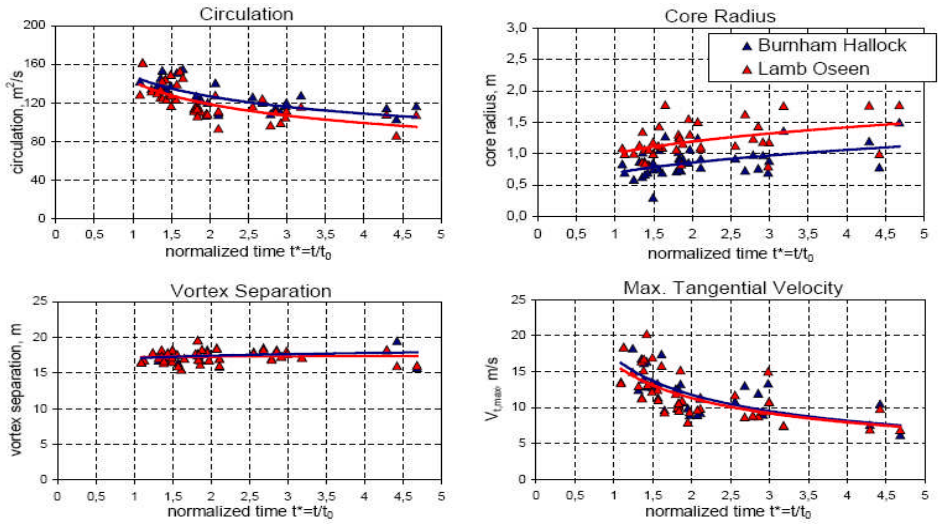

Figure 16 ATTAS wake vortex characteristics fitted to two different vortex models. (Lamb-Oseen, Burnham-Hallock). The measurements were taken by flight test using the Do128 as wake encounter within the S-WAKE project, taken from de Bruin [13]

Technical Data	ATTAS
Length	20.60 m (24.39 m with nose boom)
Height	7.84 m
Wingspan	21.50 m
Wing area	64 m^2
Cabin width	2.66 m
Cabin height	1.92 m
Seats	Three seats for crew members and up to seven seats for scientists.
Empty mass	14.9 t (with permanent test equipment)
Total mass	20.8 t max
Engines	Two Rolls-Royce M45 H engines
Thrust	2 x 32 kN (no reverse thrust)
Range	1800 km
Flight altitude	7600 m max
Speed	700 km/h
Fuel tank capacity	6224 l
Original use	Short-haul commercial aircraft
DLR flight facility	Brunswick

Table 3 ATTAS aircraft characteristics

1.5 Flow over delta wings

Simulating the ATTAS wake will be achieved using a correctly scaled delta wing. Therefore it is useful to revise the flow characteristics for this wing configuration.

1.5.1 General flow characteristics

According to Smith [44], the flow past a delta wing, placed at incidence, separates from the leading edges forming a pair of spiral vortices as a result of the vorticity in each shear layer. As the angle of attack is increased, the primary attachment lines on the upper and lower surfaces of the wing move to the axial centre-line (Figure 17). The boundary layer formed in the flow outboard from the upper surface attachment line separates along a line from which a further shear layer originates. This secondary separation leads to the formation of a secondary vortex, of opposite sign to that of the primary vortex, which lies close to the wing surface and nearer to the leading edge (Figure 18). According to Taylor et al. [46], the primary vortex is much bigger than the secondary vortex and contains the majority of the vorticity. This secondary separation must happen as a consequence of the non-slip condition at the surface of the wing (Honkan & Andreopoulos [25]).

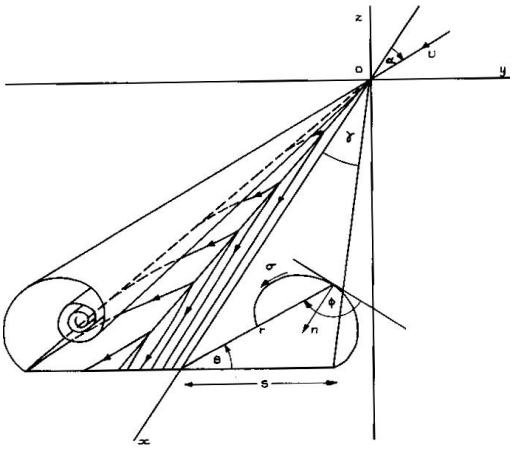

Figure 17 Sketch of the flow over a delta wing, taken from Smith [44]

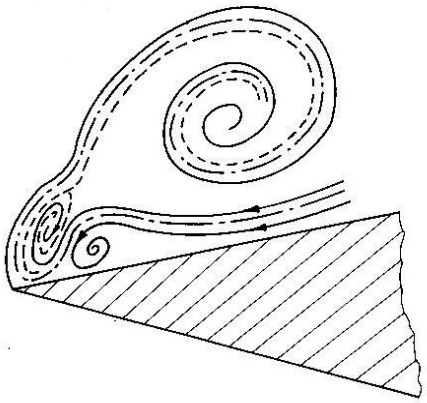

Figure 18 Schematic of the flow along a delta wing's leading edge

The general delta wing flow field described above is affected by: (i) Reynolds number, (ii) wing geometry and (iii) leading edge profile. To assess the effect of the

Reynolds number two cases are distinguished: flow over *low sweep angle delta wings* and flow over *slender delta wings (high sweep angle)*. In the first case the formation of the vortices is strongly Reynolds number dependent. As Reynolds number is reduced the trajectory of the primary vortex moves toward the centre-line (Taylor et al. [46]). For slender wings, according to Smith [44], the entire flow is steady and stable as long as free-stream speed and angle of attack are fixed. The main features are almost independent of Reynolds number in the large scale. It is important to recognise that in *both cases* the local flow may be affected by changes in Reynolds number, particularly in the boundary layer transition region. In terms of the strength of the vortices there is a proportionality relation (Hemsch & Luckring [24]), that connects vortex circulation (Γ) over a slender wing to the sweep angle (Λ) and the chord length (c):

$$\frac{\Gamma}{V_\infty} = \frac{c}{(\tan \Lambda)^{0.8}} \tag{1.44}$$

Relatively few studies have been conducted on the effect of leading edge profile on the flow over a delta wing. Miau et al. [33], present the results of a flow visualization study which suggests that a sharp leading edge bevel is favourable to the formation of well-organized vortex structures.

Finally, under certain conditions, the vortices might be affected by instabilities before reaching the trailing edge. One of the best known and most studied is vortex breakdown (also called vortex burst). Vortex breakdown is a sudden expansion of the core as a consequence of a sudden decrease in longitudinal speed of the flow on the upper side of the wing. Many studies have been carried out concerning this phenomenon. In Figure 19, vortex breakdown location versus incidence, for different leading edge sweep angle, is reported, (Thomson [47]).

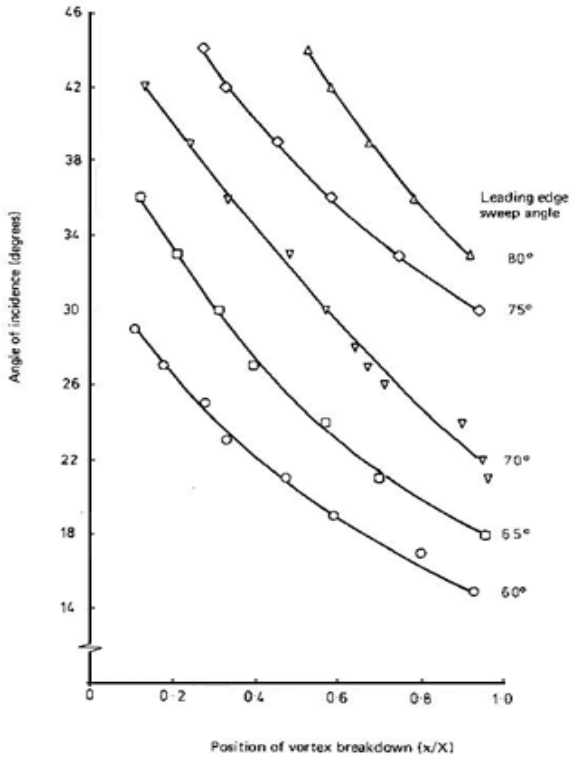

Figure 19 Vortex breakdown position for a series of slender delta wing models, taken from Thomson [47]

1.5.2 Smith's theory

Smith [44], proposed a theory for the prediction of the flow over slender delta wings ($\Lambda > 60°$). The theory is based on some important hypothesis on the wing model and the flow which it is subject. Those are subsequently reported.

- *Viscosity neglected*

  Viscosity was observed to be important only in the boundary layers on the wing surface and in a small vortex 'sub-core' which is found in the spiral vortex. Out of these regions the flow was found to be Reynolds number independent, thus an inviscid model well describes the large-scale features of the separated flow.
- *Representation of rotation*

  The vortex sheet is divided into an inner and an outer part. The inner part is represented by an isolated potential vortex joined by a cut to the "free" end of the outer part. The entire flow is considered irrotational except for the vortex sheet and a velocity potential exists but it jumps across the sheet.
- *Conical flow*

- *Slender body approximation*

  The stream-wise gradient of the stream-wise component of velocity is small compared with the gradients normal to the main flow direction.
- *Flat-plate wing*

A comprehensive description of the calculation involved in the development of the theory is found in Smith [44]. The theory gives a prediction of the vortex position over the wing and shape and strength of the vortex sheet, parameters in which we are interested to achieve the delta wing model design.

The predictions are in good agreement with experimental results: position and shape of the primary vortex are predicted successfully (see Figure 20-Figure 21).

The model appears to work well for:

- thin and slender wing (from hypothesis)
- for relatively high Reynolds number
- for $e \cong 1$ where e is the ratio $\frac{tan\alpha}{tan\delta}$ (at low values of e the primary separation is affected by the secondary one). The best results are obtained for $e = 0.91$.

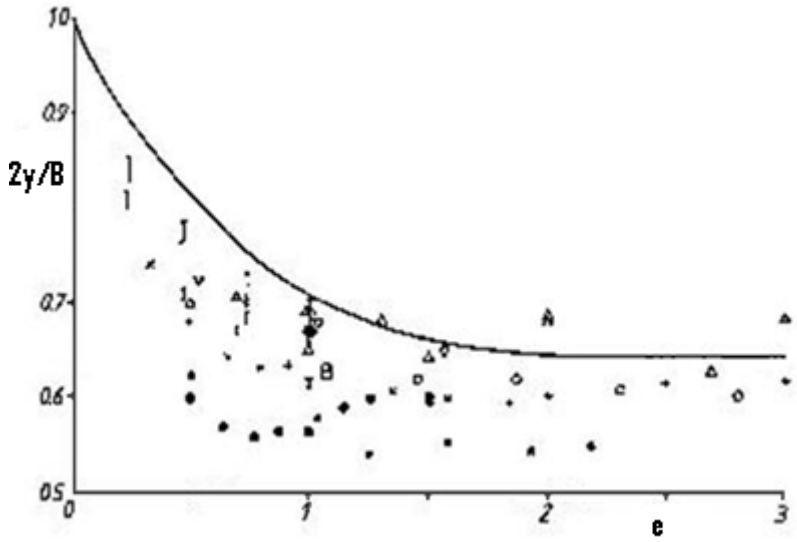

Figure 20 Vortex lateral position predicted by theory against the ratio between wing incidence and wing apex angle The theory is compared to experimental and computational data. Figure taken from Lowson [30]

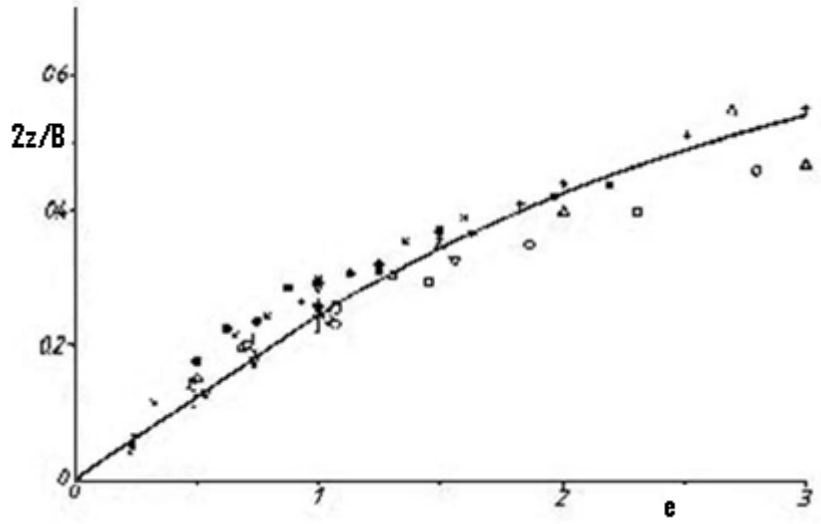

Figure 21 Non-dimensional vortex height above the wing. The theory prediction is compared to experimental and computational data. Taken from Lowson [30]

1.6 Measurement techniques

To measure the flow field behind the wing model within the wind tunnel working section two measurement techniques were used: (i) Five-hole probe and (ii) Particle Image Velocimetry. The five-hole probe was used initially to locate the vortices into the wake over several vertical planes. Also having knowledge of the vortex location provided *a-priori* information for the PIV set-up such as camera position and imaging area.

1.6.1 Five-hole probe

1.6.1.1 General overview

The five-hole probe technique is an intrusive measurement technique made up of five pressure sensing holes arranged in a cruciform configuration (Figure 22). The central hole takes evaluation of the local total pressure whereas the four holes around it provide measures of the static pressure. These measurements are time-average measurements over a time which depends on frequency and number of cycles (number of evaluations) that the system adopts. Thus a 5-hole probe system is not able to give detailed characterization of highly turbulent/fluctuating flows: it provides evaluation of

the time-average flow field. The pressures recorded by the probes are processed in velocity along the three main directions (x, y, z). Known relationships between the static pressures and the total pressure yield the three velocity components. These relationships must be expressed as functions of the flow angularity so that calibration of the system and consequently measurements in specific experiments are independent on the flow velocity and the Reynolds number.

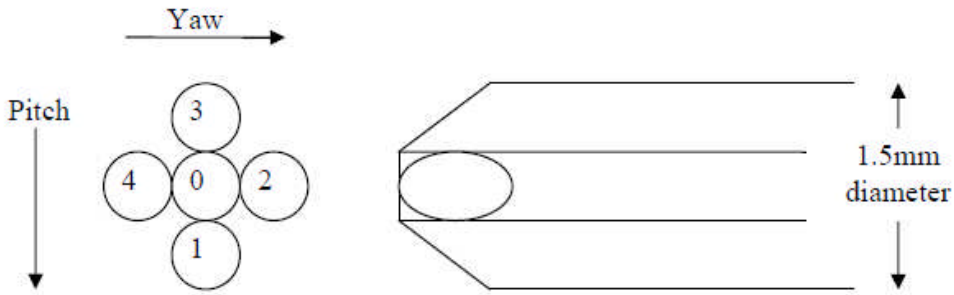

Figure 22 Sketch of a five-hole probe

1.6.1.2 Calibration

Although for some probe geometries (for example spherical geometry) a potential flow solution can predict the pressure distribution and corresponding calibration characteristics, due to manufacturing inaccuracies a calibration of the system is required. This is made by setting up the probe in a known flow field, for example a uniform flow field and see how it responds changing its orientation with respect the main flow direction (Treaster [50]). Two ways can be adopted to calibrate a 5-hole probe system: (i) *yaw-pitch mode* and (ii) *pitch-yaw mode*. In the first case the probe is fixed at one of the predetermined yaw angle within the flow and moved in prescribed increments trough the pitch angle range. In the pitch-yaw mode instead for each predetermined pitch angle the probe is moved along its yaw angle range. In both cases the pressure of each individual tube is calculated for each probe position (calibration point) and the non-dimensional coefficients functions of the flow angularity are derived according to the following relations:

- Pitch coefficient:

$$C_{p\theta} = \frac{p_1 - p_3}{p_0 - \bar{p}} \tag{1.45}$$

- Yaw coefficient:

$$C_{p\varphi} = \frac{p_2 - p_4}{p_0 - \bar{p}} \tag{1.46}$$

- Total pressure coefficient:

$$Cp_{total} = \frac{p_0 - p_{total}}{p_0 - \bar{p}} \tag{1.47}$$

- Static pressure coefficient:

$$Cp_{static} = \frac{\bar{p} - p_{static}}{p_0 - \bar{p}} \tag{1.48}$$

where

$$\bar{p} = \frac{p_1 + p_2 + p_3 + p_4}{4} \tag{1.49}$$

These coefficients together with pitch and yaw angles form a series of calibration maps (or 3D surfaces) which report yaw angle and pitch angle as functions of yaw coefficient and pitch coefficient and static pressure coefficient and total pressure coefficient as a function of yaw angle and pitch angle (see Figure 23).

1.6.1.3 Application: data processing

The calibration maps are used to evaluate the flow properties (velocity components along x, y, z, total and static pressure) in specific experiments according to the following steps:

- The five pressures are provided by the probe and pitch and yaw coefficients are evaluated according to the formulations.
- Pitch angle (θ) and yaw angle (φ) are evaluated from a calibration map of the type presented in Figure 23.
- From θ and φ static pressure coefficient and total pressure coefficient are evaluated by the calibration data.
- Total pressure and static pressure are evaluated using the respective coefficients.

- Velocity magnitude is evaluated by:

$$V = \sqrt{\frac{2}{\rho}(p_{total} - p_{static})} \tag{1.50}$$

- The three components of the velocity along x, y and z, namely u, v and w are calculated depending on the calibration mode; for *yaw-pitch mode*, which is adopted in this study, the velocity decomposition in the probe reference system (Figure 24) is given by:

$$u = V \cos\varphi \cos\theta \tag{1.51-a}$$

$$v = V \sin\varphi \tag{1.51-b}$$

$$w = V \cos\varphi \sin\theta \tag{1.51-c}$$

Even for the most accurate instrumentation, uncertainties exist so a measurement uncertainty is expected to affect the results provided by a 5-hole probe. For the system used this was assessed by Dockrill [15] and corresponds to *+/-0.2°* for angles and *2%* for velocity magnitude.

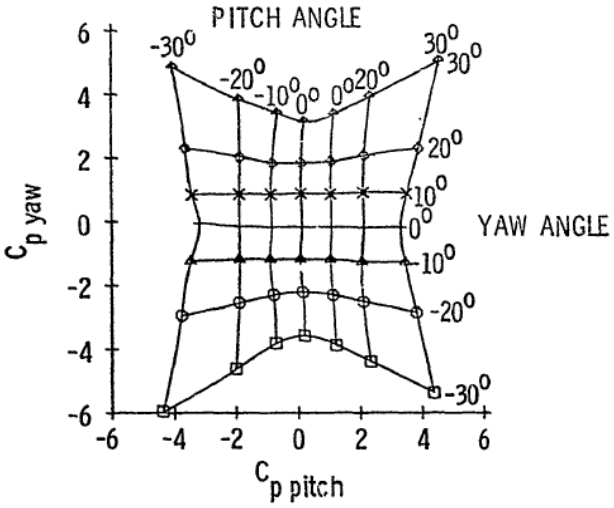

Figure 23 An example of calibration map is given: yaw angle and pitch angle are expressed as functions of Cp_{yaw} and Cp_{pitch}. Taken from Treaster [50]

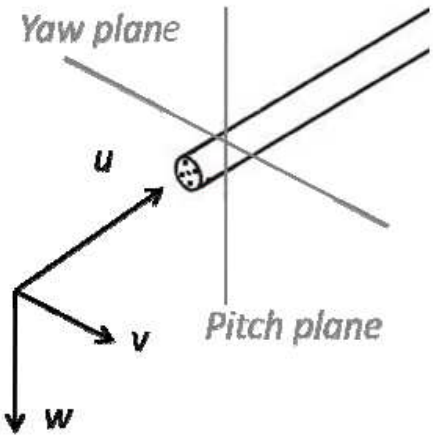

Figure 24 Velocity decomposition in 5-hole probe data, taken from Stein [45]

1.6.2 Particle Image Velocimetry (PIV)

1.6.2.1 PIV Vs Stereoscopic PIV

Particle image velocimetry (PIV) is a non-intrusive technique to measure components of flow velocity. The seeded flow region of interest is illuminated by means of a pulse source of light and pairs of images are taken with a known time delay Δt using a digital camera which is placed orthogonally to the light sheet. Using particular algorithms, based on statistical analysis, the images are correlated to return a velocity vector plot. During the correlation the image at time t is compared to that at time t+Δt and the displacement of the tracing particles which scatter the light is estimated and by means of the time interval between each frame (Δt) the local flow velocity is calculated. Defining **d** the particle image displacement between a pair of images with components d_x, d_y, d_z, and **D** the particle displacement in the physical space with components D_X, D_Y, D_Z, the velocity magnitude is evaluated by:

$$|\boldsymbol{V}| = \frac{|\boldsymbol{d}(\Delta t)|}{M\Delta t} = \frac{|\boldsymbol{D}(\Delta t)|}{\Delta t} \tag{1.52}$$

where M is the magnification factor of the camera lens. After the correlation the vectors are validated and a velocity vector plot output. The system so described, which is illustrated in Figure 25, allows measurement of two components of the velocity that lie in the plane of the light sheet. The out of plane component cannot be evaluated. This component evidently affects the particle image displacement, adding an out-of-plane displacement that cannot be measured. This effect introduces an uncertainty in measuring the in-plane velocity components. Indeed, the image displacement **d** corresponding to a certain particle displacement is given by (Raffel et al. [40]):

$$d_x = x_i' - x_i = -M\left(D_X + D_Z\frac{x_i'}{z_0}\right) \tag{1.53-a}$$

$$d_y = y_i' - y_i = -M\left(D_Y + D_Z\frac{y_i'}{z_0}\right) \tag{1.53-b}$$

where M is the magnification factor (Refer to Figure 26). As clear from the formulations the higher the out-of-plane displacement the bigger is the error made on the in-plane particle image displacements. According to Raffel et al.[40] this uncertainty

turns into a systematic error, a perspective error, which in certain situations can reach up to *15 %* of the mean flow velocity

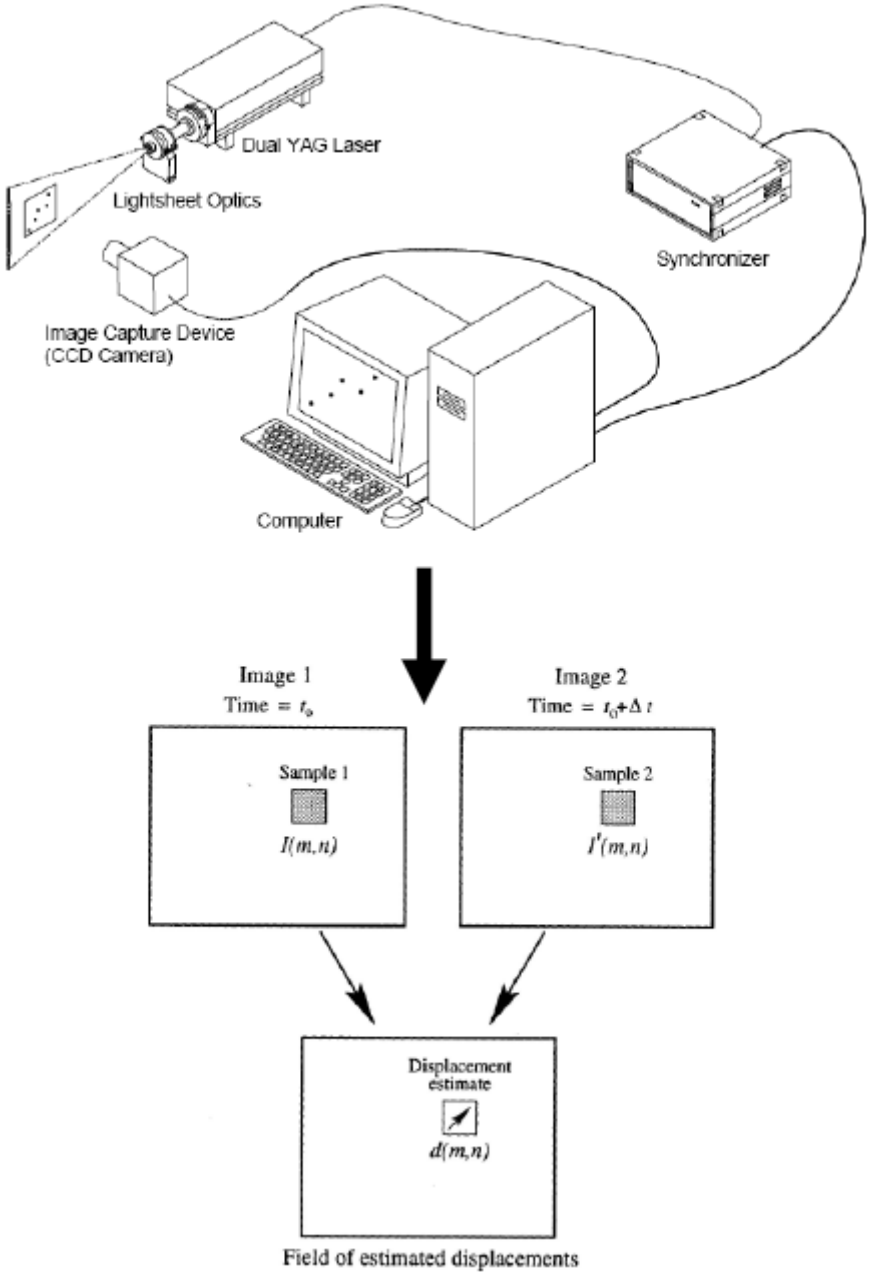

Figure 25 Sketch of a PIV system, taken from Dockrill [15]

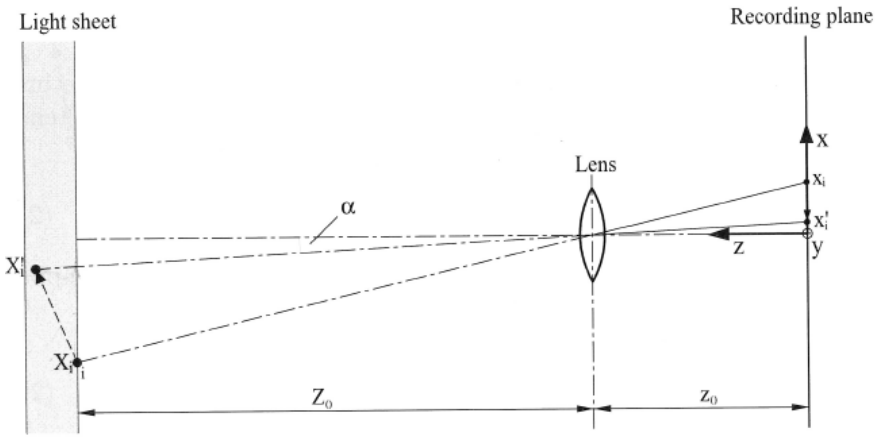

Figure 26 Imaging of a particle within the light sheet on the recording plane. Physical explanation of the perspective error. Taken from Raffel et al [40]

This limit of a classic PIV system (one recording camera) is overcome with a Stereo PIV (SPIV) system which adopts two recording cameras (see Figure 27). This system is able to evaluate the three components of the velocity u, v, w, eliminating the perspective error, but introduces a perspective distortion which must be calibrated.

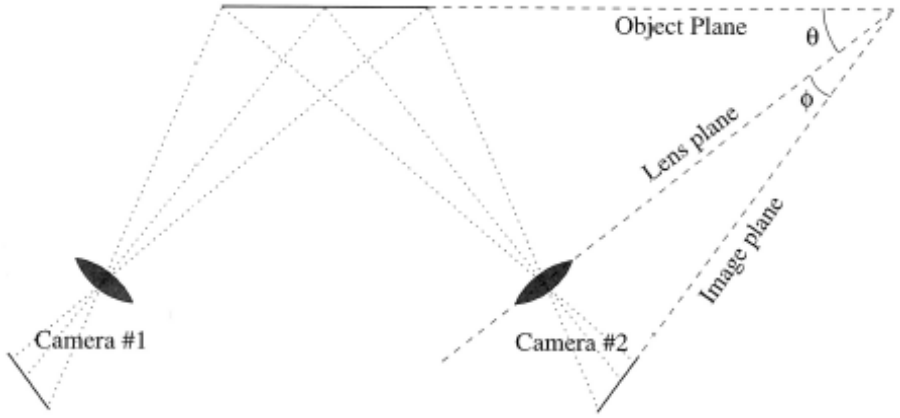

Figure 27 SPIV system configuration, taken from Raffel et al [40]

In a SPIV system each camera takes a pair of images from the region of interest with a Δt time delay. Each image pair then is correlated using correlation algorithms to return a 2D velocity vector plot. The three velocity components can be reconstructed, from the 2D vector plots obtained by the two cameras, using the following expressions:

$$u = \frac{u_1 \tan \alpha_2 + u_2 \tan \alpha_1}{\tan \alpha_1 + \tan \alpha_2} \qquad (1.54\text{-a})$$

$$v = \frac{v_1 \tan\beta_2 + v_2 \tan\beta_1}{\tan\beta_1 + \tan\beta_2} \quad (1.54\text{-b})$$

$$w = \frac{u_1 - u_2}{\tan\alpha_1 + \tan\alpha_2} \quad (1.54\text{-c})$$

where

$$\tan\alpha_{1,2} = \frac{x'_{i_{1,2}}}{z_0} \quad (1.55\text{-a})$$

$$\tan\beta_{1,2} = \frac{y'_{i_{1,2}}}{z_0} \quad (1.55\text{-b})$$

u_1, v_1 and u_2, v_2, are the velocity components measured respectively by the left camera and the right camera. α is the angle between the z axis and the ray from the tracer particle through the lens centre to the recording plane xz of each camera. β is defined accordingly in the yz plane per each camera (see Figure 28). According to the previous formulations the left side vector plot and right side vector plot are correlated to give back a 3D velocity vector plot.

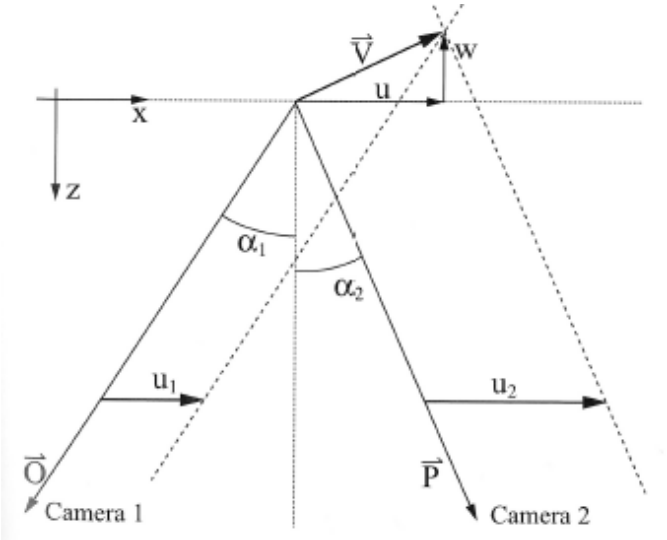

Figure 28 SPIV velocity reconstruction, taken from Raffel et al [40]

An accurate evaluation of highly three-dimensional flows, like vortex flow which is the object of the present study, where an intense out-of-plane velocity component is present requires use of SPIV devices otherwise a lack of precision will be in the evaluation of the velocity vector.

Since SPIV is able to evaluate the instantaneous velocity vectors, this technique is particularly suitable to the measurements of transient and/or turbulent flows, the latter being our case.

1.6.2.2 Characteristics of a PIV/SPIV system

In the previous section an overview of PIV was given. Finding velocities, perspective error and the need for a SPIV system for measuring highly 3D flows were discussed. In this section some technical aspects of a generic PIV measurement are given.

Two aspects are considered of great importance in a PIV measurement: (i) choice of seeding particles and (ii) light source.

- *Seeding Particles*

  Tracer particles are needed to evaluate the flow velocity. Since the flow velocity in a specific point is measured from the particle displacement within the flow, it is clear that the tracers must faithfully follow the motion of the fluid elements requiring small particles. The better the particles mix with the fluid the better they will follow the flow, thus is clear that small particles will follow the flow better. In contrast the particle image intensity and therefore the contrast of the PIV recordings is directly proportional to the scattered light power. In general it can be said that this quantity is a function of the particles size, shape and orientation (Raffel et al. [40]). Thus a compromise has to be found for the particles size. Also the density of the particles is of great importance and must be carefully chosen. It affects the way the images are processed.

- *Light Source*

  The region of interest must be illuminated by a high power light source, to catch the scattered light by the particles. Lasers are used for this purpose. They emit a monochromatic light beam with high energy density, which can be easily converted into light sheets for illuminating and recording the tracers, using lenses. Moreover the laser must be a pulse laser with short enough duration of the illumination pulse to “freeze” the motion of the particles, in order not to have strakes in the images recorded by the camera/cameras (Raffel et al. [40]). The

time delay between illumination pulses is also important, must be short enough to retain the seeding particles within the light sheet between pulses, but long enough to be able to evaluate the displacement between the particle images.

1.6.2.3 Processing the images

Processing the particle images is made breaking each image into small regions called *interrogation regions*. The size of these regions depends on the optical set-up and the spatial resolution required but is typically 32 x 32 pixels. Each Interrogation box is then processed into a velocity vector. The final result is a vector plot based on regularly or irregularly spaced data points.

Processing each interrogation region is made using algorithms which are based on one of the following approaches: particle tracking and spatial correlation analysis.

Particle tracking methods are based on locating every particle in the PIV images and paired up the particles. In this way the particle image displacement is calculated and from this the actual velocity vector. To do this with high accuracy the tracing particle density must be low so that the particles are correctly matched. Obviously this results in velocity data with low spatial resolution. In Figure 29a) shows a low image density requirements for processing by particle tracking methods.

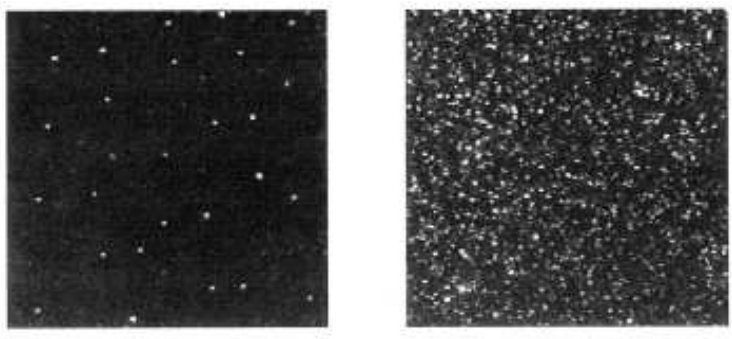

a) b)

Figure 29 Different particle image densities are presented: (a) typical image density for PTV; (b) typical required density for PIV correlation analysis. Taken from Raffel et al [40]

Spatial correlation analysis, involves finding a statistical pattern in the particle image displacement, in each interrogation region. As a result this method requires higher image density with respect tracking methods. One consequence is that the size of the resolution of the interrogation grid can be refined to obtain higher resolution velocity

data. For this reason these methods are the most used for PIV images processing. Figure 29b) presents a typical image density required for correlation analysis.

2 Methodology

There are three chronological steps that produce the research methodology: wing model design, experimental setup and data processing. Each of them is treated in a dedicated section in this chapter.

2.1 Model design

A flat plate delta wing was used as vortex generator [1.4.3]. The Smith theory was inversely applied to define the wing geometry from the ATTAS wake characteristics. Unfortunately the theory does not include prediction of the core radius. Also the vortex circulation, which could be estimated, strongly depends on the flow velocity, which under the constraint due to the ABL depends on the wing height within the wind tunnel. Thus the design is completely based on the initial vortex separation (b_0). The method for designing the delta planform follows the steps presented below:

- The sweep angle was arbitrarily fixed at *70°* to satisfy the Smith's theory hypothesis (slender wing) and to avoid vortex breakdown over the wing at relatively high incidence (Thomson [47] and Traub et al. [49]). As a result an apex angle of *40°* was obtained (2δ).

- A bevelling angle of *30°* was arbitrarily chosen because sharp leading edge condition ensures the best and the "cleanest" vortex generation.

- The ATTAS wake parameters were scaled with a scale factor (*f*) of *1/200* using the formulations presented in [1.4.3]. For an initial vortex separation of *17 m* taken from Figure 16, is obtained a scaled value (b_{0s}) of:

$$b_{0s} = f\, b_{ATTAS} = 0.085\, m \qquad (2.1)$$

- The ratio $e = \frac{tan\alpha}{tan\delta}$ was fixed at *0.91* since the experimental data appear to have the best agreement with the theory for this value (Smith [44]).

- From Figure 20 a ratio between the vortex lateral position and the half span of *0.7382* corresponds to *e=0.91*. From the known vortex separation the wing span is calculated by:

$$B_s = \frac{b_{0_s}}{0.7382} = 0.115\ m \tag{2.2}$$

- The chord is immediately found by:

$$c_s = \frac{B_s}{2}\tan\Lambda = 0.158\ m \tag{2.3}$$

- Finally a thickness of *3mm* was established.

Thus the wing geometry was completely characterised and ready to be manufactured. It was made in the Cranfield University workshop from a *3 mm* thick aluminium plate. The delta wing model design is presented in Figure 30.

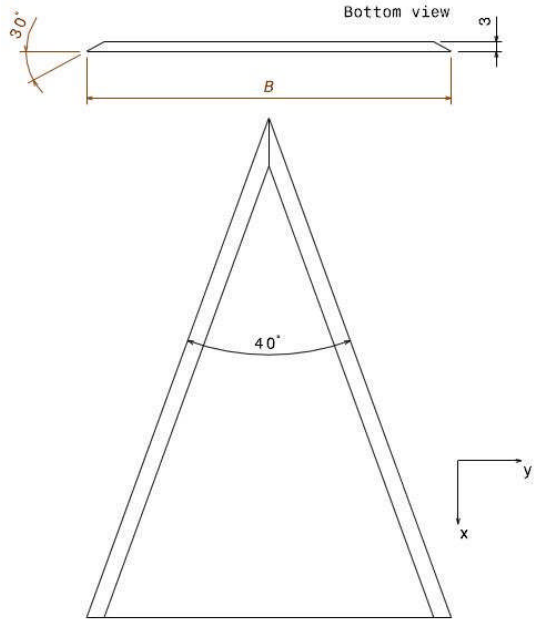

Figure 30 Wing model design

Parameter	Symbol	Value
Chord	c_s	158 mm
Span	B_s	115 mm
Thickness	s_s	3 mm
Sweep Angle	Λ	70°
Bevelling Angle	β	30°

Table 4 Wing model characteristics

It has to be borne in mind that for *a=0.91* and *δ=20°* the angle of attack (α) must be kept at *18.5°* and only if this is satisfied then the flow approximates the required condition. In Table 4 the wing parameters are summarised.

2.2 Experimental Setup

2.2.1 Five-hole probe

Measurements of local flow velocity components were taken over several transversal planes (y-z) downstream of the wing at three different wing heights. A five-hole probe, mounted on a traverse system able to move the probe in a way to design measurements grid fine up to *2 mm* step in both directions, was used. The probe was connected to five differential pressure transducers (*Furness Controls FC044, ±100 mmH2O*) which were interrogated by a computer via an A-D converter. The whole system included also a barometer for the evaluation of the atmospheric pressure, a thermometer and a Pitot-static tube, fixed at the wing height. For a finer characterization of the instruments used refer to Bernon [6]. In Figure 31 a sketch of the five-hole probe system is presented.

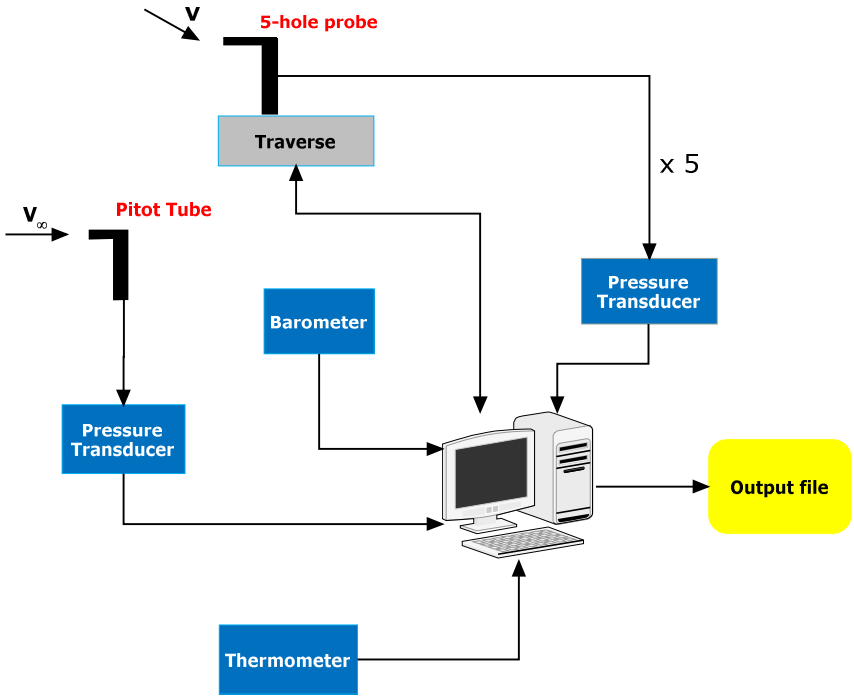

Figure 31 Sketch of the five-hole probe system

The computer controlled the data acquisition using software written in Labview running under Microsoft Windows. The program wrote the five readings of the pressure transducer, position of the probe and temperature in a *.txt* output file. To achieve maximum accuracy in the evaluation of the time average flow characteristics, the

system was set at *30 seconds* sampling time and *500 Hz*. Working in this way a relatively large amount of time would have been needed to acquire pressure data from a full plane (*30 seconds* per point plus *2-5 seconds* to move the probe to the next measurement point). To reduce the overall measurement time, only the flow behind the left wing side was investigated, assuming symmetry with respect the centreline of the wing.

Grids with square cells were adopted with step size and number of points dependent on the plane location. The closer the region being investigated was to the wing the smaller the grid size needed to capture the wake vortex, the finer the grid that could be adopted. Obviously, the number of grid points must be kept small enough not to increase significantly the evaluation time of the entire plane. Two cell sizes were used: *10x10mm* (for the planes closer to the wing) and *20x20mm* (for the planes farther from the wing). All the measurements were carried out running the wind tunnel at *400 RPM* to obtain the required ABL profile [1.3.2]. The measurements taken with acceptable vortex capture and used in the present analysis are reported in Table 5.

N°	$\frac{Height}{B_s}$	$\frac{x}{B_s}$	Grid size (mm)	Step size (mm)
1	0.93	0.18	70x70	10x10
2	0.93	1.50	80x80	10x10
3	0.93	2.62	100x180	20x20
4	0.93	3.74	120x180	20x20
5	0.93	5.61	120x180	20x20
6	0.93	7.48	120x180	20x20
7	0.93	9.35	140x160	20x20
8	1.50	0.18	70x70	10x10
9	1.50	1.50	80x80	10x10
10	1.50	2.62	100x180	20x20
11	1.50	3.74	140x200	20x20
12	1.50	5.61	140x200	20x20
13	1.50	7.48	140x200	20x20
14	2.24	-0.02	140x50	10x10
15	2.24	0.02	70x70	10x10
16	2.24	0.18	70x70	10x10
17	2.24	1.50	80x80	10x10
18	2.24	2.62	100x140	20x20
19	2.24	3.74	140x200	20x20
20	2.24	5.61	140x200	20x20
21	2.24	7.48	140x200	20x20

Table 5 Measurements taken with good vortex capture

2.2.2 PIV

Figure 32 shows the stereoscopic particle image velocimetry (SPIV) arrangement used to record the particle images. A Litron Nano 200mJ double pulsed Nd:YAG laser was used with a *-25mm* single light sheet optic in conjunction with a pair of TSI Powerview 4MP cameras. Seeding was provided by injection of Di-2-Ethylhexyl-Sebacat (DEHS) oil particles into the flow development section of the tunnel. This injection point provided sufficient time for the particles to mix adequately for high quality PIV images in the working section.

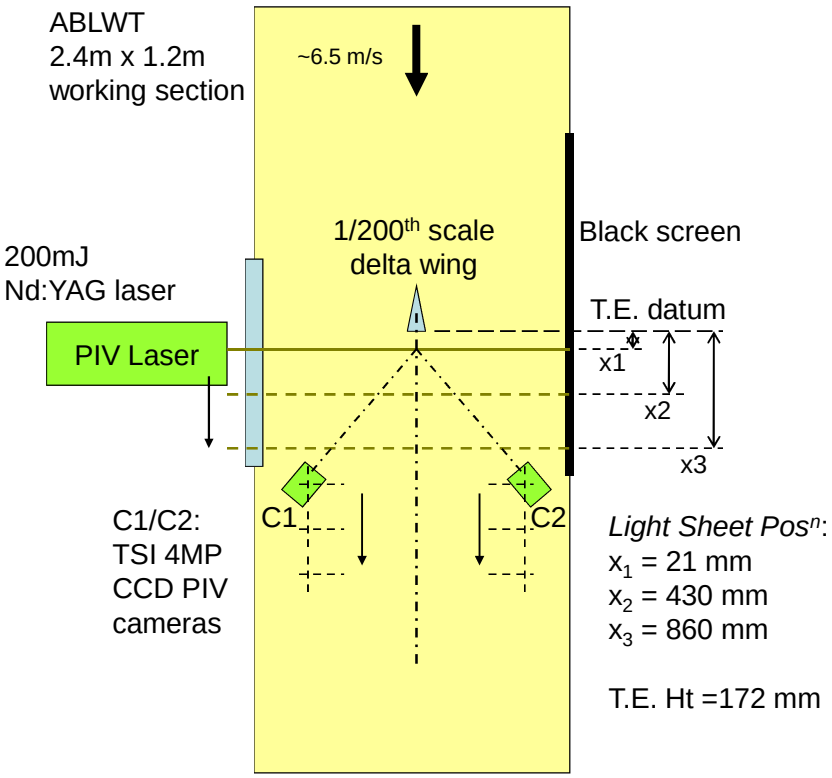

Figure 32 Schematic of the SPIV set-up in the ABLWT

The wing was fixed within the working section at the same angle of attack as for the five-hole probe measurements ($\alpha=18.5°$). The flow field was investigated over three planes at one fixed wing height. Planes position and wing height were chosen coincident with previous five-hole probe measurements so comparison is possible (see Table 6).

Height (H)	*Plane position (x)*
$1.5B_s$	$0.18B_s$
$1.5B_s$	$3.74B_s$
$1.5B_s$	$7.48B_s$

Table 6 Schedule of the PIV measurements

Per each run (measurement) 50 image pairs were taken (number of instantaneous flow evaluations). All the SPIV apparatus was controlled by TSI Insight 3G which then was used to process and post process the images in 3D velocity vector plots. A number of parameters have to be set up within the software regarding the camera setup, laser setup and timing setup. The timing setup parameters have a great importance in analysing the experimental data because they regard the way (timing) the flow is evaluated. Some of those parameters are reported with explanation below:

- ***PIV Frame Mode***: defines the number of frames the camera captures when it receives a trigger from the synchronizer. Two modes are available:
  - *single*: the camera acquires a single frame image
  - *Straddle*: the camera acquires two consecutive single exposure images
- ***Pulse Rep Rate (Hz)****:* it specifies the timing from the start of one laser pulse sequence to the start of the next laser pulse sequence.
- ***Laser Pulse Delay:*** pulse delay time is the amount of time to wait from the start of a laser pulse sequence to until the first laser pulse.
- ***Delta T (μs):*** pulse separation time

Refer to the Insight 3G user manual for a full description of all the parameters [52]. Table 7 below shows the values used for this study.

Parameter	*Value/mode*
Pulse Rep Rate	7.25 Hz
Laser Pulse Delay	305
Delta T	200 μs

Table 7 Timing parameters in the images capturing setup

2.3 Data processing

2.3.1 Five-hole probe data processing

The five-hole probe data were processed using a dedicated MATLAB program made up of three main sections.

1. The first part processes the five pressures collected by the five-hole probe in velocities by means of the method and formulations presented in [1.6.1.2-1.6.1.3]. It uses a calibration *.m* file containing the calibration data collected by Dockrill [15].

2. The second part calculates vorticity from the velocity data previously obtained. By means of the vorticity map, some vortex parameters are evaluated: maximum and minimum vorticity, location of maximum and minimum vorticity (y, z coordinates), centroid of vorticity (vortex centre), circulation and core radius (using the angular momentum definition). All of these parameters were calculated according to the formulations presented in [1.1.1].

3. The third section fits the velocity data to three different vortex models (refer to [1.1.5]): Vatistas, Lamb-Oseen and Burnham-Hallock.

The algorithm of the program is presented in flowchart form in Figure 33.

2.3.1.1 Evaluation of the integrals

Some of the calculations the code performs involve the evaluation of surface integrals. Since all flow variables are discrete functions (defined per points) of the position all the integrals require a numerical solution. In the present case four quantities require the solution of a double integral and these are the circulation, the core radius and the two vortex position coordinates, expressed respectively by formulas (1.3-5). The surface over which the integral is performed is considered to be made up of a number of cells. Each cell has an area (ΔS) equal to the product of the spatial step along y and along z ($\Delta S=\Delta y \Delta z$) of the grid where all the flow variables are defined. The integral is then converted into is numerical image which is the sum over the surface elements of the variable times the surface element itself. Below the numerical expressions for the

circulation and vortex centre position are reported; the core radius is calculated in the same manner.

Circulation

$$\Gamma = \oiint \omega_x dS = \sum_i \omega_{x_i} \Delta S \tag{2.4}$$

Vortex centre

$$y_c = \frac{1}{\Gamma} \oiint y \omega_x dS = \sum_i y_i \omega_{x_i} \Delta S \tag{2.5}$$

$$z_c = \frac{1}{\Gamma} \oiint z \omega_x dS = \sum_i z_i \omega_{x_i} \Delta S \tag{2.6}$$

The vorticity map used to perform those calculations was obtained by interpolating the vorticity matrix directly calculated from the experimental velocity data over a grid with *1 mm* step in both the plane directions no matter the initial spatial step of the measurements grid. When reducing the cell size the accuracy of the numerical solution increases. The interpolation was performed using a Matlab cubic interpolation function.

2.3.1.2 Data fitting

Fitting experimental data means to find those coefficients that make the fitting functions best approximate the data. The parameters that have to be determined in fitting vortex velocity data are the circulation (Γ) and the core radius (a). The best fitting parameters are found by means of an iterative method. The two fitting parameters are initialised to a reasonable value: the core radius is set to zero and the circulation is set to a fifth of the circulation directly calculated in the previous section. Then the initial values are increased by an increment to an upper limit that for the core radius is the length of the grid and for the circulation is twenty-five times the starting value. The increments were set to *0.1 mm* for the core radius and *0.001* m^2/s for the circulation. For every iteration a function (χ) is calculated as:

$$\chi = \sum_{i=1}^{N} \left(\frac{V_{\theta_{fitting}}(i) - V_{\theta_{exp}}(i)}{\sigma(i)} \right)^2 \quad (2.7)$$

where N is the number of grid points and σ is the standard deviation of the tangential velocity over the ith point given by:

$$\sigma(i) = \sqrt{\frac{\sum_{j=1}^{N} \left(V_\theta(j) - V_\theta(i) \right)^2}{N}} \quad (2.8)$$

Minimizing function χ, the best fitting to the experimental data is obtained.

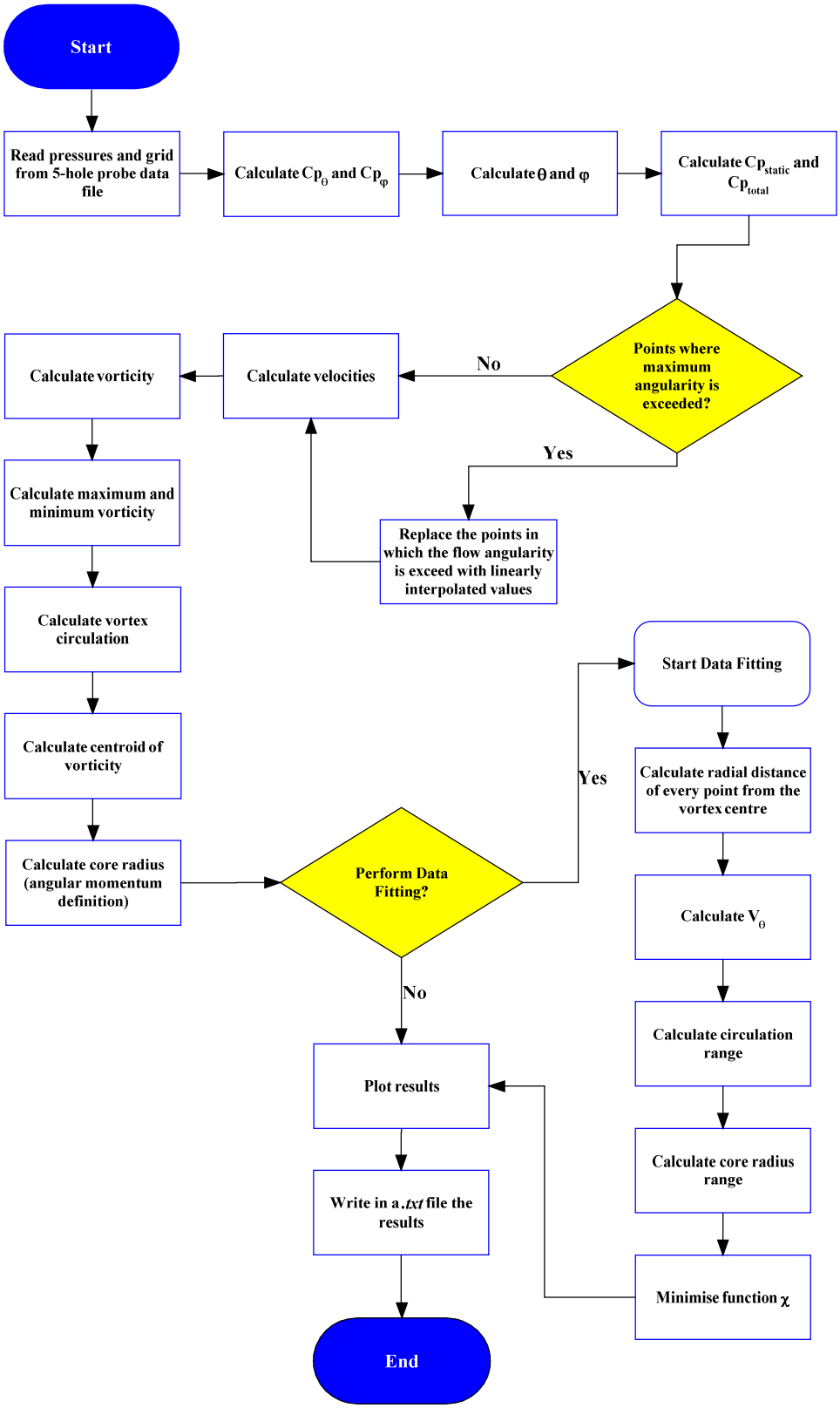

Figure 33 Algorithm of the code used to process the five-hole probe data

2.3.2 PIV data processing

The particle images were processed into 3D velocity vector plots with TSI Insight 3G using iterative grid FFT algorithms. The data was validated using a local median validation method of Insight 3G. The method consists in evaluating a reference vector as the median value of all vectors in the neighbourhood and comparing each vector of the same neighbourhood with the reference one. The dimension of the neighbourhood must be setup as well as the tolerances (maximum difference between the current vector and the reference vector) generally based on the flow characteristics. The invalid vectors are replaced by the local median vector. The 3D velocity data first visualised with Tecplot is then imported in an *.m* file used as input by two dedicated Matlab programs which further process the data.

1. *Average Field Processing Code*

   First, the program reads from an *.m* file time average velocity data and mesh. Second, it fills the eventual gaps present in the velocity field, with linearly interpolated values (this step is a further validation at the beginning of the program). Then it processes the velocities in vorticity and calculates the vortex parameters (maximum and minimum vorticity, and their position within the computational grid, vortex and box circulation, centroid of vorticity and core radius). Finally, if needed, it performs data fitting to Vatistas, Lamb-Oseen and Burnham-Hallock models. The structure of the code is very close to that of the five-hole probe data processing code (Figure 33) except for the section reading from the input file. Figure 34 shows the procedure in flowchart form for processing PIV data.

2. *Turbulence Statistics Code*

   Similarly to above it reads from an *.m* file the velocity data and mesh, but in this case the input file contains every instantaneous field obtained by SPIV measurement within the same experiment. Each instantaneous field is placed in a matrix which represents the flow field at a specific time. All the matrices form a three-dimensional array where the third dimension is time. After reading this “large” input file the program re-organizes the data in a suitable way to be analysed and then checks each realization of the flow against possible points in which the velocity is not defined. If it finds gaps or non-real values those are replaced with linearly

interpolated values. Then it performs calculation of the turbulence statistics variables of the flow field. It computes the turbulence velocity fluctuations using formula (1.15), the three components of turbulence intensity (I_u, I_v, I_w) according to formulation (1.16), the turbulent kinetic energy (k) using formula (1.17) the correlation lengths (formula (1.21)) and the six independent components of the Reynolds stress tensor which is given by:

$$R^T{}_{ij}(\boldsymbol{x}) = \overline{u'_\iota(\boldsymbol{x},t)u'_\jmath(\boldsymbol{x},t)} \tag{2.9}$$

Since the Reynolds stress tensor is symmetric, it is necessary to calculate only six of the nine components it is formed by. The average used to calculate all the turbulence statistics is the time average defined by formula (1.14). The integral is evaluated by the program using the well established trapezium rule using as time step the time interval elapsed between each evaluation of the instantaneous field by the SPIV system. At the time of capturing the particle images some important parameters have been fixed. One of these is the *"pulse rep rate"*. Because within each laser pulse sequence a pair of images per each camera is collected which after correlation returns one 3D vector field the frequency of laser pulse sequence equals the number of flow field evaluation per second. Inverting this frequency the time step is obtained. Finally the program plots all the statistic quantities and then performs calculations over the mean flow field following the same procedure as the previous program (*Average Field Processing Code*).

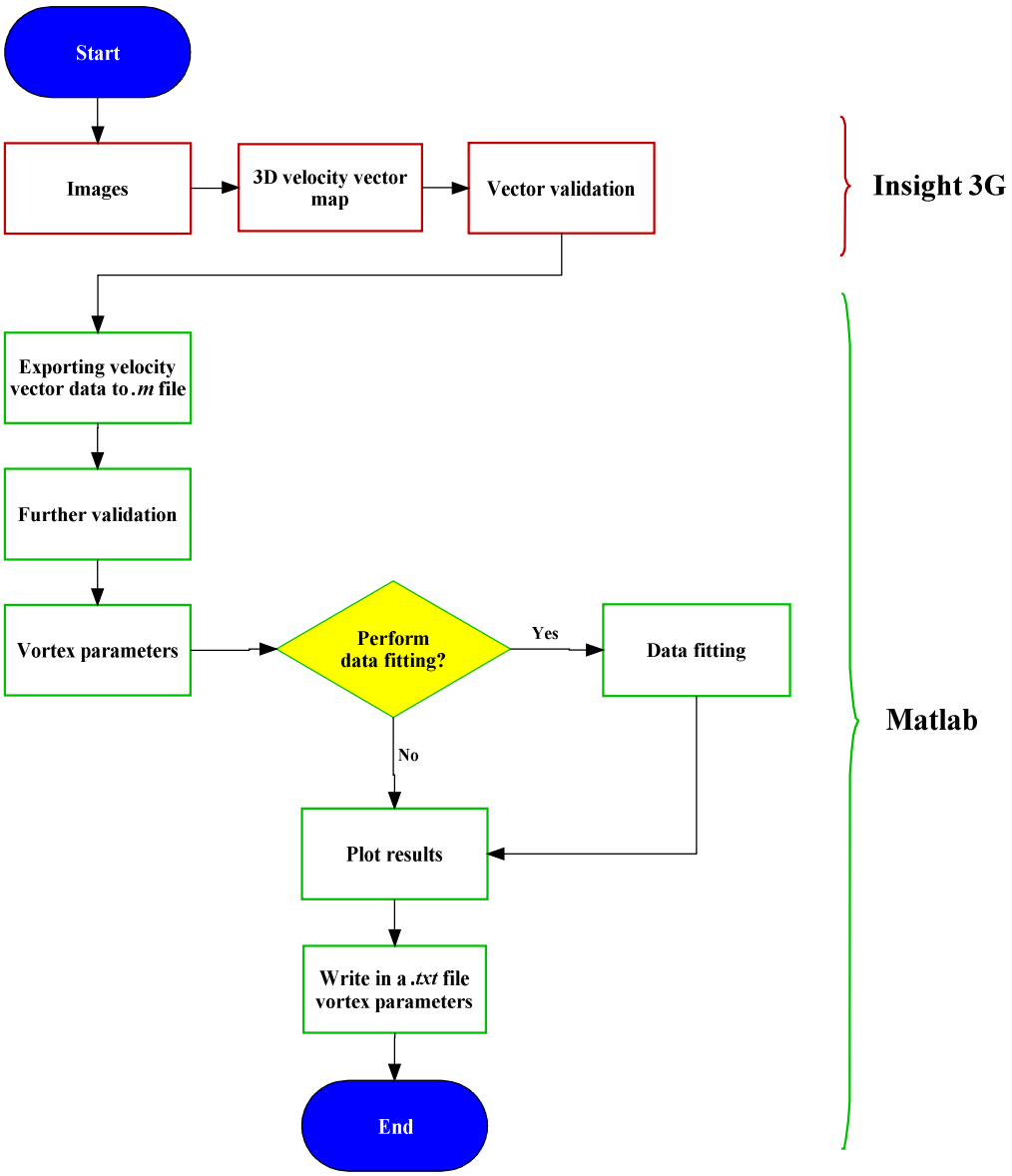

Figure 34 PIV average field processing algorithm

3 Five-Hole Probe Results

This chapter shows the five-hole probe measurements results. Those are used to discuss three main subjects: vortex structure and characteristics, Smith's theory validation and wake vortices dynamics in ground effect. Each one is treated in a dedicated paragraph.

3.1 Data presenting

All the results presented within the present chapter are *cubic interpolated* using a built in Matlab function. Since the grids used to carry out the measurements have relatively large spatial steps (*10 or even 20 mm*) the results would have an angular aspect which does not correspond to the reality of the analysed phenomenon. In contrast the actual flow is characterised by continuous and regular variables. To aid understanding, Figure 35 shows a comparison between the cubic interpolated vorticity map and the correspondent vorticity map not interpolated for the wing height $H=1.5B_s=172mm$ over the plane located at $x=2.62B_s=301mm$. This measurement was arbitrarily chosen as an example.

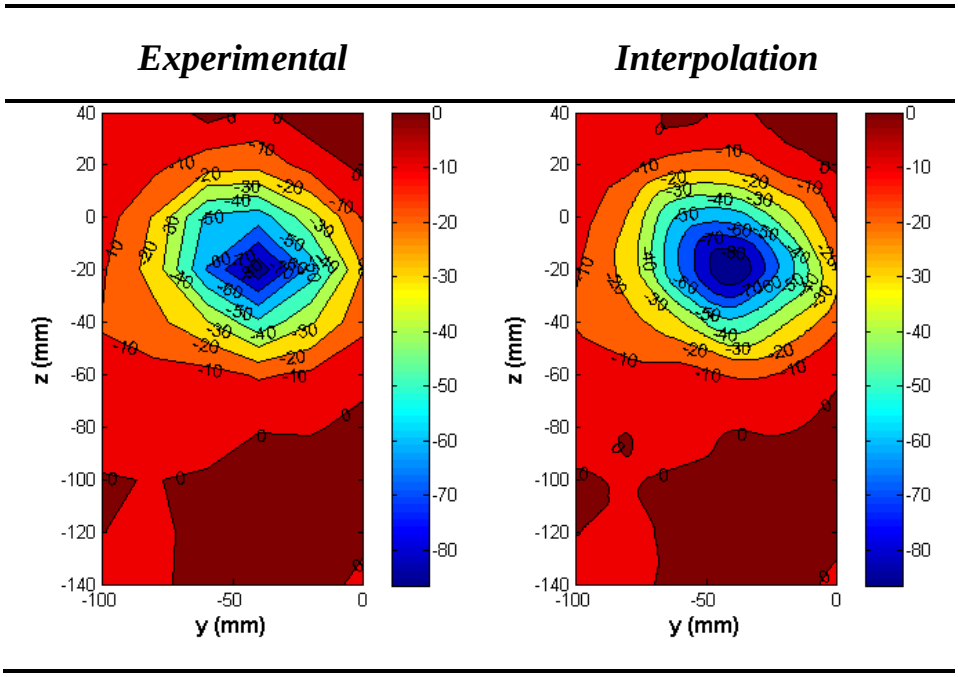

Figure 35 Comparison between not interpolated results (left) and cubic interpolated results (right)

3.2 Wake configuration: Smith's theory validation

The wake obtained at the trailing edge of the wing is made up of two pairs of counter-rotating vortices, (one each side of the wing). Each one contains a primary vortex and a secondary vortex. Figure 36 shows the left side of the flow *2 mm* outboard the trailing edge: the negative vortex (on the top) is the primary vortex, the positive one (bottom) is the secondary that will rapidly dissipate leaving in the wake only a pair of counter-rotating vortices which we are interested in studying.

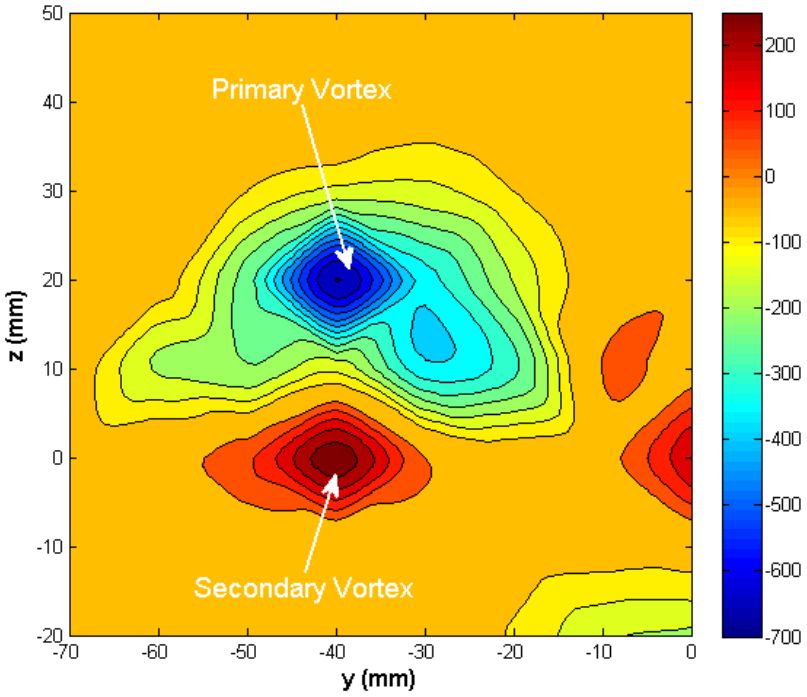

Figure 36 Vorticity map 2 mm outboard the wing

This result in conjunction with a full measurement of the flow *2 mm* inboard the trailing edge (Figure 37) was used to compare with the prediction of the theory given by Smith [44]. Neither plane corresponds exactly to the wing trailing edge, but it is assumed that the vortices do not change significantly when moving *2 mm* downstream so the mean position can be compared with that predicted by theory. Figure 37 shows the whole flow field over the delta wing; the negative vorticity region (on the left hand side) and positive vorticity region (on the right hand side) correspond to the primary vortices. The flow field appears to be asymmetric about the wing axial centre line (*y=0*). It is assumed that this asymmetry is due to a slight mis-alignment of the wing with the free

stream flow direction. Also the vortices appear to be cut over the wing surface, this is due to the impossibility of investigating the flow too closely to the wing model to avoid the probe could touch its upper surface. Correlating this data gives an initial vortex spacing (b_0) of *78-80 mm.* The error made in the prediction with respect the ATTAS scaled vortex separation (b_{0s} = *85 mm*) is then *6 - 8 %.*

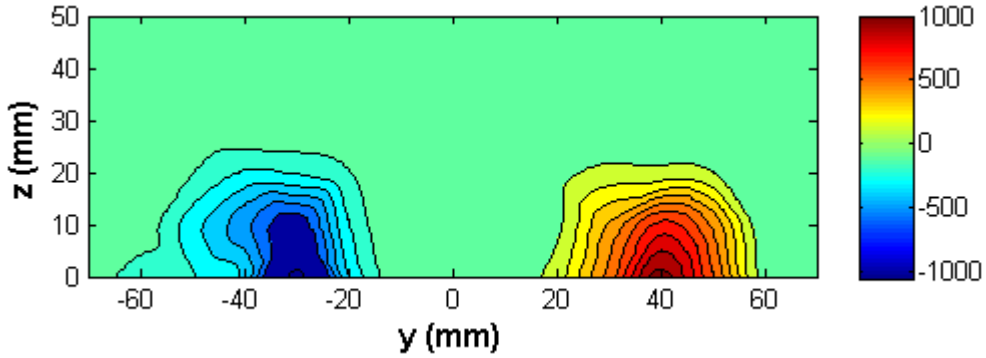

Figure 37 Vorticity map 2 mm inboard over the wing

3.3 Vortex structure and characteristics

An assessment of the vortex characteristics was made using data taken over the plane located at $x=0.18B_s=21mm$ for a wing height of $0.93B_s=107mm$. Typical and expected vortex structure was obtained, characterised by high concentration of vorticity (Figure 38-top left) and high gradients in the core region which induce a region of recirculation (Figure 38-top right) that affects the whole flow field even relatively far away from the vortex centre. The vorticity plot shows two discrete vortex structures of opposite sign. The larger and stronger (blue) is the primary vortex, whereas the other (dark red) weaker and compressed just beneath the first one is assumed to be what remains of the secondary vortex. The latter, due to its weakness, dissolves quickly and is undetectable farther downstream. The vortex structure is then characterised by a drop in pressure and out of plane velocity (u) in the core region due to the partial transfer of the fluid motion and energy from the x-z plane to the y-z plane. This is presented in terms of static pressure coefficient (Figure 38-down left) whereas Figure 38-down right shows the distribution of out-of-plane velocity.

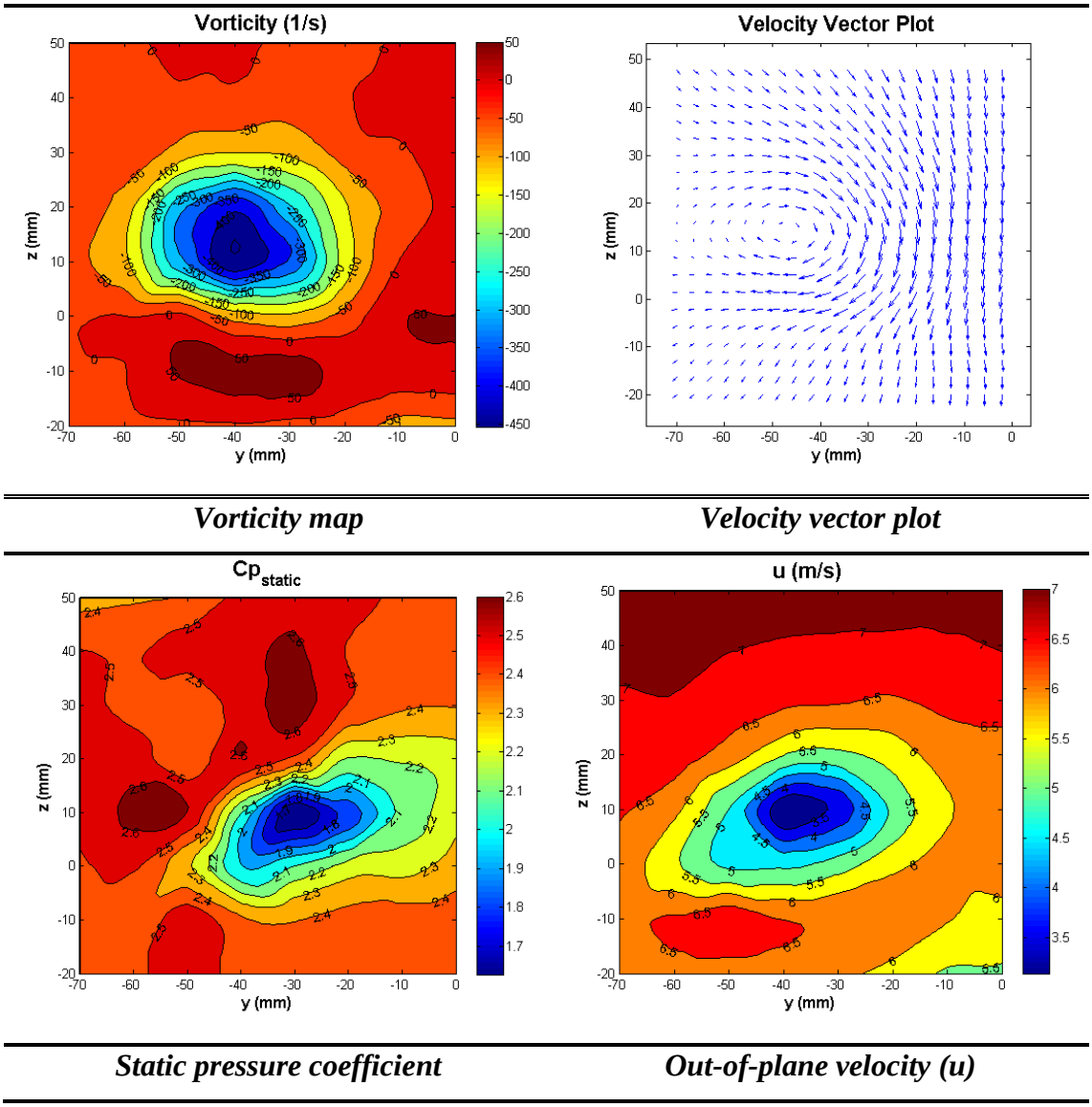

Figure 38 Vortex characteristics. H=0.93B_s plane located at x=0.18B_s

The vector plot also shows a strong asymmetry mainly with respect to the vertical plane. This is assumed to be due to the presence of the primary vortex, of opposite sign generated by the right side of the wing with which it interacts. A weaker asymmetry is evident with respect to the horizontal plane possibly due (at this stage) to the secondary vortex. The overall strong asymmetry affects the possibility of successfully fitting the experimental data to well established vortex models. Indeed those are based on functions with radial symmetry. As a result the data points which do not follow a radial symmetry appear to be spread over the plane r- V_θ (radial distance-tangential velocity) and the models cannot realistically fit the data. Figure 39 shows an example of data fitting.

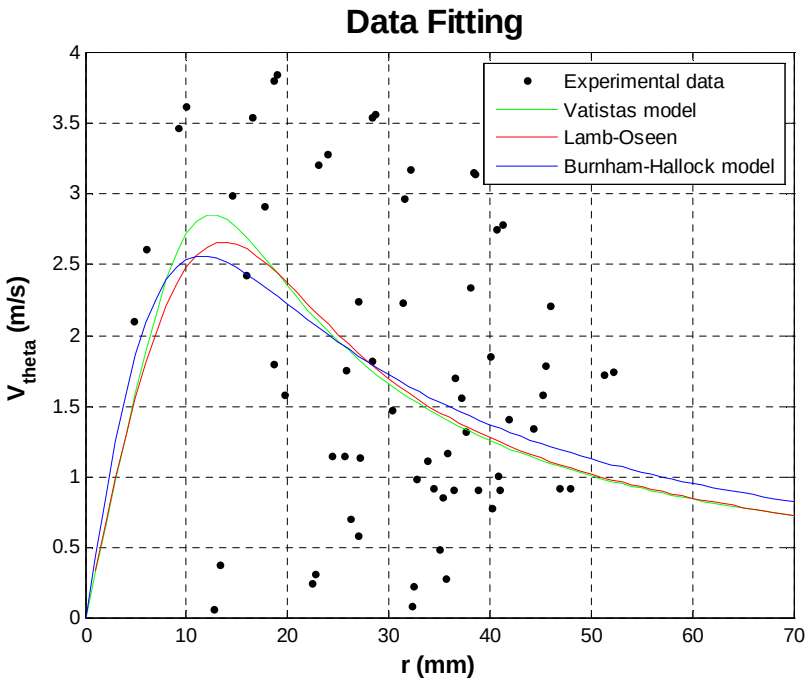

Figure 39 Data fitting to three vortex models. Black points correspond to experimental data points; the green line is the Vatistas model; the red line corresponds to Lamb-Oseen model; blue line is the Burnham-Hallock model

3.4 Wake vortices in ground effect

This 5-hole probe data set was used to investigate the dynamics and space evolution of the mean flow in ground proximity within a scaled model of the ABL. Therefore some conclusions will be drawn.

The vortices are seen to sink behind the wing as expected due to the mutually induce downward velocity. The secondary vortex initially present in the region close to the trailing edge has disappeared one and half wing span downstream. The maximum vorticity dramatically reduces as the vortex system moves downstream of the wing due to viscous effects and at the same time the core radius linearly increases. As the wing height approaches the ground the vortex evolution is not seen to change significantly. Only the initial values of circulation and maximum vorticity change due to the different freestream velocity fields. In particular the closer the wing to the ground the lower its maximum vorticity and circulation, as consequence of the velocity decrease due to the boundary layer profile. Table 8 shows the vorticity space evolution for two wing heights: $H=0.93B_s$, and $H=2.24B_s$.

	$H=0.93B_s=107mm$	$H=2.24B_s=258mm$
$x = 0.18B_s=21$ mm	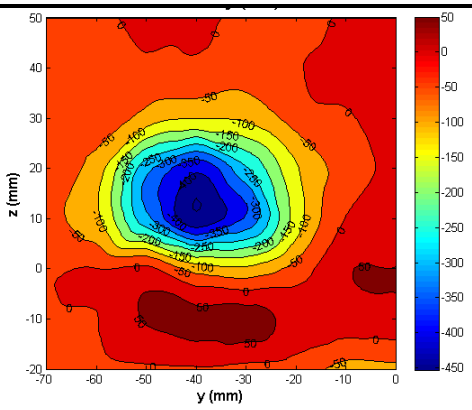	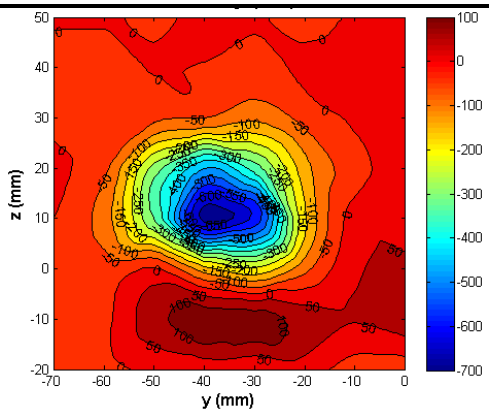
	$\Gamma = -0.31\ m^2/s \quad \lvert\omega\rvert_{max} = 453.1\ s^{-1}$	$\Gamma = -0.37\ m^2/s \quad \lvert\omega\rvert_{max} = 672.5\ s^{-1}$
$x = 1.50B_s = 172$ mm	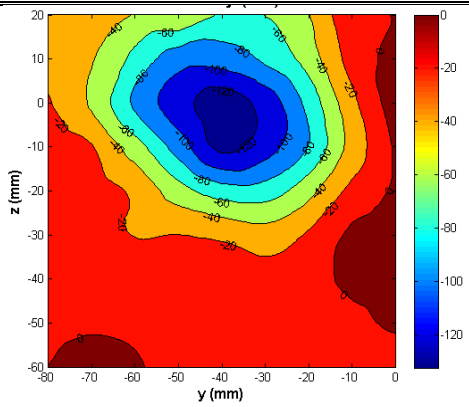	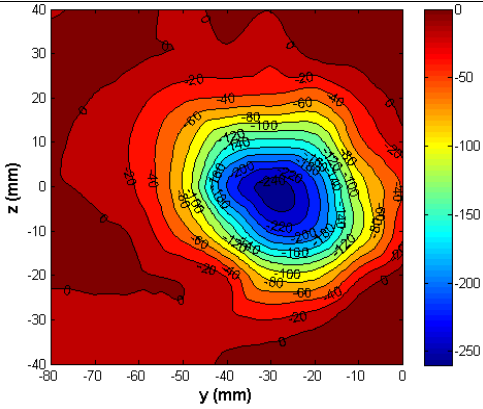
	$\Gamma = -0.23\ m^2/s \quad \lvert\omega\rvert_{max} = 132.4\ s^{-1}$	$\Gamma = -0.27\ m^2/s \quad \lvert\omega\rvert_{max} = 251.6\ s^{-1}$
$x = 2.62B_s = 301$ mm	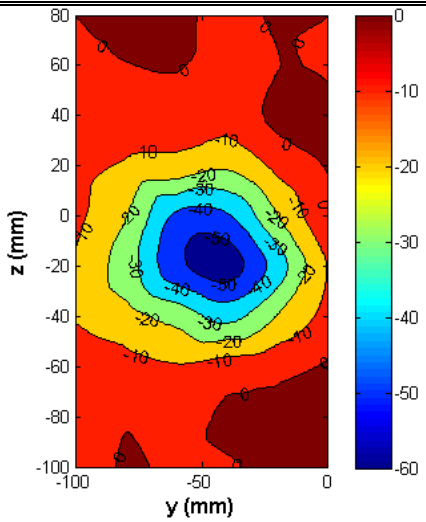	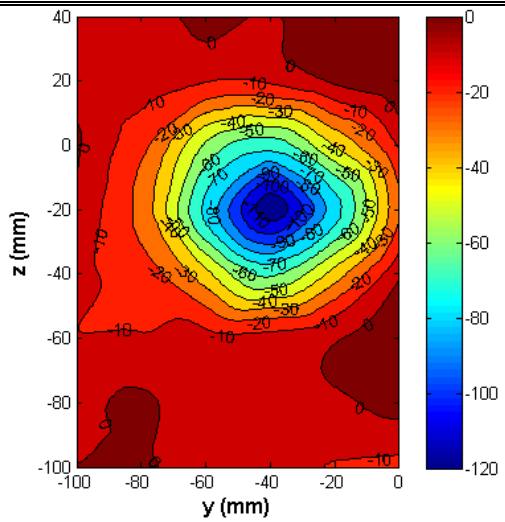
	$\Gamma = -0.21\ m^2/s \quad \lvert\omega\rvert_{max} = 55.2\ s^{-1}$	$\Gamma = -0.29\ m^2/s \quad \lvert\omega\rvert_{max} = 114.5\ s^{-1}$

$x = 3.74B_s = 430$ mm	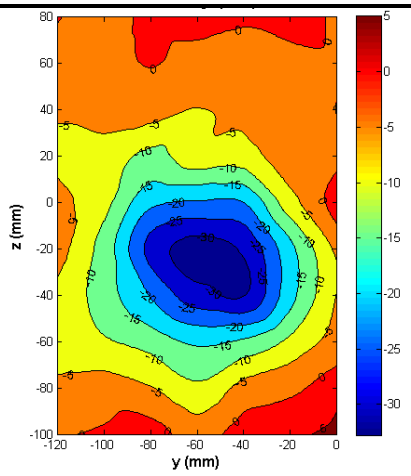	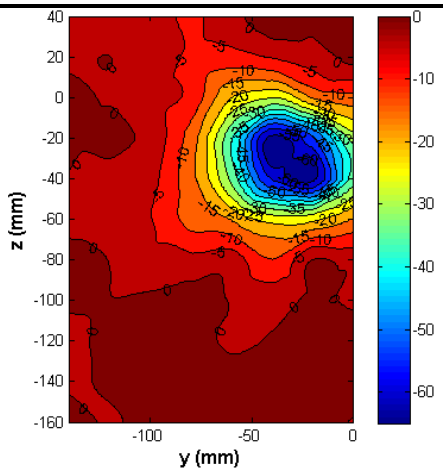
	$\Gamma = -0.18\ m^2/s$ $\quad \lvert\omega\rvert_{max} = 32.8\ s^{-1}$	$\Gamma = -0.23\ m^2/s$ $\quad \lvert\omega\rvert_{max} = 64.2\ s^{-1}$
$x = 5.61B_s = 645$ mm	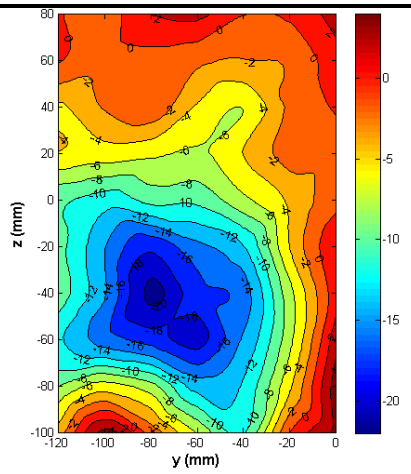	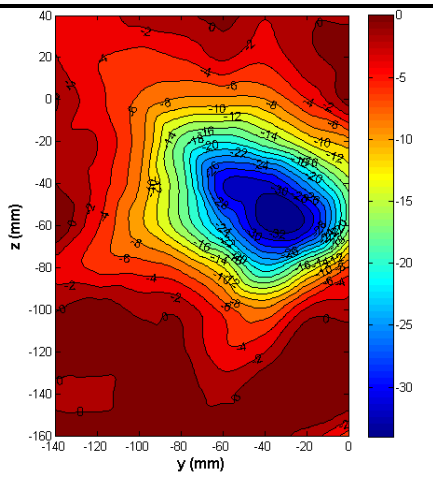
	$\Gamma = -0.15\ m^2/s$ $\quad \lvert\omega\rvert_{max} = 20.4\ s^{-1}$	$\Gamma = -0.19\ m^2/s$ $\quad \lvert\omega\rvert_{max} = 33.8\ s^{-1}$
$x = 7.48B_s = 860$ mm	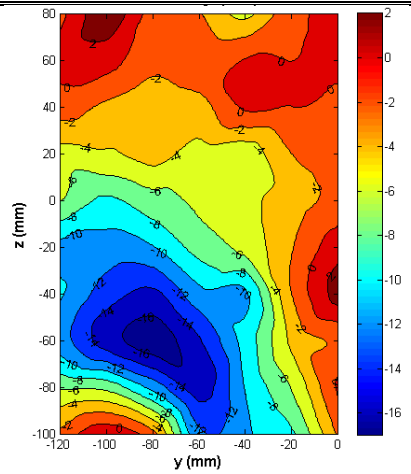	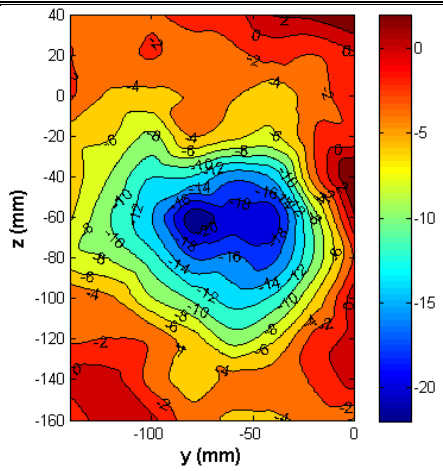
	$\Gamma = -0.12\ m^2/s$ $\quad \lvert\omega\rvert_{max} = 17.0\ s^{-1}$	$\Gamma = -0.17\ m^2/s$ $\quad \lvert\omega\rvert_{max} = 21.1\ s^{-1}$

Table 8 Vorticity evolution for two initial wing heights: H=0.93B_s and H=2.24B_s. Flow field over six different vertical planes is shown up to a distance downstream equal to 7.48B_s

From Table 8 two aspects have to be stressed:

(i) The vortex remains coherent as it moves downstream for wing height $H=2.24B_s$ than for $H=0.93B_s$ (see last two planes). At $x=7.48B_s$ for $H=0.93B_s$ the vortex almost reaches the ground and it distorts possibly due to the presence of an opposite vorticity distribution consequence of the boundary layer separation at the ground. However no vortex rebound, mentioned by Harvey & Perry [23] was observed.

(ii) The vortex for $H=0.93B_s$ starts progressively diverging just after its formation whereas for $H=2.24B_s$ the diverging phase begins some spans downstream.

According to Sarpkaya [42] a system of wake vortices is in ground effect when its height above the ground is equal or less than $1.5b_0$, Proctor [38] suggests that the critical height is less than $1.0b_0$. Thus for the wing fixed at $H=0.93B_s$ the vortex system can be considered in ground effect whereas for the other two heights the vortex system at the formation time is not in ground effect yet. The results show that the ground proximity strongly affects vortex descent and lateral position. Figure 40 shows the vortex centre lateral displacement.

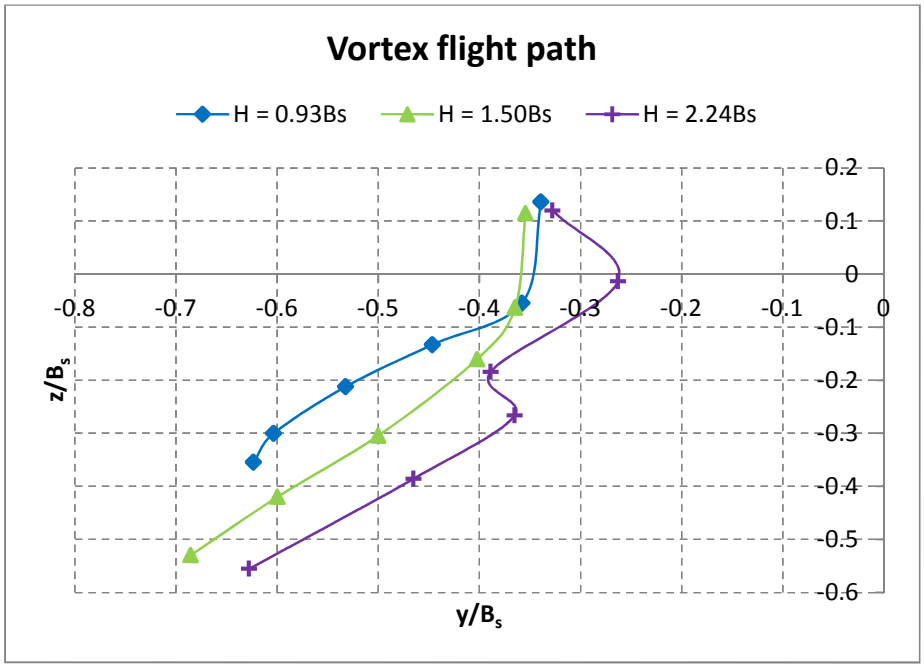

Figure 40 Vortex flight path along y in the wing reference system for three different wing heights

It seems from Figure 40 that the smaller the vortex system initial height the greater is the displacement of the vortex core from the axial centre line (*y=0*). This may be due to the relatively high lateral velocity components (v) in the region between the vortex core and the ground (Figure 41).

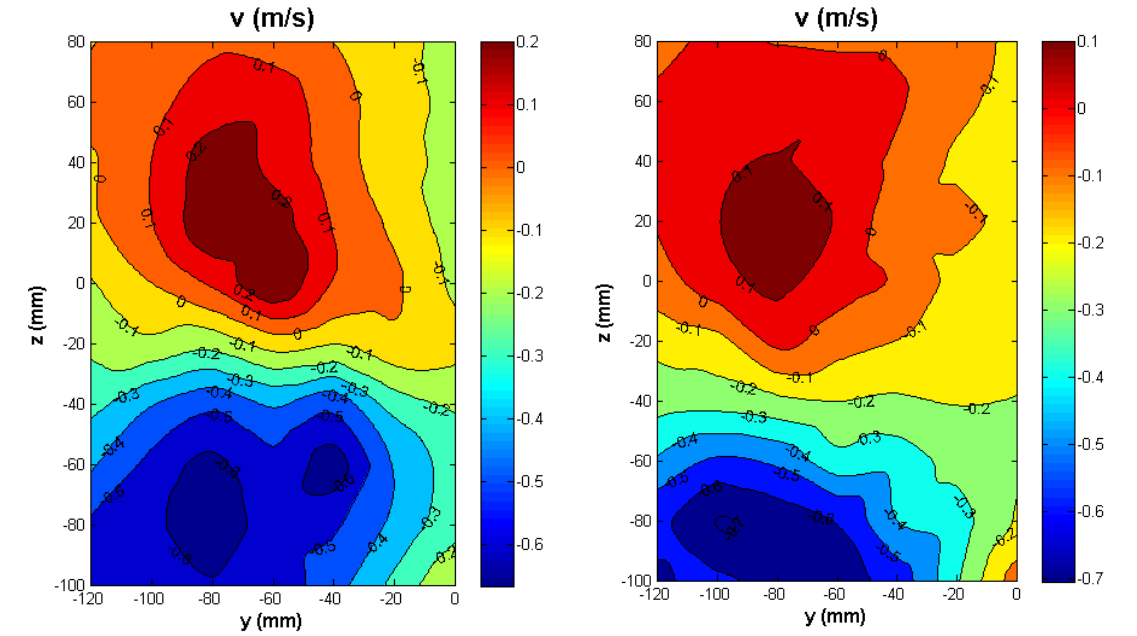

Figure 41 Velocity component along y (v) over two planes for the case H=0.93B$_s$

The distribution of lateral velocity component (v) should ideally be symmetric with respect the y axis translated in the vortex reference system in free air. This phenomenon leads to the possibility of the formation of a concentration of opposite vorticity over the ground: a secondary opposite vorticity distribution has to exist to verify the no-slip boundary condition at the ground. This new vorticity distribution eventually would increase the local velocity beneath the primary vortex. Unfortunately it was not possible to verify this as the minimum height achievable by the probe was *7 mm*.

As previously stated the vortex system is seen to descend downstream of the wing. The rate of descent appears to decrease as the initial height of the vortex system approaches the ground. The descent tends to flatten over the x axis but vortex rebound

was not observed. The location of the vortex core relative to the wing trailing edge with distance downstream (x) is shown in Figure 42.

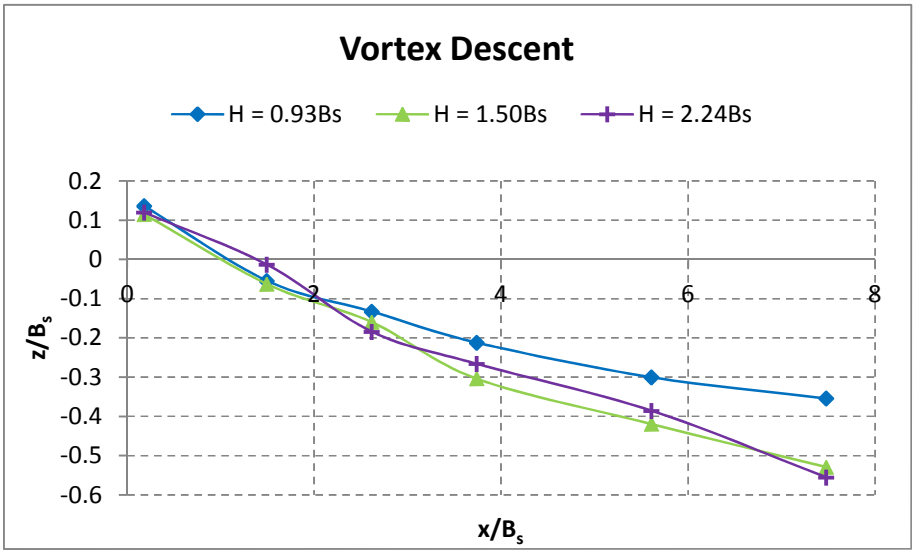

Figure 42 Vortex descent in the wing reference system for three different wing initial heights

In terms of circulation and vorticity decay ground effect appears less clear. It seems that the maximum vorticity, as the vortex is moving downstream, is not affected by ground proximity. It is to be expected that the lower the initial height the lower the maximum vorticity and the faster it decays. This is a combined effect of the Reynolds number and the turbulence profile the vortex is subject to, within the atmospheric boundary layer, see Figure 43.

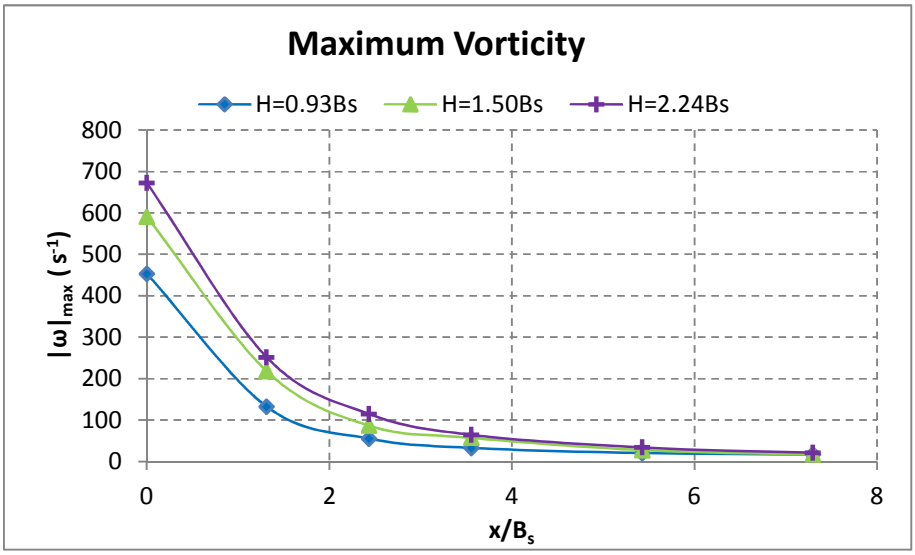

Figure 43 Maximum vorticity decay (vortex reference system)

On the other hand circulation was recognized to have a linear trend in the ground effect region ($H=0.93B_s$) in agreement with Sarpkaya's model ([42]) as well as out of ground effect ($H=1.50B_s$ *and* $H=2.24B_s$). In Figure 44 circulation is interpolated to a straight line for different heights. The best fitting is for the data set correspondent to the height $H=1.50B_s$ however the other two data sets are well represented by a straight line.

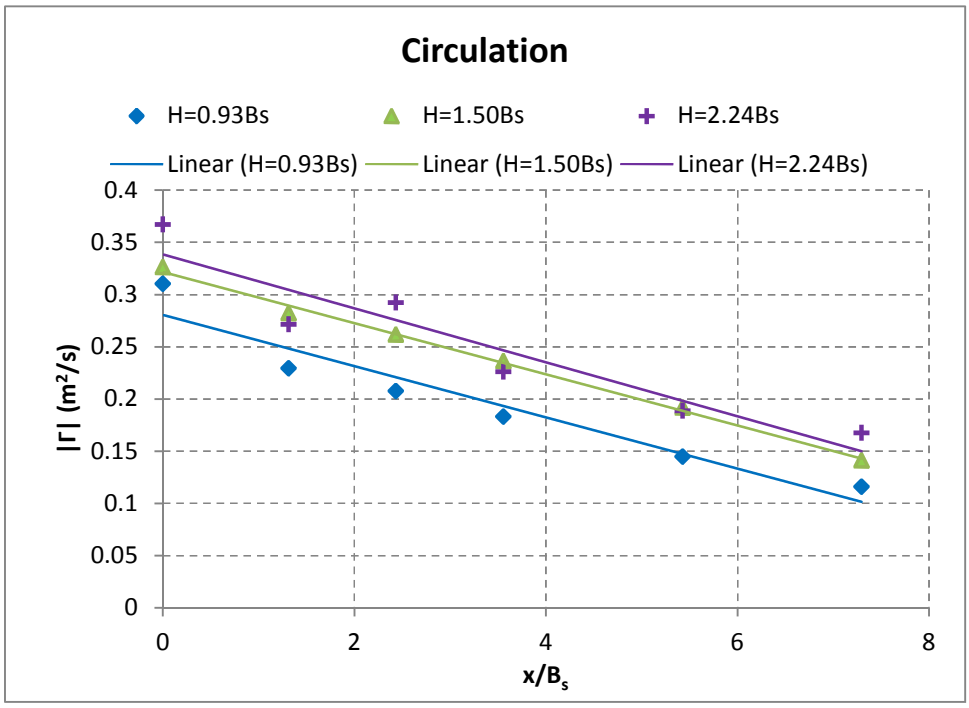

Figure 44 Circulation decay for three wing initial heights (vortex reference system)

The straight lines are given by the following equations:

$$\Gamma = -0.024x + 0.280 \quad \rightarrow \quad for\ H = 0.93B_s \qquad (3.1\text{-a})$$

$$\Gamma = -0.024x + 0.321 \quad \rightarrow \quad for\ H = 1.50B_s \qquad (3.1\text{-b})$$

$$\Gamma = -0.025x + 0.338 \quad \rightarrow \quad for\ H = 2.24B_s \qquad (3.1\text{-c})$$

Apparently the circulation decays with approximately the same slope for the three cases analysed whereas we would expect the decay be enhanced moving the initial vortex system toward the ground due to the higher turbulence intensity, being represented by the following general expression:

$$\Gamma(x) = -f(\varepsilon^*)x + \Gamma_0 \quad \rightarrow \quad up\ to\ H \cong 3b_0 \qquad (3.2)$$

where $f(\varepsilon^*)$ is a function of the turbulence parameter introduced in [1.2.3]. This result is in contradiction with the definition of ground effect region given by Sarpkaya [42] and Proctor [38]. Based on the circulation data obtained, this region seems to extend up to $3b_0$ for the model studied.

The last topic to discuss is the core radius evolution with distance downstream (x) for the three wing heights (Figure 45).

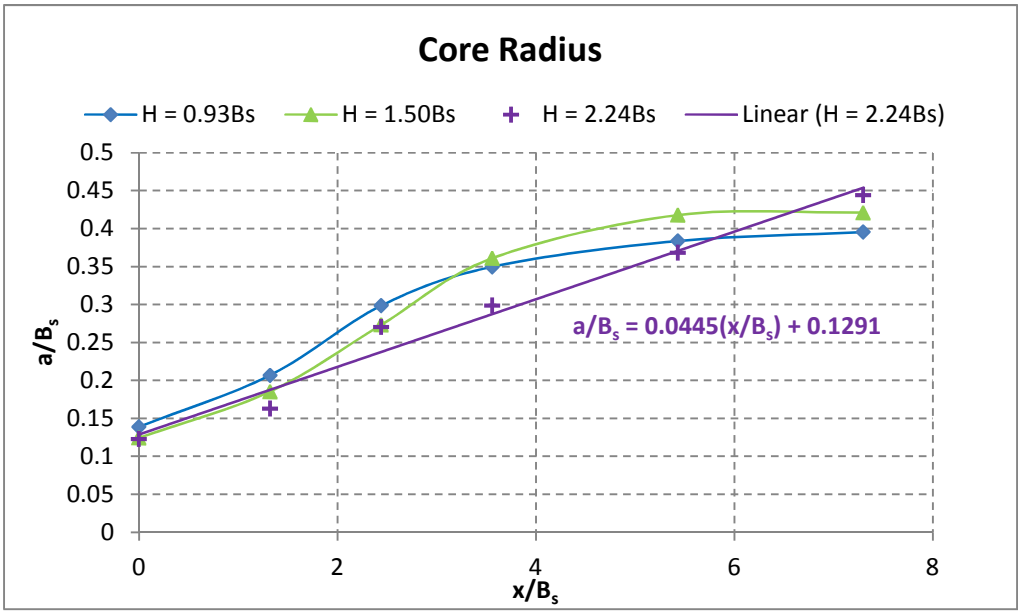

Figure 45 Vortex core radius against distance downstream for three wing initial height (Vortex reference system)

The core radius in all of the cases studied increases as normally does due to the diffusive effect of the viscosity. In general it can be said that the core radius grows as a function of the vortex Reynolds number as previously analysed by Fonti [20] and Orlandi [34]. The Reynolds number can be explained as the ratio between the Inertia force and the viscous force acting on the fluid elements. As a result at higher Reynolds number the system tends to keep its condition of motion longer than at low Reynolds numbers in which cases the viscous force is dominant and makes the system dissipating its energy faster. In our cases (three wing heights) the initial vortex circulation slightly changes and so the Reynolds number does. As consequence it is not possible to clearly understand the core radius evolution against the Reynolds number variation, but apparently something can be said about the ground effect on its behaviour. For the wing height $H=2.24B_s$ the vortex system is out of the ground effect region and it never enters

in this region at least in our range of measurements (flow field investigated up to $x=7.48B_s$). In this case the data points appear to be well fitted to a straight line and its equation is reported in Figure 45. On the other hand for the other two heights the core radius initially increases quickly then its rate of growing progressively decreases tending to flatten in the x axis direction. This effect is thought to be due to the ground proximity but more measurements are needed to confirm this preliminary interpretation.

Further Five-hole probe results (velocity components plots and pressure plots) are discussed in Appendix A.

4 Results Comparison

The present chapter is divided in two distinct sub-sections. The first one introduces an inviscid model for vortex trajectory in ground proximity, the second shows a series of results comparison with theoretical/empirical models and further experimental data found in literature.

4.1 Vortex sheet approximation of the ground

After analysing the five-hole probe data presented in the previous chapter it was intended to model the motion of a generic pair of vortices in ground proximity. Thus the aim was to find a mathematical expression able to describe, with good accuracy, the trajectory of any possible pair of vortices. Few models addressing this problem were found in the literature and all of them appear to be particularly complex to implement, see for example Atias & Weihs [3], although the results compared to the experimental data appear to be accurate. The present study points to model the problem of motion of vortex systems in the early stages of the ground effect (highest layer of the ground effect region).

4.1.1 Model structure

The first stage in building the model was to make some assumptions over the flow structure. A pair of wake vortices can be seen either as a three-dimensional steady flow or as a two-dimensional unsteady flow (Puel [39]). In the present case the complex three-dimensional flow is considered as unsteady two-dimensional in the transversal plane (y-z) downstream the wing. Thus the time evolution of the flow over a section orthogonal to the axis of the wake is considered. The wake is assumed to be symmetric with respect the centreline of the wing and made up of two counter rotating vortices that descend due to the mutual induced velocity. Each vortex is assumed to have two distinct regions: inner region (core) and outer region. The inner region is the region where most of the vorticity is concentrated and where the viscous effects are dominant. The outer region, much larger than the first one, is almost irrotational and can be well

approximated with an inviscid flow solution. As a result the flow in the outer region is considered to behave as a point vortex.

As previously analysed, in ground effect region the wake interacts with the ground and over the ground a cross-flow boundary layer creates and eventually separates generating a region of opposite vorticity, a secondary vortex. The formation of the boundary layer is connected to the generation of a layer of opposite vorticity lying over the ground. The present approach is based on simulating the vorticity layer on the ground with an infinite vortex sheet. The wake vortex flow is then built as follow. The ground is replaced by an infinite vortex sheet of intensity $\gamma(y)$ (which must be evaluated) and the real viscous descending vortices are replaced by infinite long straight vortex filaments. Figure 46 shows a schematic representation of the flow.

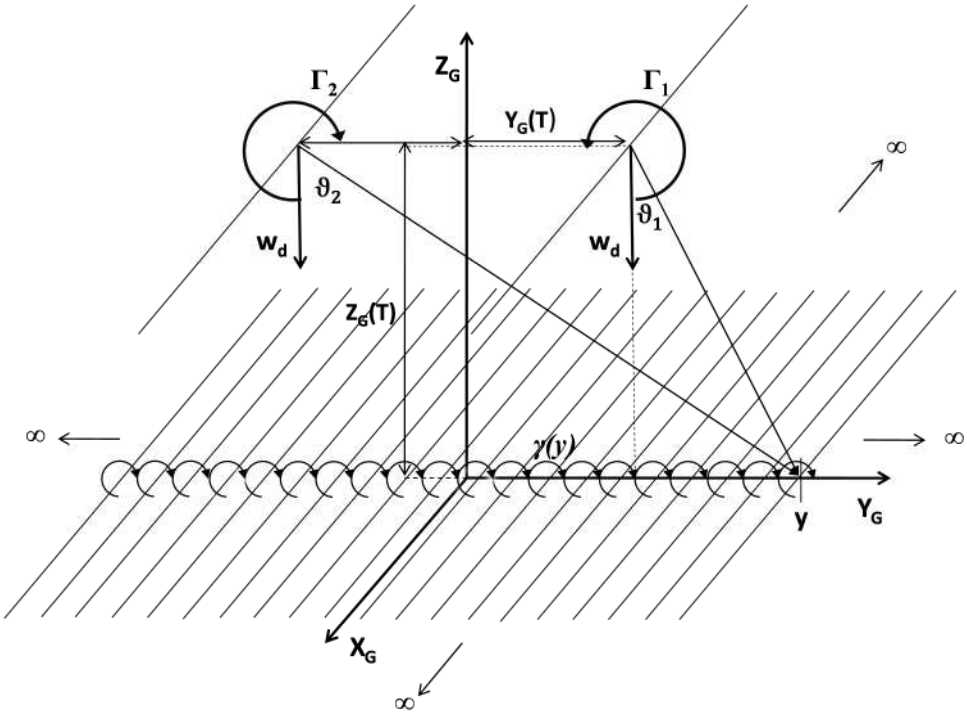

Figure 46 Sketch of the inviscid flow structure correspondent to the real vortex flow

Each section orthogonal to the vortex filament presents the same flow and is identical to the flow field induced by a point vortex (Lamb [51] - Anderson [1]). Thus we consider the flow in the y-z plane. Refer to Figure 46 for the notation used in following calculations and velocity decomposition.

The vortex sheet intensity γ(y) must verify the condition of zero velocity normal to the ground:

$$w_G = 0 \tag{4.1}$$

This means that no fluid particles can cross the ground, which would be physically impossible, and that the ground line is a streamline, which is compatible with an inviscid model.

If the vortex sheet strength is known it is possible to evaluate the velocity induced by the vortex sheet on the descending vortices and so calculate the trajectory of the vortices from the following first order differential system:

$$\begin{cases} \dfrac{dY_G}{dT} = v\big(Y_G(T), Z_G(T)\big) \\ \dfrac{dZ_G}{dT} = w\big(Y_G(T), Z_G(T)\big) \end{cases} \rightarrow \quad \begin{cases} Y_G(0) = Y_0 \\ Z_G(0) = Z_0 \end{cases} \tag{4.2}$$

v and w are functions of the vortex sheet strength so first of all the procedure to calculate it must be explained.

The ground is subject to the vortices induced velocity and the vortex sheet self-induced velocity: these are functions of the point considered on the ground. Since (4.1) must be verified, the sum of the orthogonal components of the velocities induced by the sheet and vortices must equal zero:

$$w_G = w_{vort1-G} + w_{vort2-G} + w_{sheet-G} = 0 \tag{4.3}$$

where the velocity component induced by the vortices on the ground and that one induced by the vortex sheet on the ground itself are respectively:

$$w_{vort1-G} = \frac{\Gamma}{4\pi Z_G(T)} \sin 2\vartheta_1 \tag{4.4-a}$$

$$w_{vort2-G} = -\frac{\Gamma}{4\pi Z_G(T)} \sin 2\vartheta_2 \tag{4.4-b}$$

and

$$w_{sheet\_G} = \int_{-\infty}^{\infty} \frac{\gamma(y')}{2\pi(y-y')} dy' \tag{4.5}$$

ϑ_i can be expressed as function of Y_G and Z_G. Thus by means of (4.4-5) and expressing ϑ_1 and ϑ_2 by:

$$\vartheta_1 = \tan^{-1}\left(\frac{y - Y_G(T)}{Z_G(T)}\right) \tag{4.6-a}$$

$$\vartheta_2 = \tan^{-1}\left(\frac{y + Y_G(T)}{Z_G(T)}\right) \tag{4.6-b}$$

equation (4.3) becomes:

$$\int_{-\infty}^{\infty} \frac{\gamma(y')}{(y-y')} dy' = -\frac{\Gamma}{2Z_G(T)}[\sin 2\vartheta_1 - \sin 2\vartheta_2] \tag{4.7}$$

This is a Volterra integro-differential equation of the first kind (Tricomi [51]). Since this equation depends on the vortex position which is time-dependent it is clear that the vortex sheet intensity must be re-evaluated at each time step. Indeed the condition (4.1) must be verified at each time. Once evaluated γ(y) the velocity induced by the entire vortex sheet on the right side descending vortex can be calculated as:

$$v_{sheet-vort1} = -\int_{-\infty}^{\infty} \frac{\gamma(y)\cos^2\vartheta_1}{2\pi Z_G(T)} dy \tag{4.8}$$

and

$$w_{sheet-vort1} = -\int_{-\infty}^{\infty} \frac{\gamma(y)\sin 2\vartheta_1}{4\pi Z_G(T)} dy \tag{4.9}$$

The component along z of the vortex sheet induced velocity is expected to be small whereas the main contribute to the descending velocity is due to the opposite side vortex. By hypothesis the two vortices behave in the outer region like point vortices so the velocity induced by the left side vortex on the right side one and vice versa is given by:

$$w_{21} = w_{12} = w_d = -\frac{\Gamma}{2\pi b(T)} = -\frac{\Gamma}{4\pi Y_G(T)} \tag{4.10}$$

The differential system (4.2) becomes:

$$\begin{cases} \dfrac{dY_G}{dT} = v_{sheet-vort1} \\ \dfrac{dZ_G}{dT} = w_d + w_{sheet-vort1} \end{cases} \tag{4.11}$$

The system (4.11) has to be integrated numerically and at each time step the vortex sheet strength has to be re-calculated integrating equation (4.7).

4.1.2 Model validation

To validate this vortex sheet model the differential system was solved by a dedicated Matlab program which uses the Euler's method for solving the time integration. All the integrals are evaluated using the trapezium rule.

First the model was solved for the wing height $H=0.93B_s$. In this case the vortex system initial height is equal to $1.07B_s \approx 1.57b_0$ thus the vortices are about to enter the ground effect region which according to Sarpkaya [42] begins at $z_G/b_0=1.5$. The model was solved in non-dimensional form using as initial condition the following values:

$$\begin{cases} Y_G(0) = 0.50 \\ Z_G(0) = 1.57 \end{cases} \tag{4.12}$$

All the variables were non-dimensionalised according to Table 9 below.

Variable	Symbol	Value
Descent	Z_G	z_G/b_0
Lateral Displacement	Y_G	y_G/b_0
Time	T	tV_0/b_0
Circulation	Γ*	$\Gamma/V_0 b_0$

Table 9 Non-dimensionalisation procedure

In Table 9 V_0 is the initial descending velocity of the vortex pair (see formula (1.36))

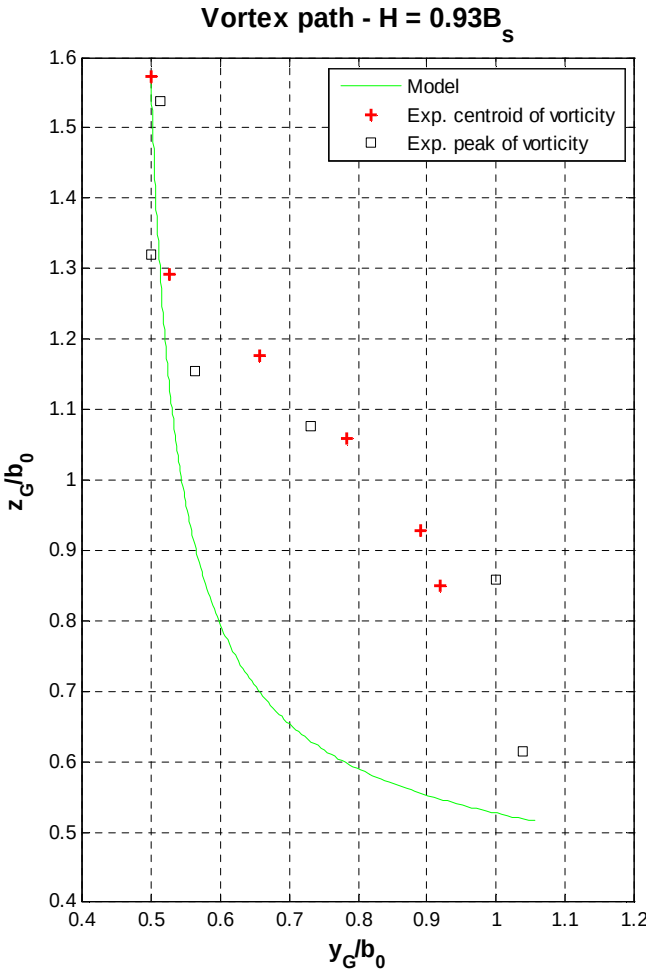

Figure 47 Predicted vortex trajectory versus experimental results

Although the model predicts the diverging and descending motion of the vortices, it fails in predicting their exact position as shown in Figure 47, which shows the right side vortex path. In particular except for the first two experimental points the predicted trajectory (green line in the graph) is considerably far from the other measurements. The model overstates the descent and understates the lateral displacement.

Figure 48 shows the vortex sheet intensity profile versus the span-wise direction (y). The graph exhibits two relatively high and sharp peaks exactly beneath the vortices which are responsible for the vortices lateral displacement. In fact these peaks induce a relatively strong velocity field just beneath the vortices recreating that region of flow

acceleration which is characteristic of the real viscous flow, as analysed in Chapter 3. The vortex sheet keeps the same shape as the solution marches in time but its peaks move following the vortices in their lateral shifting. At each time iteration γ(y) is recalculated and its peaks (negative and positive) are always found under the vortices.

Figure 48 Vortex sheet intensity for $H_0=1.57b_0$ at T= 1.5

However as seen in Figure 47 the vortex sheet simulation does not agree with the experimental results. Two reasons can be identified as responsible for the disagreement. First the simulation does not take into account the boundary layer profile and distribution of vorticity associated to it. Second and main reason, the model is made using the superimposition principle starting from basic inviscid flow structures that are the vortex filament and the vortex sheet. In this way we are assuming that the flow is mainly dominated by linear effects. Evidently the real viscous flow is governed by highly non linear phenomena. But this is not surprising since it is well known that the equations of fluid dynamics, namely the Navier-Stokes equations, are highly non-linear.

4.2 Sarpkaya's model

Comparing the experimental results to the Sarpkaya's model (section [1.2.3]) required some reasonable assumptions over the flow in the ABLWT working sections. Those hypotheses, discussed below, are needed to solve the model equations and overcome the absence of some key parameters.

1. The stratification parameters (N*) or Brunt–Väisälä frequency is a function of the potential temperature (Θ) and is given by:

$$N^* = \sqrt{\frac{g}{\Theta}\frac{d\Theta}{dz_G}} \tag{4.13}$$

Since the scale model of the ABL is considered not to have a temperature profile along z the partial derivative in (4.13) equals zero so does N*. As consequence the equation for the vortex descent (formula (1.39)) becomes:

$$\frac{d^2 Z_v}{dT^2} + \frac{C}{T^*} e^{-\frac{C}{T^*}T} = 0 \tag{4.14}$$

This is a second order ordinary differential equation that can be easily solved and this is the equation we refer to until the end of this section.

2. The calculation of the turbulence dissipation rate given by (1.37) requires the knowledge of the turbulence fluctuations throughout the flow field. Since this data was not available for the tunnel used in this study we assumed the *1/200th* scale model of the ABL to equal the correspondent model given by ESDU. Assuming the production of turbulence kinetic energy (TKE) in the region near the ground equal to the dissipation of energy via viscosity effect (Townsend [48]) the dissipation rate (ε) can be expressed as function of the velocity gradient along z by (Counihan [9]):

$$\varepsilon = \frac{\tau}{\rho}\frac{\partial u}{\partial z_G} = \frac{u^{*3}}{k_a z_G} \tag{4.15}$$

The skin friction velocity (u_*) can be evaluated according to formulation (1.26) where in this case V_{10} is the reference velocity at an height of *0.05 m*, being the

ABL geometrically scaled. Thus V_{10} becomes $V_{0.05}$ and the roughness parameter z_0 consequently scaled becomes $z_{0s}=z_0/200$. The reference speed was calculated according to:

$$V_{0.05} = V_{0.107}\frac{ln\frac{0.05}{z_{0s}}}{ln\frac{0.107}{z_{0s}}} = 5.86\ m/s \tag{4.16}$$

where $V_{0.107}$ is the measured velocity using a Pitot tube at *0.107 m*. From this reference velocity a skin friction velocity of *0.404 m/s* was obtained. Using formula (4.15) the dissipation rate of turbulence at the required heights was calculated.

3. The vortex system is considered to be initialised in a strong turbulent environment characterised by a turbulence dissipation rate calculated at the wing height which is approximately the initial height of the vortex system.

Based on these hypotheses the turbulence dissipation rate was calculated for each wing height tested, and from this value the turbulence parameter (ε*), which appears in Sarpkaya's model, was evaluated according to the formulation below:

$$\varepsilon^* = \frac{(\varepsilon b_0)^{\frac{1}{3}}}{V_0} = \frac{2\pi b_0(\varepsilon b_0)^{\frac{1}{3}}}{\Gamma_0} \tag{4.17}$$

Three values of the turbulence parameter were calculated and are reported in Table 10 together with the estimated values for ε and the values of circulation and vortex separation used to perform the calculations.

Height	b_0 (mm)	Γ_0 (m^2/s)	ε (m^2/s^3)	ε*	T*
H=0.93B_s	78	0.30	1.54	0.81	0.94
H=1.50B_s	80	0.33	0.96	0.65	1.11
H=2.24B_s	78	0.37	0.64	0.49	1.37

Table 10 Parameters used for integrating the Sarpkaya's model

Table 10 also contains the vortex lifespan, defined in section [1.2.3]. This was calculated based on knowledge of the turbulence parameter according to the empirical

relations given by Sarpkaya. Since all the three turbulence parameter values verify the condition ε* > 0.2535, the vortex lifespan (T*) was calculated by:

$$T^* = \left(\frac{0.7454}{\varepsilon^*}\right)^{\frac{3}{4}} \tag{4.18}$$

Before integrating equation (4.14) it is necessary to distinguish two different cases: vortex in ground effect and vortex out of ground effect. In fact the differential equation (4.14) changes depending on the case studied as explained in section [1.2.3].

4.2.1 Wake vortex in ground effect

In ground effect ($z_G/b_0 \leq 1.5$) the circulation decay is assumed to be linear and is obtained integrating equation (1.42-a):

$$\Gamma(T) = \Gamma_0 \left[\left(-\frac{C}{T^*} e^{-\frac{C}{T^*}T_G}\right) T + 1\right] \tag{4.19}$$

Now if the time T_G that is the time the wake vortex enters into the ground effect region is our time zero then (4.19) becomes:

$$\Gamma(T) = \Gamma_0 \left[\left(-\frac{C}{T^*}\right) T + 1\right] \tag{4.20}$$

which is the equation we consider for our application within this study. Indeed, the wake vortex system is considered to be initialised ($T = 0$) at $x = 0.18B_s$ down-stream the wing where the vortices are well-shaped the roll-up is complete and the effect of the secondary vortices is negligible. At this stage the wake vortex has a height of about $1.57b_0$ which allow us to say with good approximation it is in ground effect.
The equation for the descent of the vortex system is then given by:

$$\frac{d^2 Z_v}{dT^2} + \frac{C}{T^*} = 0 \tag{4.21}$$

This equation has a close well known quadratic solution given by:

$$Z_v(T) = -\frac{C}{2T^*} T^2 + T \tag{4.22}$$

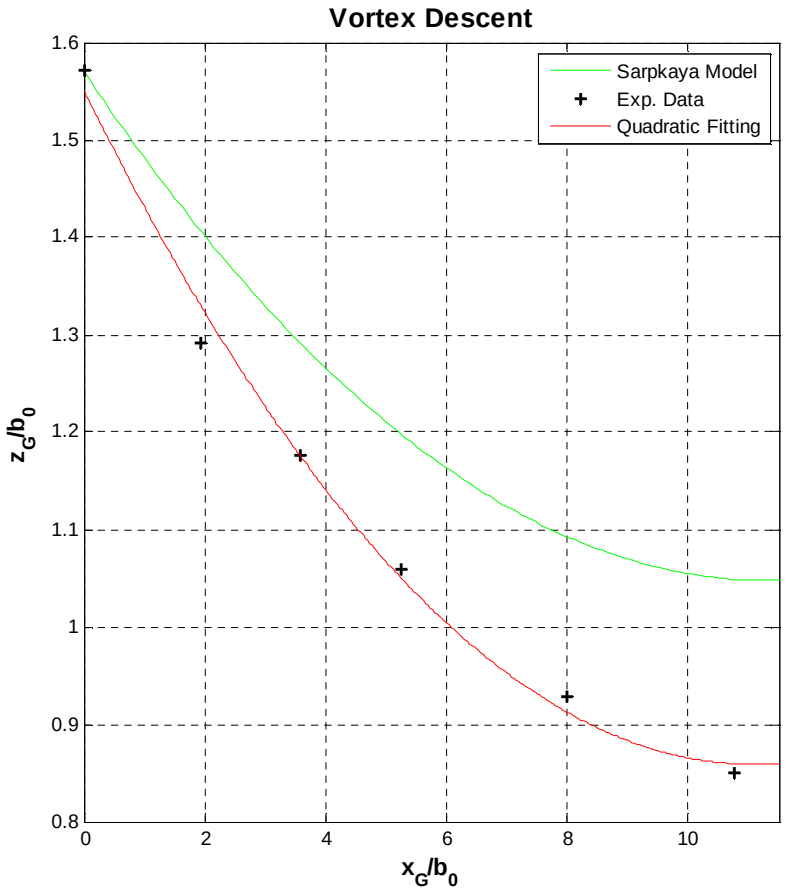

Figure 49 Vortex descent for wing height H=0.93B$_s$

Figure 49 shows the vortex descent predicted by the model the actual experimental results and quadratic fitting performed using a built in Matlab function. In the graph the descent is expressed as a function of the distance in the x direction but the model gives a time-dependent solution. Thus a reference velocity was used to convert the time-dependent solution given by the model into the space-dependent solution needed to compare with the experiments. The equipment used to carry out the experiments does not facilitate time-dependent data. The reference velocity used to convert the data, namely circulation and descent, was the velocity measured by a Pitot tube placed at the wing trailing edge height (u_{ref} = *6.63 m/s*). This choice seemed reasonable from a physical point of view. Unfortunately although the model predicts the trend of the descent, which is evidently parabolic (red line in Figure 49), it fails in predicting the vortex position. This partial failure might depend on the coefficient – *C/2T** in the descent equation (4.20) which depends on both, the constant C assumed to be *0.45* (Sarpkaya [42]) and the vortex lifespan (T*). Thus the way the turbulence

parameter was evaluated could be the real explanation of this partial failure in conjunction with the value assigned to C.

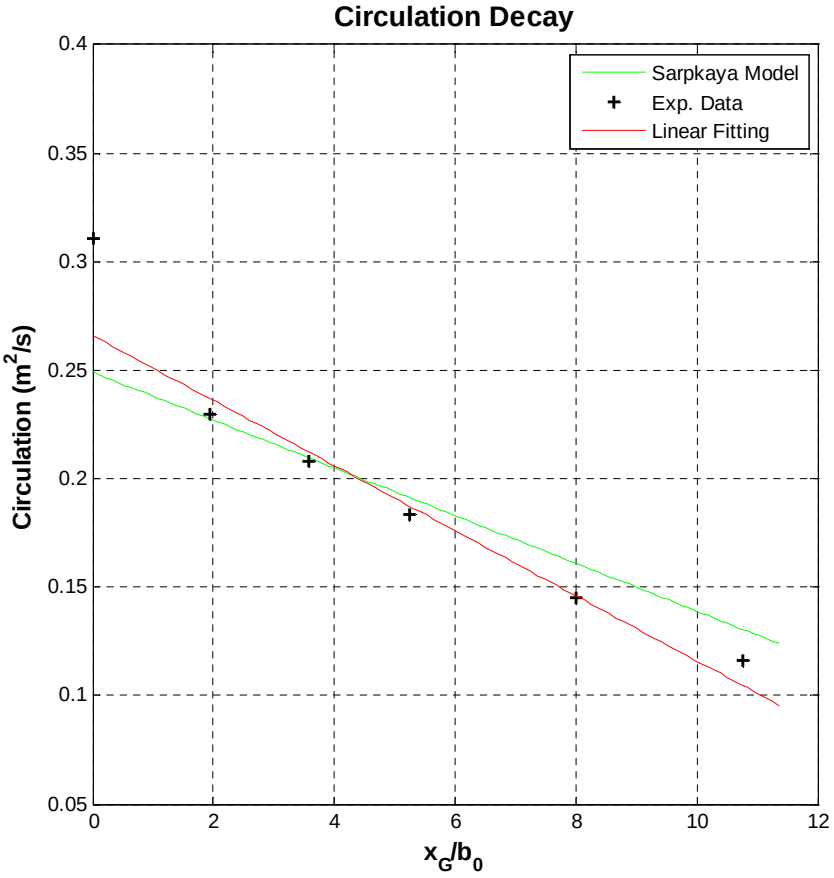

Figure 50 Circulation trend for wing height H=0.93B_s

The circulation decay appears to be better described by the model (Figure 50). The red line is a fitting to a straight line obtained using the method explained in [2.3.1.2] while the green line is the model prediction fitted to the data. The initial circulation that appears in the linear equation of the circulation was recalculated to fit the experimental data. The two fittings are very close to each other demonstrating the circulation is well described by the model.

4.2.2 Wake vortex out of ground effect

When the wake vortices are out of ground effect their vertical displacement is described by equation (4.14) and their circulation decay by equation (1.40). The results related to the wing height $H=1.50B_s$ are presented in this section.

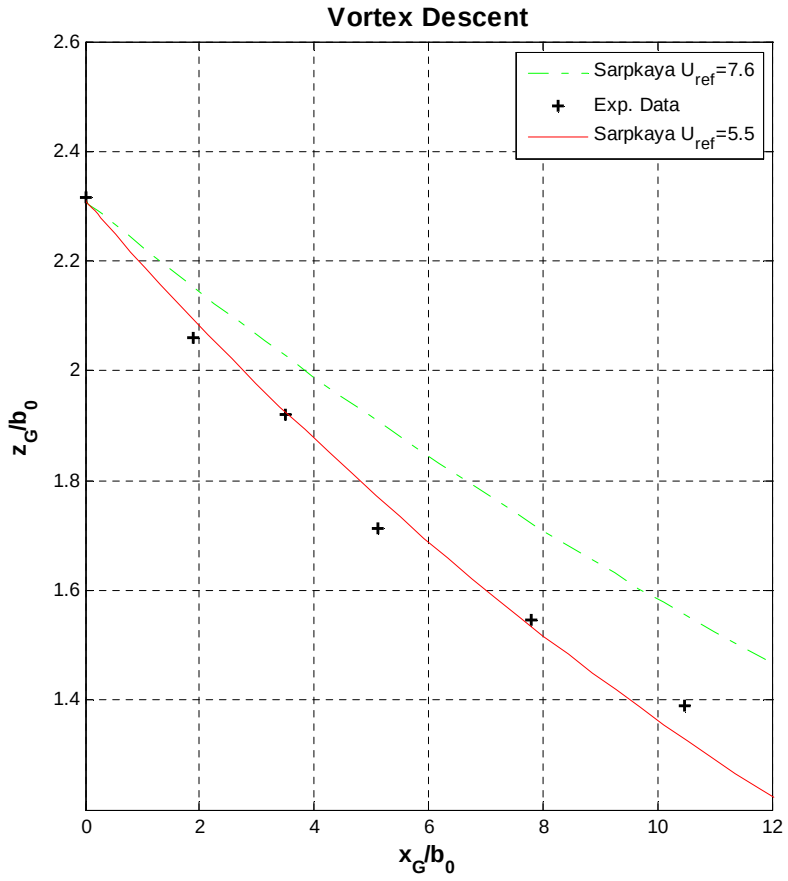

Figure 51 Vortex descent at wing height H=1.50B$_s$

In this case the model was first tried with a reference velocity for time/space conversion equal to the velocity measured by a Pitot-static tube at the same height as the wing trailing edge (u_{ref}=*7.6 m/s*). An effort was then made to improve the fit both of the descent and the circulation to the experimental data, and a velocity of *5.5 m/s* was finally chosen. It is interesting to see from Figure 51 and Figure 52 the improvement of the fit to the experimental data using this new reference velocity (red line in both graphs). However it should be noted that although the overall trend of the descent is well represented by the model the circulation is not so good. In fact Figure 52 shows that the actual trend of the circulation is linear and not exponential (the purple line that fits the data to a straight line). The pale blue line instead fits the data to an exponential function of the form predicted by the model.

In conclusion from analysing the data against the model presented here it is not possible to determine its absolute validity for this kind of experiment. More data and

better knowledge of the turbulence characteristics in the wind tunnel are required to draw stronger conclusions. Also significant is the problem connected to the choice of the reference speed which, as observed, strongly affects the comparison between space-dependent evaluations of the flow and time-dependent model solution. This velocity must be matched to the flow characteristics, representing a kind of characteristic parameter for the flow. This aspect requires much deeper investigations.

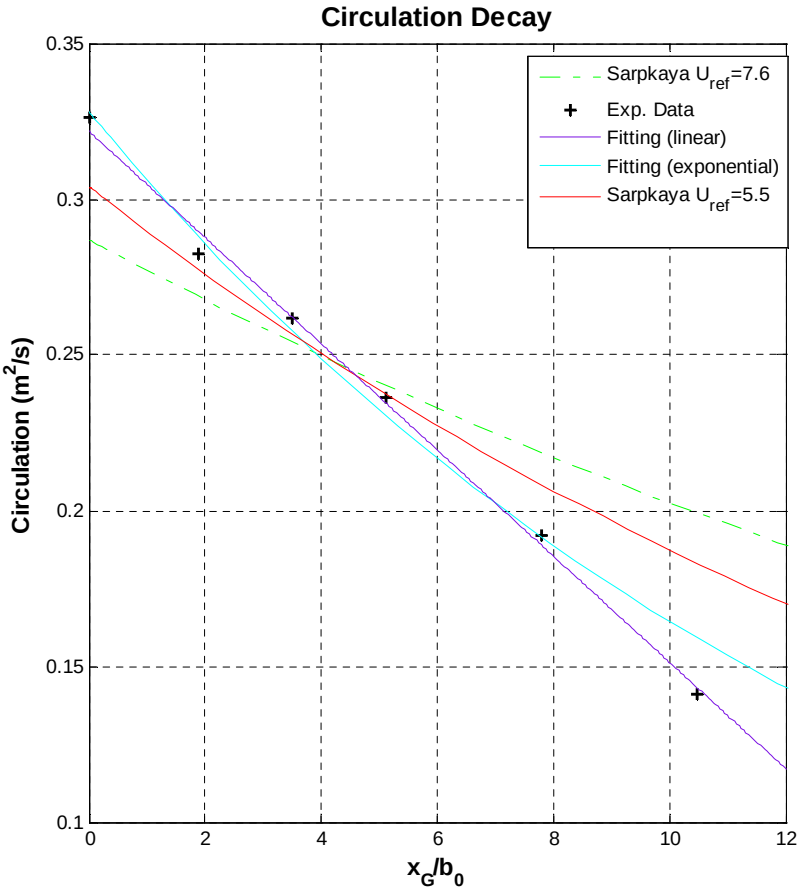

Figure 52 Circulation decay at wing height H=1.50B_s. Comparison with model, fitting and experimental results

4.3 Further comparisons

Barker [4] shows the trajectory of a vortex pair in proximity of the ground within a water tank. The vortices were initialised with a separation of *150 mm* and a circulation of $0.075 m^2/s$. It is clear that these flow conditions are very different from those experienced in an ABLWT where turbulence is strong and inhomogeneous but due to absence of more similar experiments freely available in the literature, it is considered interesting to analyse the results obtained. In the same article the experiments results are compared to the solution given by Lamb [29] for a pair of straight line vortices interacting with an image pair (*four vortex model*) (Figure 53). Referring to Figure 53 the trajectory of the top right vortex is obtained using the superimposition principle and it is expressed by:

$$Z_G = \frac{Y_G}{\sqrt{\left[\left(\frac{1}{H_0}\right)^2 + 4\right] Y_G^2 - 1}} \tag{4.23}$$

where all the variables are in non-dimensional form. This equation is obtained from a re-elaboration of the solution given by Lamb [29].

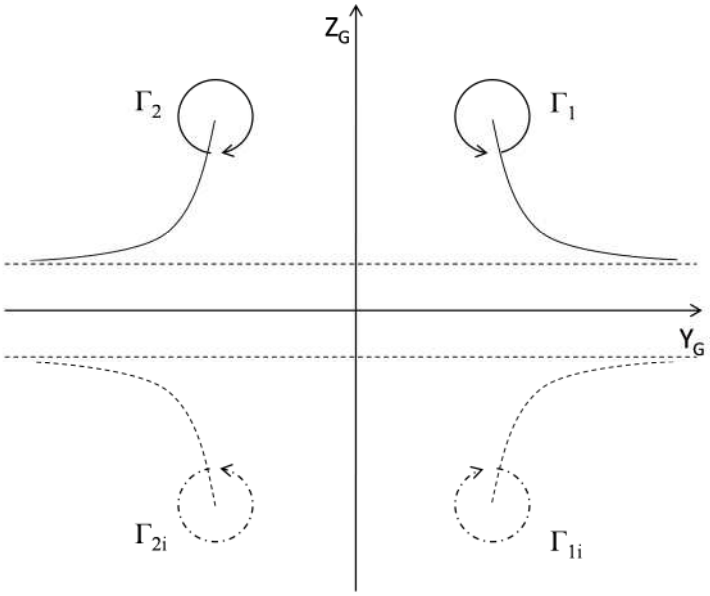

Figure 53 Sketch of the four point vortex system

Figure 54 shows a comparison between the experimental data taken from [4], the data collected in ABLWT within this study, the *vortex sheet model* presented in section [4.1] and the *four vortex model* just discussed.

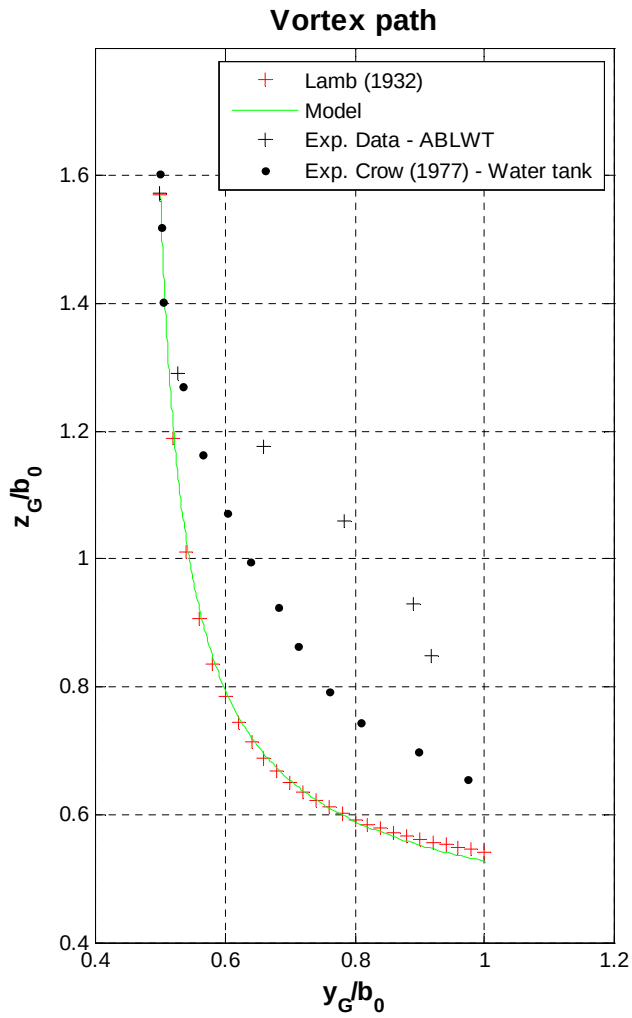

Figure 54 Comparison between the four vortex model, the experimental data obtained by Barker [4], the experimental data obtained in the ABLWT and the vortex sheet model presented in section [4.1]

It is interesting to notice that the *four vortex model* solution coincides with the *vortex sheet* solution given previously. This is actually expectable because the image pair in the Lamb's model is placed to nullify the velocity component along z (w) at the ground, just like the vortex sheet, since no particles can physically cross the ground. So, the only difference between the two models is the distribution of circulation placed to verify the boundary condition. In one case (*Lamb's model*) all the circulation is concentrated in a pair of counter rotating vortices (image pair) in the other case (*vortex sheet model*) the

circulation is distributed over the ground with a function of time. Since the problem is governed by the Laplace equation and the boundary condition on the ground is the same in both the models the results have to be the same as shown in Figure 54. Therefore, these models are two different ways of solving the same problem. Of course they are built in different ways and involve (as shown) different mathematics but at the end they are just two different images of the same problem which admits just one unique solution. However Figure 54 also shows there is a slight difference between the two solutions, but this depends on the numerical approach used to solve the system (4.11). In fact the reader has to bear in mind that the *Lamb's model* was solved analytically whereas the *vortex sheet model* was solved numerically and in the numerical solution lies the error.

Furthermore both models fail in predicting the vortex trajectory for the two sets of data here presented. And the two sets of data themselves show different trends which might be due to the initial flow condition (grade of turbulence) which eventually affect the space evolution of the flow. Also the difference might be due to a different definition of vortex centre (which in our case was defined as the centroid of circulation).

5 SPIV Results

The mean flow field was analysed in Chapter 3. The vortex time-average position was tracked making it possible to establish the trajectory of one vortex (left side) assuming symmetry with respect to the centreline. The vortex was seen to diverge and decay quickly and eventually to lose coherence over the farther planes investigated. In this chapter the real nature, fluctuating and intermittent, of the flow is analysed, using the SPIV data collected. The present chapter is divided in two main sub-sections. The first section will give a qualitative analysis of the fluctuating flow field against the time-average flow field. In the last part, a quantitative study of the turbulent field will be given, by showing the turbulence statistics throughout the complex vortex flow field and analysing the energy dissipation within the vortices.

5.1 Fluctuating flow Vs average flow

Particle Image Velocimetry makes it possible to evaluate the instantaneous flow field. For steady laminar flows, evaluations of the instantaneous flow field are all equal to each other and equal to the time averaged flow. On the contrary turbulence means that every evaluation of the flow field is different from another and as a consequence different from the mean flow. Also due to the random nature of the phenomenon each realization of the flow will eventually differ from the others. A statistical description of the flow is then required. Assuming an experiment can be repeated many times, keeping as much as possible identical, the initial conditions, ensemble averages of the flow variables can be introduced depending on the position and time in the flow development. However if the flow is statistically steady, which means that its statistical quantities do not change with time, and is not possible to reproduce many times the experiment, then the ensemble averages can be replaced with the time averages defined by Formula (1.14) (Casciola [7]). If the evaluation time (T_e) is much greater than the correlation time of the flow, then we can consider different realizations of the flow field within the same run of the experiment. Since the wake vortex flow can be assumed to be a three-dimensional statistically steady flow, all the averages within the present chapter were calculated using the time average, Formula (1.14)

The stochastic and fluctuating nature of the flow is shown in Table 11 below.

	Velocity Vector Plot	***Vorticity***
n°15	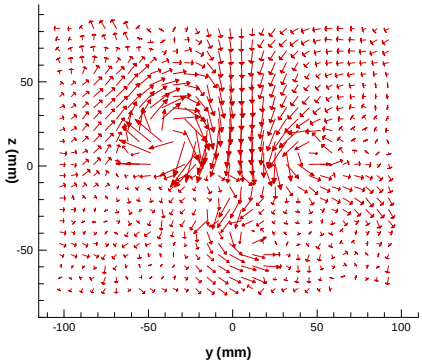	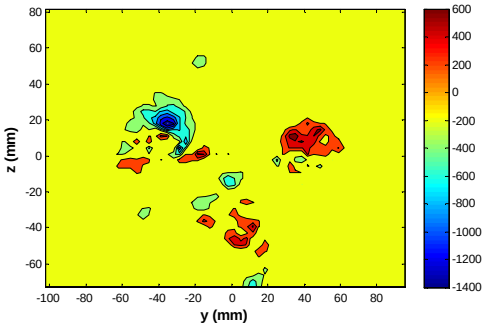
n°20	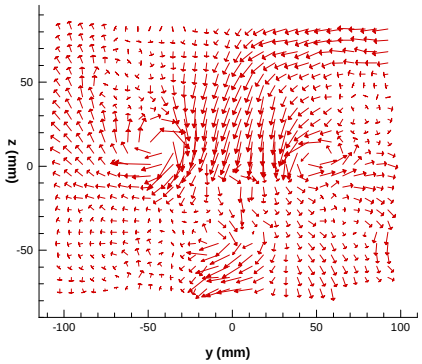	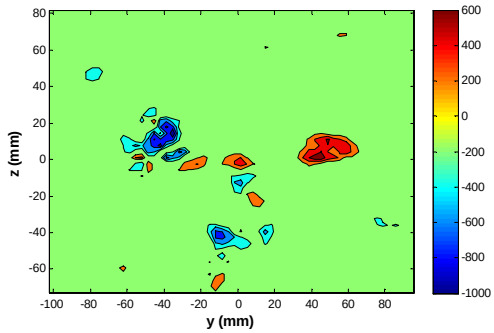
n°25	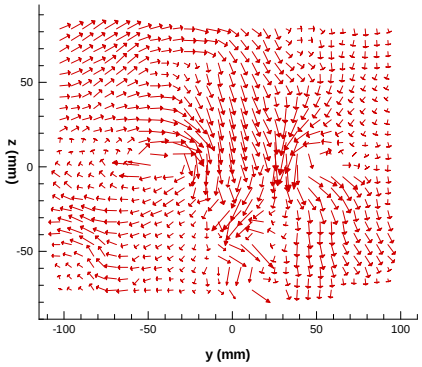	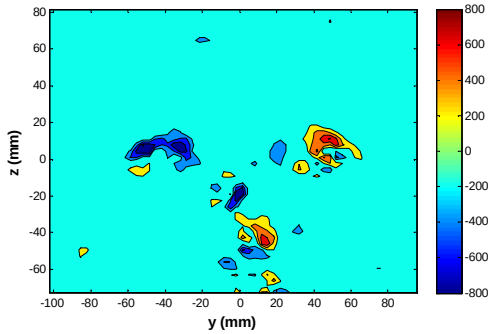
n°30	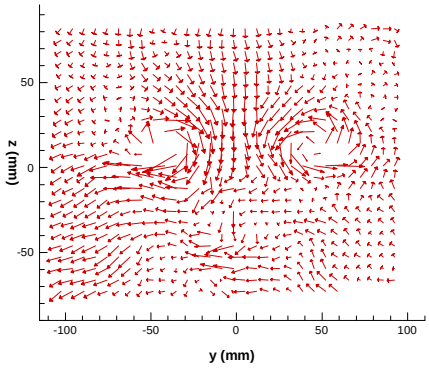	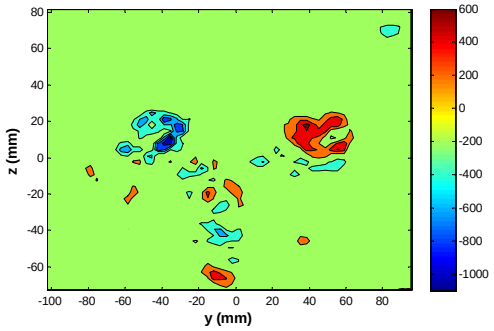

n°35	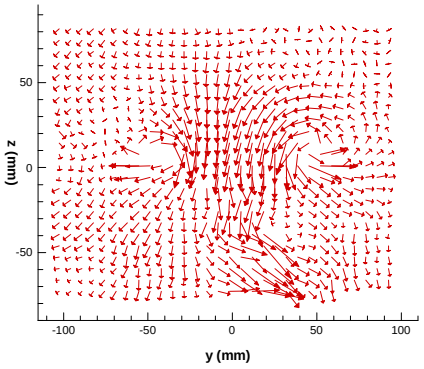	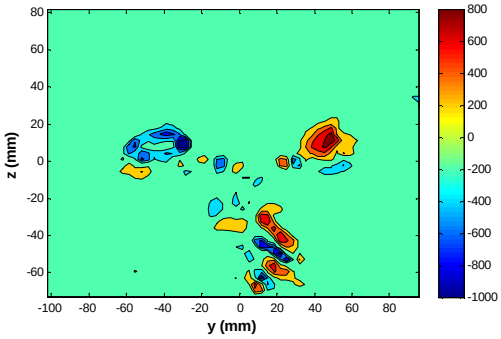
n°40	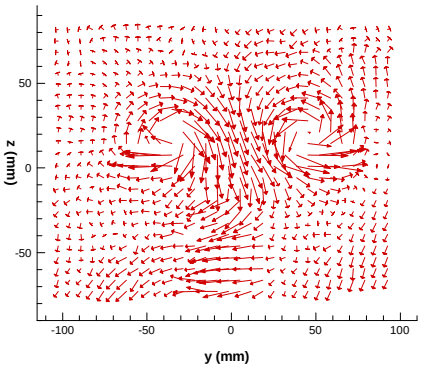	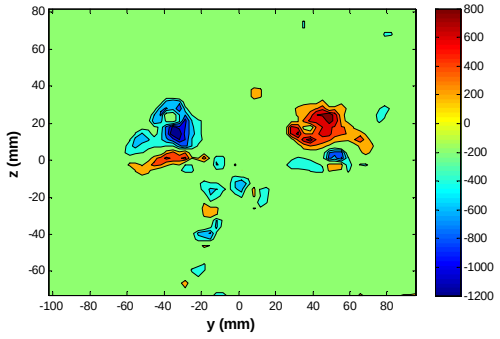
n°45	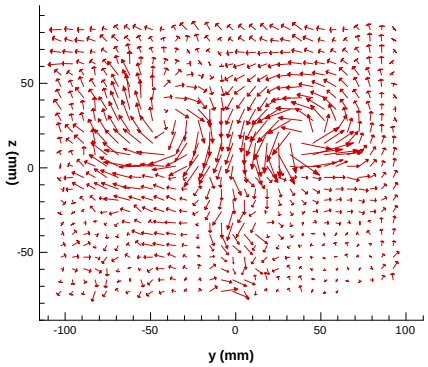	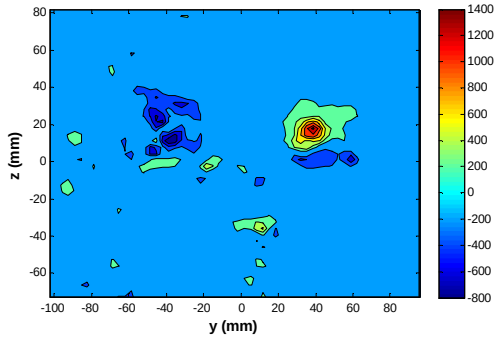

Table 11 Time evolution of the velocity field (left) and vorticity field (right) due to the turbulence fluctuations

In the first column of Table 11 instantaneous field evaluation number is found. It is useful to remind that within this study *50 pairs* of particle images were taken for each run with a time interval of about *0.14 s* between each pair, which means that *50 evaluations* of the flow field were available for analysis. Looking at the data two aspects of the instantaneous field have to be stressed. First, the vortices undergo to a continuous deformation and motion with time. Eventually they lose coherence as shown by the vorticity maps. In most of the plots instead of a single high peak of vorticity it is possible to identify multiple peaks of vorticity for each side of the flow. Both vortices appear to have a dynamic structure that breaks and reform in time due to the intense

fluctuations. Second, the flow loses its symmetry and again this is explained by the randomness of the turbulence fluctuations. The flow eventually becomes strongly asymmetric and the vortices differ from each other in both dimension and intensity (circulation). The total circulation behind the wing should be nominally zero if the flow was exactly symmetric with respect to the centreline. This circulation fluctuates and eventually can reach relatively high peaks (Figure 55) with respect the average value (*~0.02 m^2/s*) obtained for the mean flow.

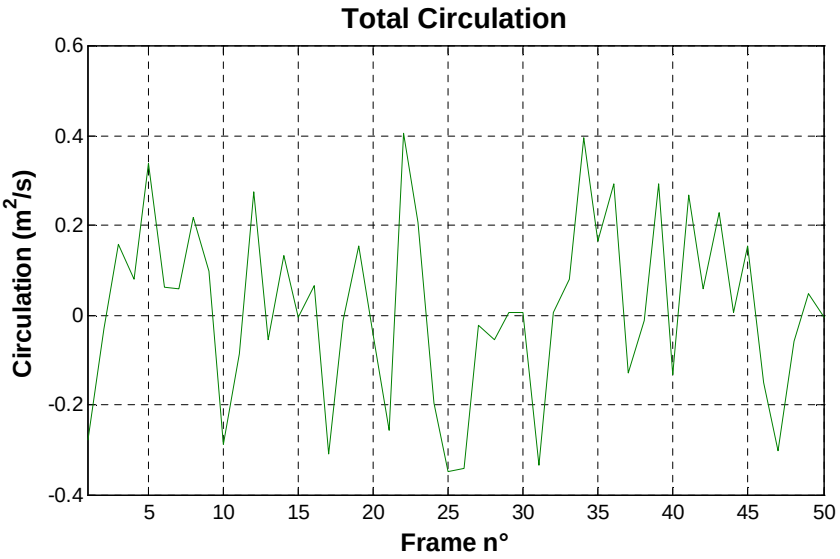

Figure 55 Total circulation Vs time at wing height H=1.50B_s, over the plane located at x=0.18B_s

Finally, the last aspect to be stressed is that the elongated region of relatively high mixed vorticity present in each vorticity plot of Table 11 beneath the vortices is most likely due to the support bar used to fix the wing model in the wind tunnel working section.

Since the flow is statistically steady the mean field does not change in time. Thus averaging in time the instantaneous fields the time-average field is obtained (Figure 56).

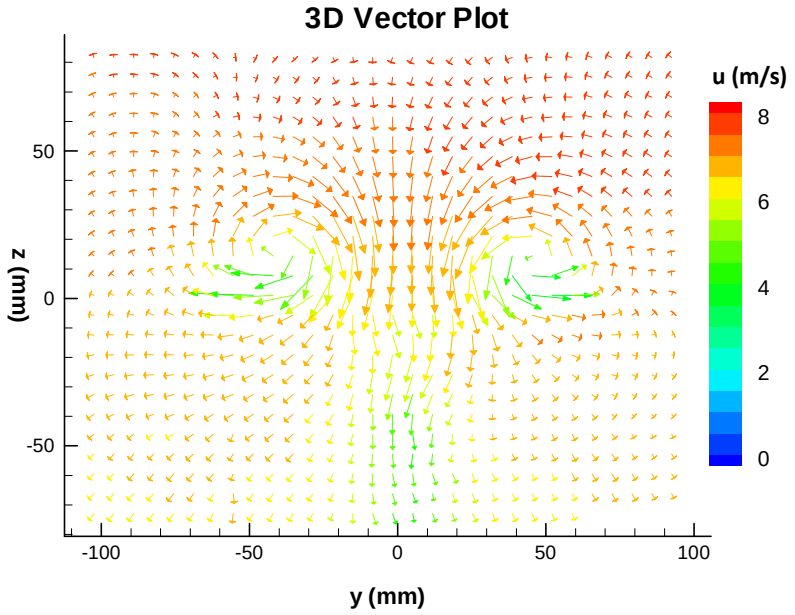

Figure 56 3D velocity vector plot for wing height H=1.50B_s at x=0.18B_s

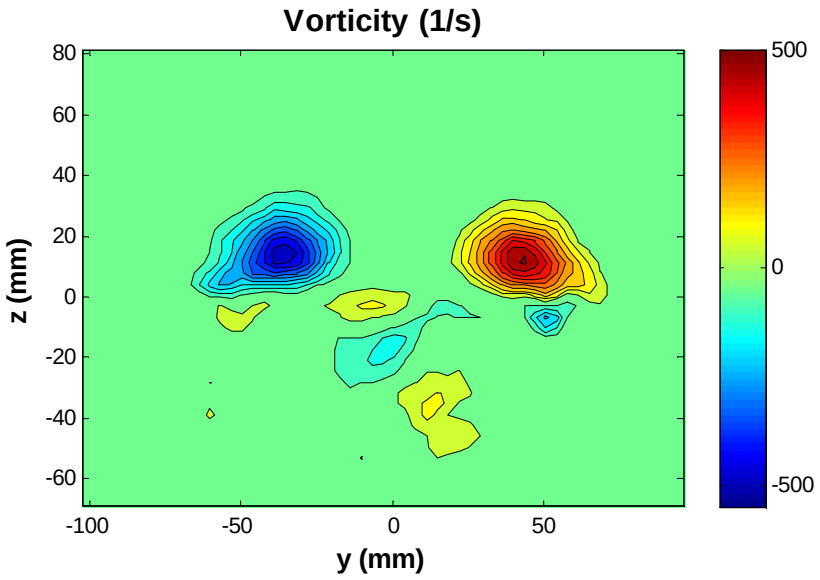

Figure 57 Vorticity map for wing height H=1.50B_s at x=0.18B_s

The velocity field was averaged over a period of about $T_e = 6.8\ s$ with an estimated time step (Δt) of *0.14 s*. As expected the average flow field regains symmetry with respect the centreline. The remnant asymmetry might be due to a slight misalignment of the wing that was fixed manually within the wind tunnel, with respect to the freestream, or might depend on an axial asymmetry in the flow itself at the inlet of the wind tunnel

working section or a combination of these factors. A region of relatively low mixed vorticity beneath the vortices corresponding to the support bar is still present in the average flow, but it will soon dissipate.

5.2 Turbulence Statistics

This section illustrates the turbulent field from a quantitative point of view and eventually the mechanism of energy dissipation the vortices undergo due to turbulence action. After a discussion on the turbulence field in the last part of the present section the Boussinesq hypothesis will be introduced and investigated against this particular flow field. Most of the results presented here refer to the closest plane to wing ($x=0.18B_s$). This is because at this stage the vortex system is well defined in terms of circulation and concentrated in small a region, thus all the flow properties are well defined and easily recognised. In contrast the plane located at $x=3.74B_s$ shows the vortex flow losing its coherence and appearing to be spread over a large region of space, being difficult to be clearly recognised.

5.2.1 Turbulence intensity

The three components of the turbulence intensity namely I_u, I_v and I_w that represent the intensity of the turbulent fluctuations with respect the mean flow velocity were calculated by means of Formula (1.16). As we know the vortex system is initialised in a highly turbulent ambient. At the wing height $H=1.50B_s$, which we refer within this section, the ambient turbulence is about *13%* and this contributes as previously analysed to speed up the vortex decay and eventually breakdown. However this turbulence level is subject to increase in the wake due to the high shear stresses within the vortex flow. It also depends on the Reynolds number. Therefore the turbulence field in the wake vortex within the ABL can be seen as made up of two components: ambient turbulence and vortex self-induced turbulence. Obviously the problem is highly non-linear so it is not possible practically to evaluate separately these two components. This is just a simple method to model this complex problem justified by the experimental observations.

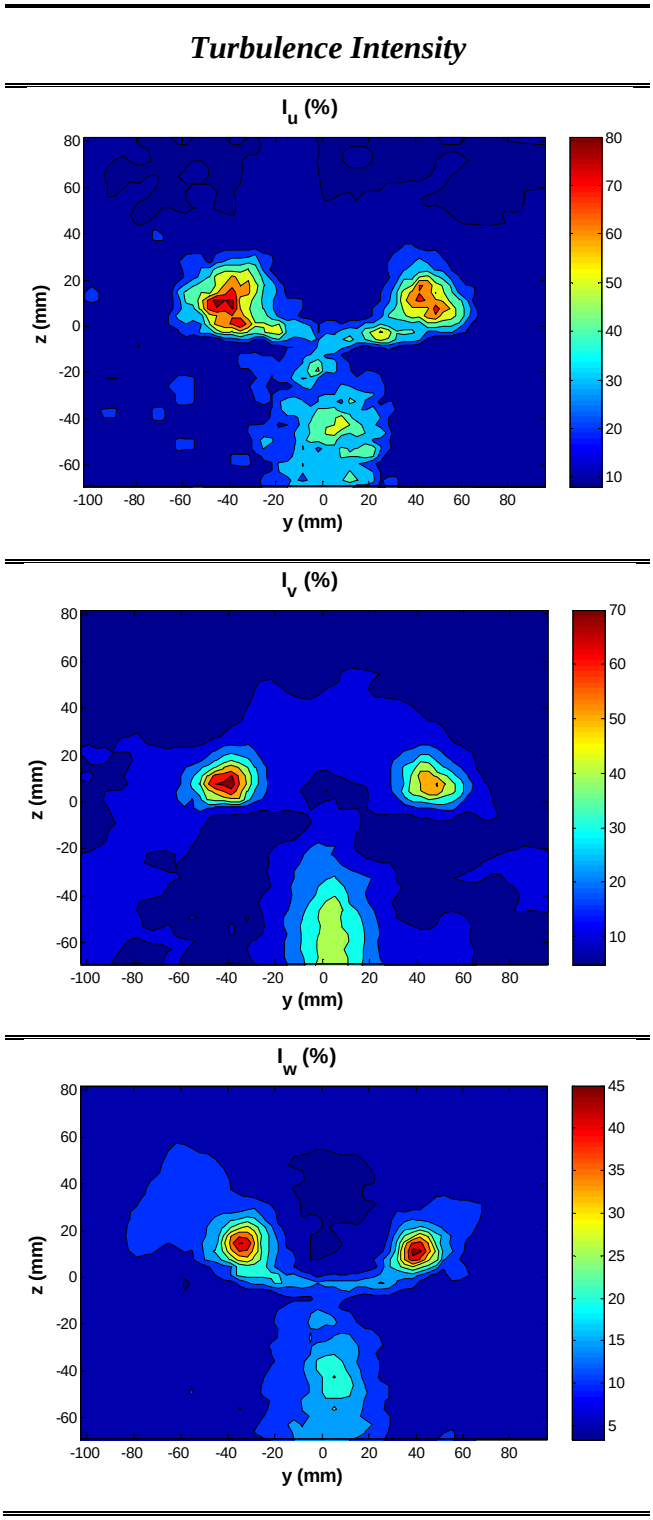

Table 12 Turbulence intensity: x component (top), y component (middle) and z component (bottom)

As is clear from Table 12 the turbulence field is not homogeneous in any of the three directions (x, y and z). The three components of the turbulence intensity show similar behavior: all the turbulence components reach their peaks in the vortex cores.

Also these peaks are very intense: turbulence in the x direction (out-of-plane) reaches *80%* whereas in the y and z directions respectively, *70%* and *45%*.In contrast, in the outer regions of the vortex system the turbulence tends to the ambient turbulence. This phenomenon can be analysed using the generic equation for the evolution of turbulent kinetic energy (k) given by (Bernard [5]):

$$\frac{\partial k}{\partial t} + \overline{u_j}\frac{\partial k}{\partial x_j} = -\frac{1}{\rho}\frac{\partial \overline{p'u'_\iota}}{\partial x_i} + \frac{\partial}{\partial x_j}\overline{u'_\iota\left[\nu\left(\frac{\partial u'_\iota}{\partial x_j} + \frac{\partial u'_J}{\partial x_\iota}\right)\right]} - \frac{\partial}{\partial x_i}\overline{\left(u'_\iota\frac{u'^2_J}{2}\right)} - \overline{u'_\iota u'_J}\frac{\partial \overline{u_\iota}}{\partial x_j} - \frac{1}{2}\nu\overline{\left(\frac{\partial u'_\iota}{\partial x_j} + \frac{\partial u'_J}{\partial x_\iota}\right)\left(\frac{\partial u'_\iota}{\partial x_j} + \frac{\partial u'_J}{\partial x_\iota}\right)} \quad (5.1)$$

The penultimate term expresses the production of turbulent kinetic energy (k). It represents the amount of energy subtracted to the mean flow. Thus it is the source of the turbulence. It depends on the Reynolds stresses and on the mean velocity gradients, namely $\partial\overline{u_\iota}/\partial x_j$ where $\overline{u_\iota}$ is the ith mean velocity component. The core of a vortex is characterised by a high mean velocity gradient and high viscous stresses as previously analysed. Its outer region can be considered quasi-inviscid since the velocity gradients are lower and the viscous effect less significant. At this point it is clear that the vortex core acts as a source of turbulent kinetic energy, so the highest turbulence intensity is found in this region. It is clear as well that in the outer region of the wake vortices the turbulence intensity tends to the ambient turbulent since the velocity gradients relative to the vortex flow decrease with distance from the vortex centres. It is then clear that the trend of the turbulent kinetic energy in the flow field must be similar to that of the turbulence intensities (Table 13).

Finally the energy subtracted from the mean flow in favour of the turbulence fluctuations is dissipated by viscosity effects at the smallest scales of turbulence. The energy dissipation is given by the last term in equation (5.1) that was already introduced in section [1.2] with the name of turbulence dissipation rate (ε). Since the flow is statistically steady the statistical quantities do not change with time so they are fixed over each slice of the wake. However as we get farther from the wing trailing edge we find the wake less and less energetic until it eventually dissolves tending to the upstream flow condition. As the mean flow loses energy due to conversion into heat the

amount of energy transferred to the turbulent field (production of TKE) reduces as well. As consequence the vortex self-induced turbulence (dependent on the vortex flow itself) will tend to end. Thus the flow will tend to the upstream condition. This concept is well explained by the TKE plot over the plane located at $x=0.18B_s$ compared to that over the plane located at $x=3.74B_s$ (Table 13).

TKE
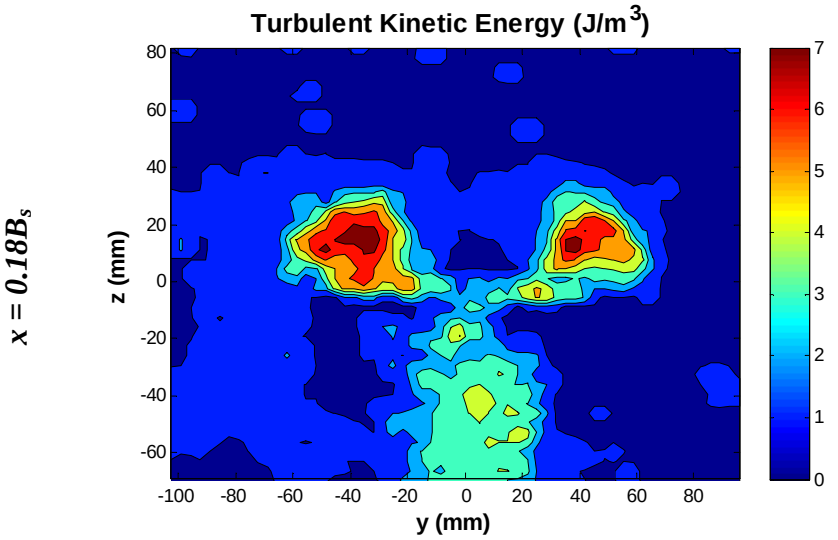
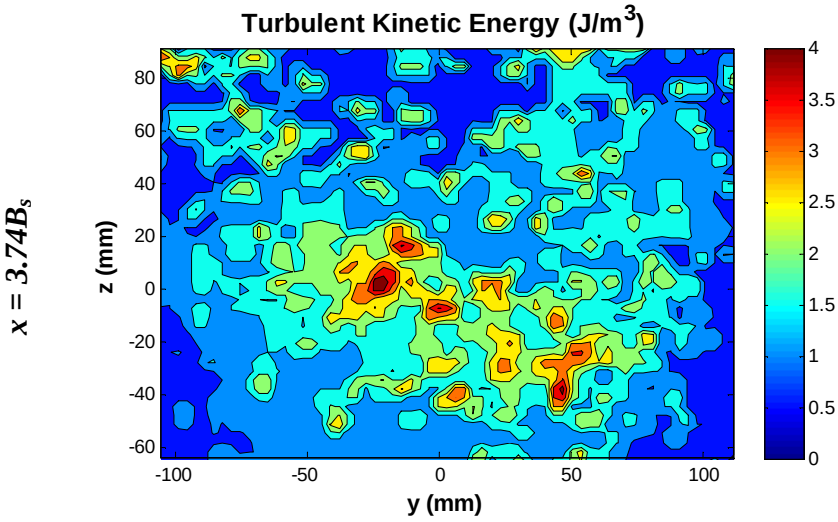

Table 13 Turbulent kinetic energy over two planes

As evident the peak of TKE over the farther plane is almost half of that over the first plane. Also it appears that the flow field (turbulent field) is not as coherent as the flow field in the region closer to the wing and this is due to the quick dissipation the vortex

system undergoes. Refer to Appendix B.1 for the turbulence intensity along the three main directions over the second plane ($x=3.74B_s$).

5.2.2 Velocity correlations and correlation lengths

In section [1.2.1] the concept of velocity correlation two point one time was introduced. By means of Formula (1.18) six main velocity correlations were calculated and non-diemensionalised using the correspondent component of the Reynolds stress tensor. Those are given below:

Correlation along y:

$$\rho^{[2]}{}_{11}(\boldsymbol{x},\boldsymbol{x}',t)=\frac{\overline{u'(\boldsymbol{x},t)u'(\boldsymbol{x}+r_2,t)}}{R^T{}_{11}(\boldsymbol{x},t)} \tag{5.2-a}$$

$$\rho^{[2]}{}_{22}(\boldsymbol{x},\boldsymbol{x}',t)=\frac{\overline{v'(\boldsymbol{x},t)v'(\boldsymbol{x}+r_2,t)}}{R^T{}_{22}(\boldsymbol{x},t)} \tag{5.2-b}$$

$$\rho^{[2]}{}_{33}(\boldsymbol{x},\boldsymbol{x}',t)=\frac{\overline{w'(\boldsymbol{x},t)w'(\boldsymbol{x}+r_2,t)}}{R^T{}_{33}(\boldsymbol{x},t)} \tag{5.2-c}$$

Correlation along z:

$$\rho^{[3]}{}_{11}(\boldsymbol{x},\boldsymbol{x}',t)=\frac{\overline{u'(\boldsymbol{x},t)u'(\boldsymbol{x}+r_3,t)}}{R^T{}_{11}(\boldsymbol{x},t)} \tag{5.3-a}$$

$$\rho^{[3]}{}_{22}(\boldsymbol{x},\boldsymbol{x}',t)=\frac{\overline{v'(\boldsymbol{x},t)v'(\boldsymbol{x}+r_3,t)}}{R^T{}_{22}(\boldsymbol{x},t)} \tag{5.3-b}$$

$$\rho^{[3]}{}_{33}(\boldsymbol{x},\boldsymbol{x}',t)=\frac{\overline{w'(\boldsymbol{x},t)w'(\boldsymbol{x}+r_3,t)}}{R^T{}_{33}(\boldsymbol{x},t)} \tag{5.3-c}$$

r_2 and r_3 stand respectively for a displacement along y and along z with respect the initial point $\boldsymbol{x}$. Again the apex above the non-dimensional correlation symbol (ρ) states the direction in which the correlation is calculated. Those calculations were performed within Matlab for each grid point identified by the coordinates $\boldsymbol{x}=(x,y,z)$. Thus for each grid point the trend of the six evaluated correlations was available. In Table 14 a comparison between the longitudinal correlations along y and along z, namely $\rho^{[2]}{}_{22}$ and $\rho^{[3]}{}_{33}$ for two points are shown. The two points considered are respectively into the

vortex core region of the left side vortex and the other just above the vortex in the outer region of the vortex itself.

	Inner Region	***Outer Region***
$\rho^{[2]}_{22}$	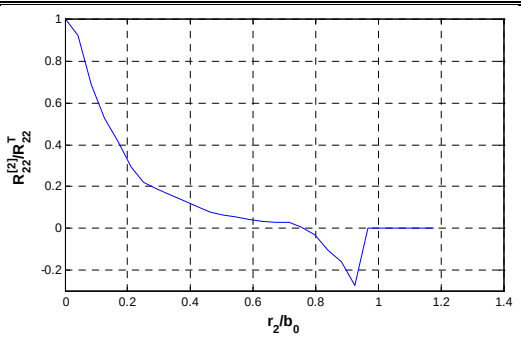	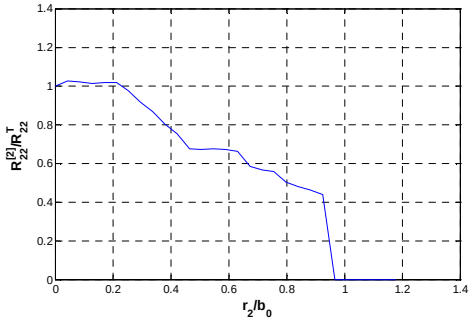
$\rho^{[3]}_{33}$	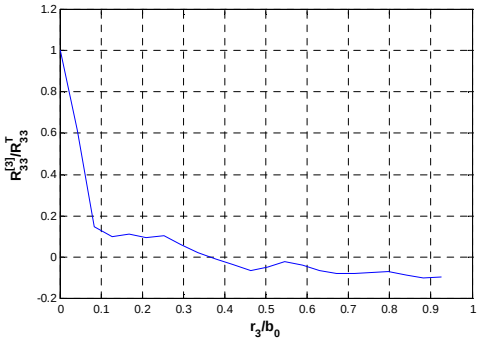	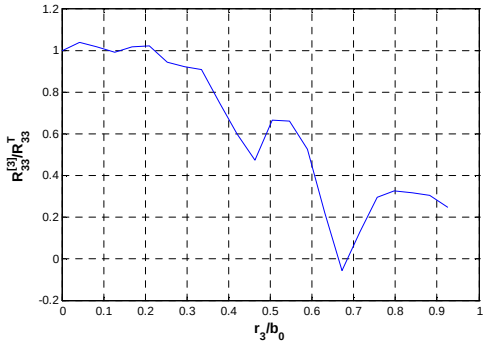

Table 14 Longitudinal spatial velocity correlation for two points

All the correlations show, as expected, a globally decreasing trend with the radial distance. However the velocity fluctuations tend to de-correlate faster in the inner region of the vortex with respect the outer region. The de-correlation is much faster in all the directions. This was confirmed analysing the correlations in other points of the domain. Having knowledge of the velocity correlations point by point it was possible to evaluate in each point of the domain the correlation lengths from Formula (1.21). The six correlation lengths were plotted into maps as fractions of the vortex separation assumed b_0=*80 mm*. Figure 58 and Figure 59 show the longitudinal correlation lengths all over the flow domain measured.

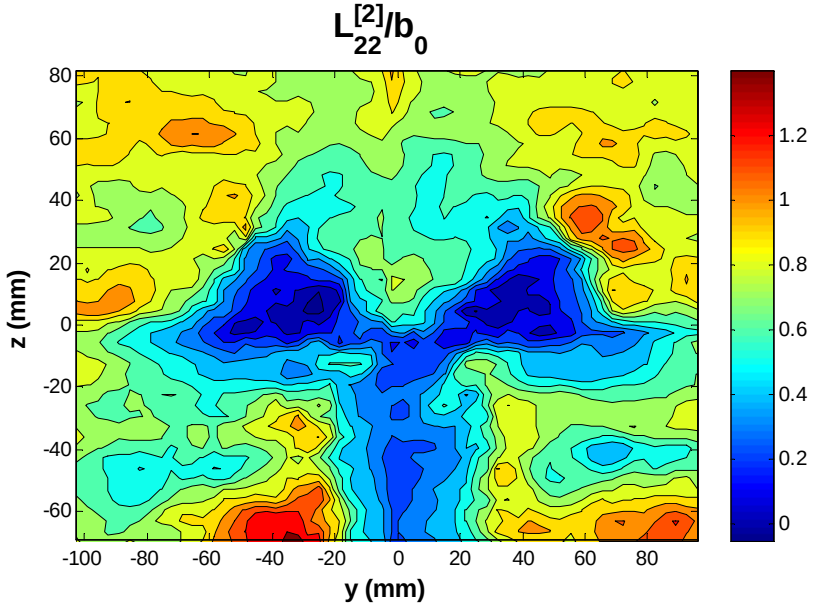

Figure 58 Longitudinal correlation length along y

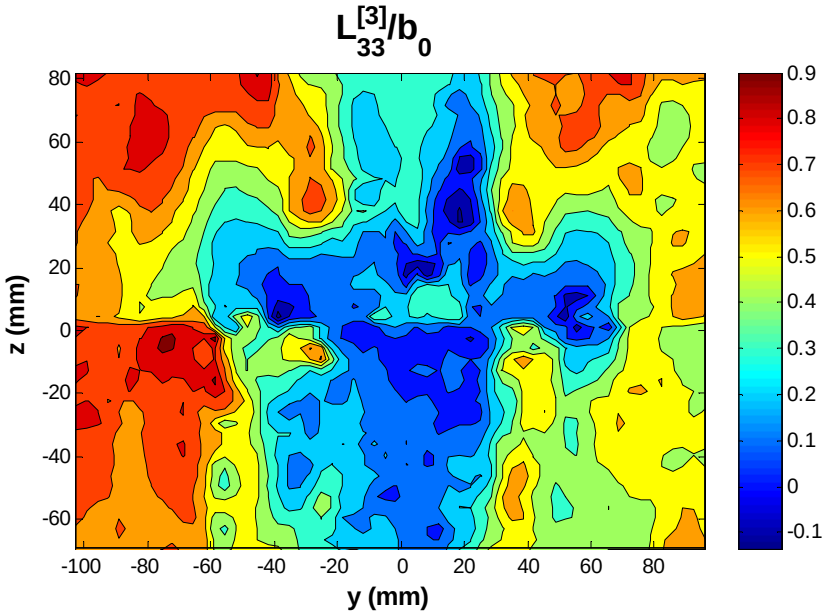

Figure 59 Longitudinal correlation length along z

In agreement with the trend of the velocity correlations along the two main directions y and z both correlation lengths reach their minimum values in the region of the wake vortices and of the wing support bar. This is especially evident in Figure 58 where the blue region recalls the shape of the mean vorticity distribution. Therefore where the production and dissipation of turbulent kinetic energy is maximum, in the vortex cores the turbulence tends to de-correlate faster. If the correlation lengths are

measures of the largest scales of turbulent flows then it means the energy extracted from the mean flow goes quickly at smaller scales in the inner region of the vortices respect to the outer region of the flow where larger scales form. The lateral correlation length which present many similarities with those analysed here, are available for comparison in Appendix B.2.

5.2.3 Turbulent viscosity as a possible second order tensor

The last aspect it is intended to discuss regarding the turbulence field into the wake vortices is the turbulent viscosity (ν_T). This concept was introduced by Boussinesq for the first time in 1877. According to the hypothesis, all the dissipative effects of the turbulence can be taken into account by a single scalar variable that he called turbulent viscosity. This scalar property of the flow would add to the kinematic viscosity characteristic of the fluid resulting in an effective viscosity that accounts for both the dissipative effects due to the viscosity and the dissipative effects due to turbulence. Since the energy dissipation in the mean flow due to turbulence depends on the Reynolds stress tensor (R^T_{ij}) the mathematical formulation of the hypothesis is given by (Pope [37]):

$$A_{ij} = \rho R_{ij}^T - \frac{2}{3}\rho k \delta_{ij} = -2\rho \nu_T \bar{S}_{ij} \tag{5.4}$$

where $\bar{S}_{ij}$ is the mean rate of strain tensor given by:

$$\bar{S}_{ij} = \frac{1}{2}\left(\frac{\partial \overline{u_\iota}}{\partial x_j} + \frac{\partial \overline{u_\jmath}}{\partial x_i}\right) \tag{5.5}$$

and k is the turbulent kinetic energy per unit of mass. Expressing the turbulence quantities, namely the Reynolds stresses as function of the mean rate of strain, the equation of motion of the mean flow can be closed and solved. A number of computational models for solving turbulent flows are based on this hypothesis, (k-ε, k-ω and so on...). However, even though the hypothesis models the turbulence as dissipative agent and surely has a strong physical meaning, even in simple turbulent flows it fails. In fact defining ν_T as a scalar parallelism between the deviatoric Reynolds stress tensor (A_{ij}) and the mean rate of strain tensor ($\bar{S}_{ij}$) is assumed, but unfortunately this is not the

case in most of the flows. Within this study three out six independent components of the rate of strain tensor were calculated namely $\bar{S}_{22}$, $\bar{S}_{33}$ and $\bar{S}_{23}$, and compared to the correspondent components of the deviatoric Reynolds stress tensor (Table 15). From a qualitative point of view the plots should have strong resemblance and it should theoretically be possible to superimpose component by component the plots being A_{ij} just scaled with respect $\bar{S}_{ij}$ by the turbulent viscosity ν_T.

$\bar{S}_{ij}$	A_{ij}
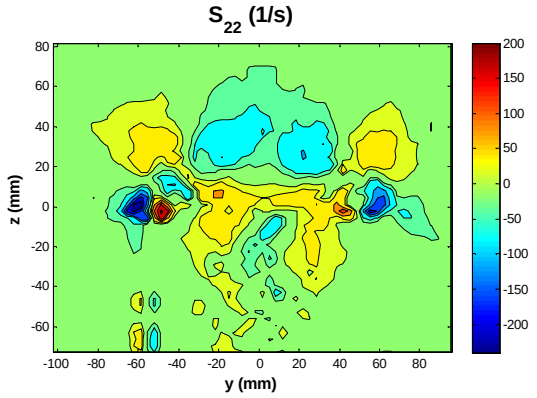	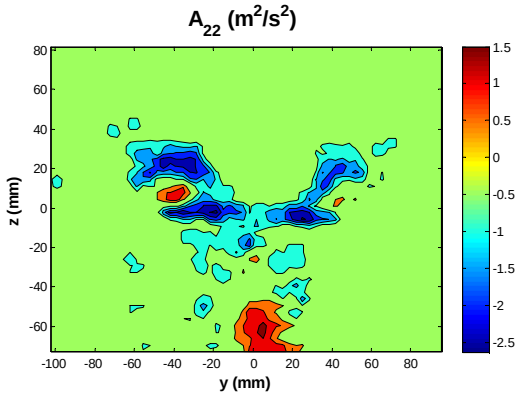
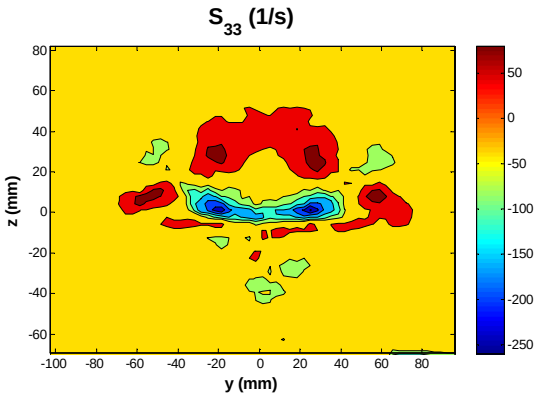	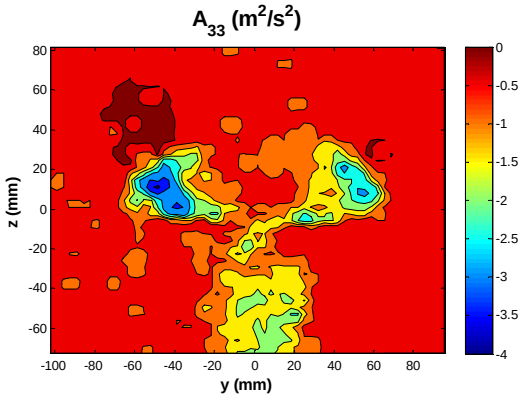
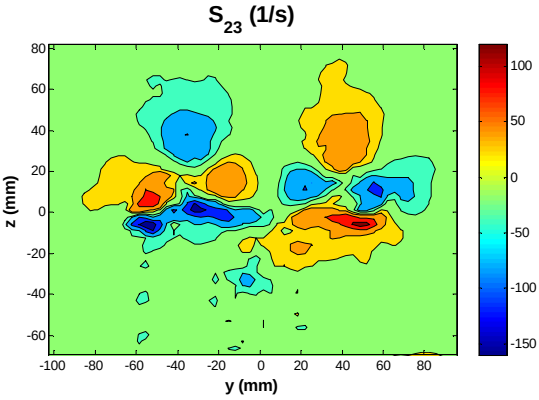	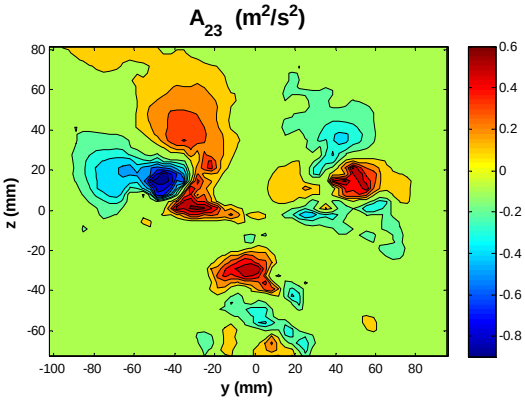

Table 15 Rate of strain (left) Vs deviatoric Reynolds stress (right)

As expected, no resemblances are between the tensors components. The best similarities are obtained for the lateral components $\bar{S}_{23}$ - A_{23}. However the ratio component by component of the two tensors should return the turbulent viscosity proposed by Boussinesq, as follow:

$$\nu_T = -\frac{A_{ij}}{2\bar{S}_{ij}} \tag{5.6}$$

and this value should be equal along each component being by hypothesis a scalar. Three plots for the turbulent viscosity were obtained but unfortunately they are all different from each other. Due to the difficulties in reading those plots they are not reported here. This led us to conclude that based on the data collected, for this kind of problems the Boussinesq hypothesis in the version it was first presented by Boussinesq is not valid. However the results suggest that the hypothesis might be reformulated defining the turbulent viscosity as a second order tensor instead of a scalar value. In this way the problem related to the parallelism between the deviatoric Reynolds stress tensor and the mean rate of strain tensor is overcome. Mathematically this is expressed by:

$$\rho R_{ij}^T - \frac{2}{3}\rho k \delta_{ij} = -2\rho \nu_{T_{ij}} \bar{S}_{ij} \tag{5.7}$$

Verification of this hypothesis however requires more experimental data and a deeper analysis of the Reynolds stress tensor, and goes beyond the aim of the present work.

In conclusion the SPIV results presented within this chapter made it possible to clarify quantify and characterise the generation of turbulence in a system of wake vortices within a scaled model of the ABL. Furthermore it can be preliminarily concluded that if the turbulent viscosity has a real physical meaning in the description of turbulence then for this class of problems it must be a tensor at least of the second order. Finally it means that attempts in simulating the turbulent wake of an aircraft with the classical turbulence viscosity models will eventually fail.

Conclusions

Measurements of simulated aircraft wake vortices in ground proximity were carried out within a *1/200*th scale model of the atmospheric boundary layer in the ABLWT at Cranfield University. A flat plate delta wing was used as a vortex generator since this wing geometry is known to generate a well defined vortex configuration even at low Reynolds numbers. It was designed to obtain a *1/200*th scaled model of the ATTAS VFW614 aircraft wake vortex system based on a well established method for the prediction of the flow over delta wings, Smith [44]. Two different analyses were carried out: (i) a study of the mean flow field and mean motion and decay of the vortex wake, using a five-hole probe and (ii) a study of the fluctuating and intermittent nature of the flow due to turbulence, using a SPIV system.

Concerning the mean flow, Smith [44] was shown to predict the vortex separation with an acceptable error in the range *5-8%*. It was not possible to conclude anything about the vortex core radius and the circulation, which depends on the upstream flow velocity, limited by the boundary layer profile. A typical vortex flow structure was obtained; the vortex was characterised by a concentrated core of high vorticity, high velocity gradients, where pressure and out-of plane velocity drop, which induces a large region of recirculation. A secondary and opposite vorticity distribution was recognised in the regions close to the wing trailing edge. This is probably what remains of the small secondary vortex that naturally develops over delta wings. Moreover the main vortex was shown to present strong asymmetry with respect to both the y axis and the z axis: this was attributed to the interactions with the opposite side vortex and the secondary vortex which lies just beneath it. Because of this, poor results were obtained fitting the experimental data to three vortex models, Vatistas, Lamb-Oseen and Burnham-Hallock (Gerz et al. [21]). The wing was then fixed at three different heights, $0.93B_s$, $1.50B_s$ and $2.24B_s$ and the left-side of the flow was investigated over six vertical planes downstream the wing, assuming symmetry with respect the wing centre-line. The wake vortex was shown to sink behind the wing. The rate of descent was seen to decrease as the initial height of the vortex system approaches the ground. While for $H=1.50B_s$ and $H=2.24B_s$ the descent is quasi-linear for $H=0.93B_s$

it eventually becomes parabolic. At the same time the vortex wake was seen to increasingly diverge. This is assumed to be due to a region of flow acceleration beneath the vortices just above the ground. No vortex rebound was observed, probably due to the rapid decay of the vortices. The circulation and vorticity quickly decay due to the diffusive effects of viscosity and to turbulence. The decay was observed to be approximately linear for all the wing heights tested with a relative high slope which makes it decrease about *50 %* or more in less than eight wing spans downstream. Finally the rate of increase of the core radius was found to be approximately constant at the beginning to reduce and eventually flatten over the x axis for the last planes investigated.

An attempt to model the mean motion of a pair of wake vortices in ground proximity was made by adopting a vortex sheet approximation of the ground. The model replaces each real viscous vortex with a straight infinite vortex filament and the ground with an infinite vortex sheet. The model has shown the descending and diverging motions of the vortex system however it failed in returning the vortex trajectory. The failure was explained by the high non-linearity present in the real viscous flow. The results were compared to Sarpkaya [42] which in ground effect ($z_G/b_0<1.5$) successfully predicts the circulation trend (linear) and the descent trend (parabolic) but fails in returning the exact vertical position of the wake vortex. In contrast out of ground effect, the descent predicted by the current model was successfully fitted to the experimental results better than the circulation. However in both cases a problem related to the definition of the reference velocity for time-space conversion of the model results was identified. Establishing criteria for choosing this parameter, which evidently is connected to a flow characteristic velocity, requires a deeper analysis of the problem. Finally the experimental data was compared to the *four vortex model* (a pair of straight line vortices interacting with an image pair). As previously shown by Barker [4] this model is not able to return an acceptable characterisation of the motion of the vortex wake in ground proximity.

Using SPIV data the instantaneous and fluctuating flow field was analysed. It differs from the mean flow which is assumed to be statistically steady. In the instantaneous field no coherent vortex structure was found but multiple peaks of

vorticity were detected in the vicinity of each vortex. The vortices were found to have a dynamic and intermittent structure that continuously breaks and reforms. The production of turbulent kinetic energy was shown to reach its peak in the vortex core and that is explained by the high velocity gradients in that region. Turbulence intensity was shown to reach up to *80 %* in the x direction in the inner region of the vortices and this is eventually the reason for their enhanced decay. It was also observed that turbulence de-correlates faster in the vortex cores meaning that in those regions the turbulent kinetic energy goes faster to the smallest scales. Finally by analysing the Reynolds stresses it was observed that, as expected, the turbulent viscosity hypothesis, as introduced by Boussinesq (Pope [37]), is not verified for this kind of problem. This led to propose a turbulent viscosity as a second order tensor. This hypothesis seems reasonable but a complete validation requires a much deeper analysis of the turbulent field and further measurements.

Future work

Even though it was not possible to compare the experimental data collected with flight test results in terms of wake evolution the vortex decay obtained appears to be much faster with respect to the wake of a generic commercial aircraft in landing or take off. In fact in the present study the wing model was designed to generate a $1/200^{th}$ geometrically scaled model of the ATTAS aircraft (experimental test case). In this way it was not possible to adequately scale the wake vortices circulation, because of the constraint imposed by the realisation of the Atmospheric Boundary Layer. Even more important, the turbulence parameter (ε^*), which depends on the vortex spacing, the vortex circulation and the turbulence dissipation rate, was relatively high and this is the key factor in wake vortex systems decay. Some of these problems could be overcome in future work by using two different approaches.

1) Utilise a delta wing able to generate a geometrically scaled model of the wake vortex system as done in the present work. But instead of fixing the model within the wind tunnel, this should be launched, with an appropriate system, within the wind tunnel working section at a certain speed so to take into account the relative velocity between the wing and the ground and to obtain the right

value for the circulation. Finally the boundary layer and its dissipation rate should be scaled so to obtain the same turbulence parameter as the full scale wake. In this way the wake model will decay in a similar manner as the real one.

2) Another possible and less expensive way to simulate the wake of a specific aircraft is to design a wing model to obtain circulation and vortex spacing that satisfy the equality between the turbulence parameter in the wind tunnel and in the full scale model. In this way the wake will not be geometrically scaled with respect the real one but the decay of the wake which is dominated by the turbulence parameter should eventually be similar to the full scale one. Even in this case it could be necessary to put in motion the model to have the required value for the circulation.

In conclusion it appears clear that developing a system able to put in motion the wing model used to generate the wake is a requirement for a realistic simulation of this complex phenomenon.

References

[1] Anderson, J. D. (2007), *Fundamentals of aerodynamics*, 4th ed, McGraw Hill Higher Education, New York ; London.

[2] Armitt, J. and Counihan, J. (1968), "The simulation of the atmospheric boundary layer in a wind tunnel", *Atmospheric Environment (1967)*, vol. 2, no. 1.

[3] Atias, M. and Weihs, D. (1984), "Motion of aircraft trailing vortices near the ground.", *Journal of Aircraft*, vol. 21, no. 10, pp. 783-786.

[4] Barker, S. J. and Crow, S. C. (1977), "Motion of two-dimensional vortex pairs ina ground effect.", *Journal of Fluid Mechanics*, vol. 82, no. pt 4, pp. 659-671.

[5] Bernard, P. S. and Wallace, J. M. (2002), *Turbulent flow*, John Wiley & Sons, USA.

[6] Bernon, E. (2007), *Modelling aircraft trailing vortex system within the atmospheric boundary layer* (unpublished MSc thesis), Cranfield University.

[7] Casciola. (Università di Roma La Sapienza), (2005), *Dispense del corso di turbolenza* Roma.

[8] Cook, N. J. (1978), "Wind-tunnel simulation of the adiabatic atmospheric boundary layer by roughness, barrier and mixing-device methods", *Journal of Industrial Aerodynamics*, vol. 3, no. 2-3, pp. 157-176.

[9] Counihan, J. (1969), "An improved method of simulating an atmospheric boundary layer in a wind tunnel", *Atmospheric Environment (1967)*, vol. 3, no. 2.

[10] Crouch, J. (2005), "Airplane trailing vortices and their control", *Comptes Rendus Physique*, vol. 6, no. 4-5, pp. 487-499.

[11] CROW, S. C. (1970), "Stability theory for a pair of trailing vortices", *AIAA Journal*, vol. 8, no. 12, pp. 2173-2179.

[12] Crow, S. C. and Bate Jr., E. R. (1976), "Lifespan of trailing vortices ina turbulent atmosphere", *Journal of Aircraft*, vol. 13, no. 7, pp. 476-482.

[13] de Bruin, A. C., Speijker, L. J. P., Moet, H., Krag, B., Luckner, R. and Mason, S. (2003), "S-Wake - Assessment of Wake Vortex Safety", *Publishable Summary Report*.

[14] DLR (2008), *DLR's research aircraft: VFW 614 / ATTAS*, available at: http://www.dlr.de/en/desktopdefault.aspx/tabid-4689/7762_read-11998.

[15] Dockrill, S. (2006), *Assessment of particle image velocimetry for wing tip flows* (unpublished MSc thesis), Cranfield University.

[16] ESDU (2002), "Strong winds in the atmospheric boundary layer. Part 1: hourly-mean wind speeds.", vol. Data Item 82026.

[17] ESDU (2001), "Characteristics of atmospheric turbulence near the ground. Part III: variations in space and time for strong winds (neutral atmosphere).", vol. Data Item 86010.

[18] ESDU (2001), "Characteristics of atmospheric turbulence near the ground. Part II: single point data for strong winds (neutral atmosphere).", vol. Data Item 85020.

[19] ESDU (1976), "Characteristics of atmospheric turbulence near the ground. Part I: definitions and general information.", vol. Data Item 74030.

[20] Fonti, E. (2008), *Vortici di scia e loro effetti sul traffico aereo* (unpublished BSc thesis), Università di Roma La Sapienza.

[21] Gerz, T., Holzäpfel, F. and Darracq, D. (2002), "Commercial aircraft wake vortices", *Progress in Aerospace Sciences,* vol. 38, no. 3, pp. 181-208.

[22] Greene, G. C. (1986), "Approximate model of vortex decay in the Atmosphere", *Journal of Aircraft,* vol. 23, no. 7, pp. 566-573.

[23] Harvey, J. K. and Perry, F. J. (1971), "Flow field produced by trailing vortices in the vicinity of the ground", *AIAA Journal,* vol. 9, no. 8, pp. 1659-1660.

[24] Hemsch, M. J. and Luckring, J. M. (1990), "Connection between leading-edge sweep, vortex lift, and vortex strength for delta wings", *Journal of Aircraft,* vol. 27, no. 5, pp. 473-475.

[25] Honkan, A. and Andreopoulos, J. (1997), "Instantaneous three-dimensional vorticity measurements in vortical flow over a delta wing", *AIAA Journal,* vol. 35, no. 10, pp. 1612-1620.

[26] ICAO (2006), Wake Vortex Aspects of A380 aircraft, TEC/OPS/SEP (T11/72) – 06-0320.SLG.

[27] Jacquin, L. (2005), "Aircraft trailing vortices: an introduction", *Comptes Rendus Physique,* vol. 6, no. 4-5, pp. 395-398.

[28] Khalifa, O. A. (2008), *Wingtip Vortices in Nature and their Potential Application in Aircraft* (unpublished MEng thesis), Imperial College London.

[29] Lamb, M. (1945), *Hydrodynamics,* 6th ed, Dover, New York.

[30] Lowson, M.,V. (1989), "Visualization measuremnts of vortex flows", *AIAA*, , no. 0191.

[31] Mathieu, J. and Scott, J. (2001), "An introduction to turbulent flow", *Physics Today*, vol. 54, no. 9, pp. 53.

[32] Meunier, P., Le Dizès, S. and Leweke, T. (2005), "Physics of vortex merging", *Comptes Rendus Physique*, vol. 6, no. 4-5 SPEC. ISS., pp. 431-450.

[33] Miau, J. J., Kuo, K. T., Liu, W. H., Hsieh, S. J., Chou, J. H. and Lin, C. K. (1995), "Flow developments above 50-deg sweep delta wings with different leading-edge profiles", *Journal of Aircraft*, vol. 32, no. 4, pp. 787-794.

[34] Orlandi, P. (2007), "Two-dimensional and three-dimensional direct numerical simulation of co-rotating vortices", *Physics of Fluids*, vol. 19, no. 1.

[35] Orlandi, P. (1990), "Vortex dipole rebound from a wall", *Physics of Fluids A*, vol. 2, no. 8, pp. 1429-1436.

[36] Panofsky, H. A. and Dutton, J. A. (1984), "Atmospheric turbulence: models and methods for engineering applications."

[37] Pope, S. B. (2000), *Turbulent Flows*, Sixth ed, Cambridge University Press, USA.

[38] Proctor, F. H., Hamilton, D. W. and Han, J. (2000), "Wake vortex transport and decay in ground effect: Vortex linking with the ground", *AIAA Paper*, vol. 2000, no. 757, pp. 14.

[39] Puel, F. and de Saint Victor, X. (2000), "Interaction of wake vortices with the ground", *Aerospace Science and Technology*, vol. 4, no. 4, pp. 239-247.

[40] Raffel, M., Willert, C. E., Wereley, S. T. and Kompenhans, J. (2007), *Particle Image Velocimetry*.

[41] Rossow, V. J. (1999), "Lift-generated vortex wakes of subsonic transport aircraft", *Progress in Aerospace Sciences*, vol. 35, no. 6, pp. 507-660.

[42] Sarpkaya, T. (2000), "New model for vortex decay in the atmosphere", *Journal of Aircraft*, vol. 37, no. 1, pp. 53-61.

[43] Schell, I., Özger, E. and Jacob, D. (2000), "Influence of different flap settings on the wake-vortex structure of a rectangular wing with flaps and means of alleviation with wing fins", *Aerospace Science and Technology*, vol. 4, no. 2, pp. 79-90.

[44] Smith, J. H. B. (1966), "Improved calculations of leading-edge separation from slender delta wings", *RAE TR-66070*.

[45] Stein, S. (2009), *Modelling aircraft trailing vortices systems within the atmospheric boundary layer* (unpublished MSc thesis), Cranfield University.

[46] Taylor, G. S., Schnorbus, T. and Gursul, I. (2003), "An Investigation of Vortex Flows over Low Sweep Delta Wings", *AIAA-2003-4021*.

[47] Thomson, D. H. (1975), A water tunnel study of vortex breakdown over wings with highly swept leading edges, Aerodynamics Note 356, Australian Defence Scientific Service ARL.

[48] Townsend, A. A. (1961), "Equilibrium layers and wall turbulence", *Journal of Fluid Mechanics Digital Archive,* vol. 11, no. 01, pp. 97.

[49] Traub, L. W., Moeller, B. and Rediniotis, O. (1998), "Low-Reynolds-number effects on delta-wing aerodynamics", *Journal of Aircraft,* vol. 35, no. 4, pp. 653-656.

[50] Treaster, A. L. and Yocum, A. M. (1979), "Calibration and application of five-hole probes.", *ISA transactions,* vol. 18, no. 3, pp. 23-34.

[51] Tricomi, F. G. (1985), *Integral Equations,* first ed, Dover, United States of America.

[52] TSI (Trust Science Innovation), (2007), *Insight 3G, Data Acquisition, Analysis, and Display Software Platform.*

Appendix A - Further Five-Hole Probe Results

A.1 Velocity components

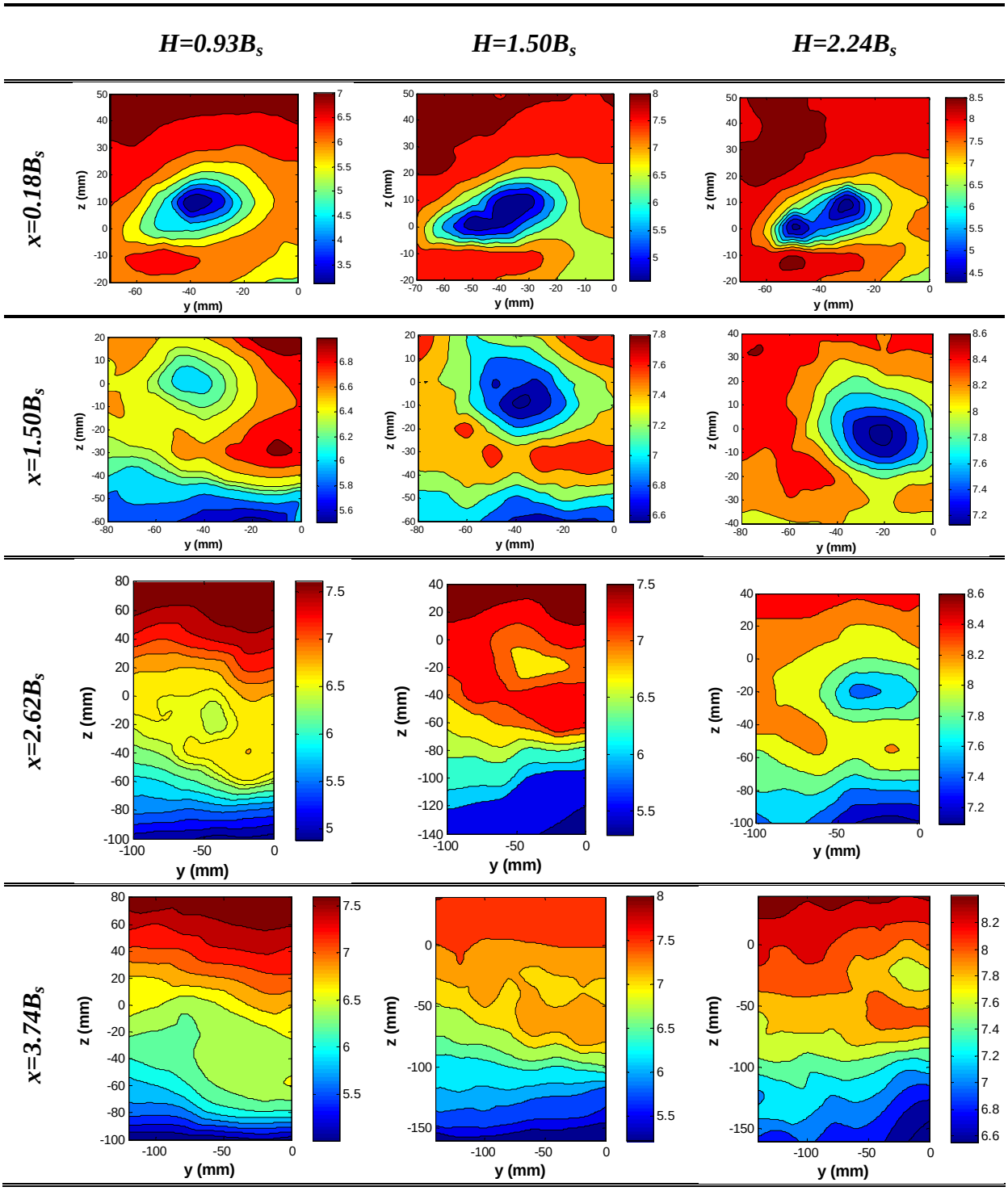

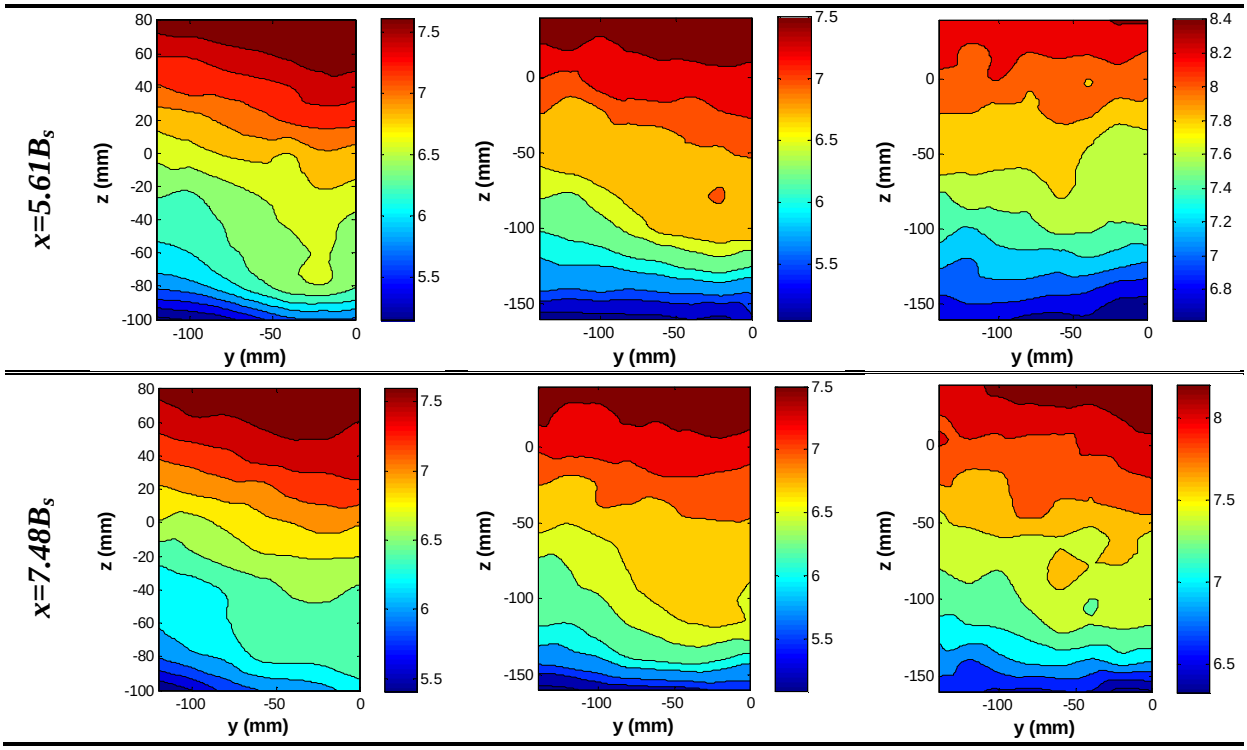

Table 16 Out-of-plane velocity (u) for three wing heights over several planes downstream the wing

Table 16 shows the distribution of the velocity component along x (u) over six vertical planes downstream the wing for three wing heights. It is clear from the plots how the vortex structure deforms the Atmospheric Boundary Layer profile in the x direction. A region of low speed correspondent to the core region of the vortex creates. As we move downstream along the vortex stream-tube (looking at the vortex as a three-dimensional steady flow) the vortex decays under the action of the shear stress due to the viscosity. So the whole flow tends to a stable condition it has upstream the wing. Since upstream the flow presents a velocity profile along z (the ABL) it will tend to the same condition. As the vortex decays the gap in velocity between the vortex core and the outer flow decreases until under the action of the shear stress in x direction the region of low velocity disappears leaving a region of highly stratified flow. The main observable difference between the three wing heights is that the vortex lasts longer at higher heights so does the region of low speed. In any case downstream $x=3.74B_s$ no a clear vortex structure is observable anymore.

Table 17 shows the velocity component in span-wise direction (v) for the three wing heights tested. As analysed in Chapter 3 the flow shows acceleration in the region beneath the vortices. A relatively high speed compared to the other regions is found between the vortex

and the ground. Eventually this region is the engine of the vortex lateral displacement. Interesting to notice is that the same asymmetry is present for all the heights tested, so is a significant diverging phase in the vortex trajectory which violates the definition of ground effect given by Sarpkaya and Proctor.

	$H=0.93B_s$	$H=1.50B_s$	$H=2.24B_s$
$x=0.18B_s$	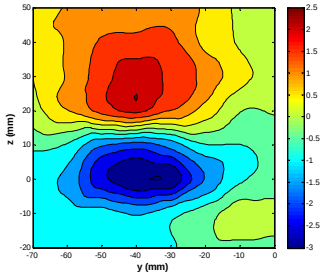	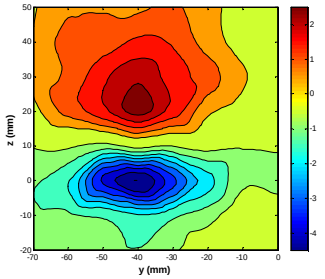	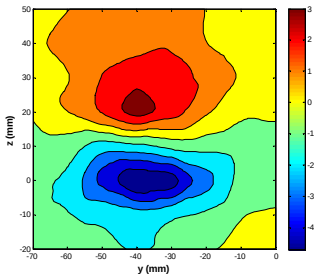
$x=1.50B_s$	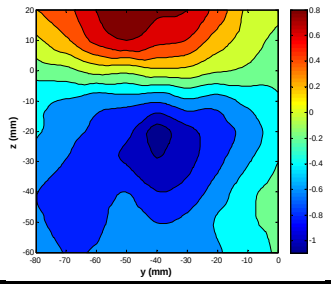	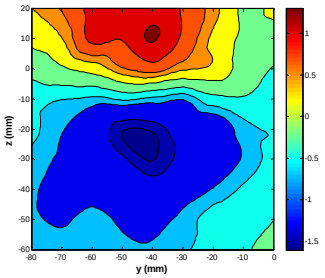	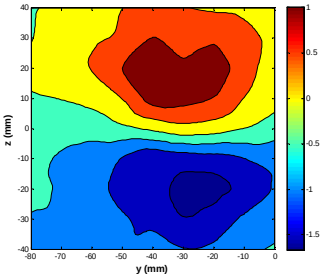
$x=2.62B_s$	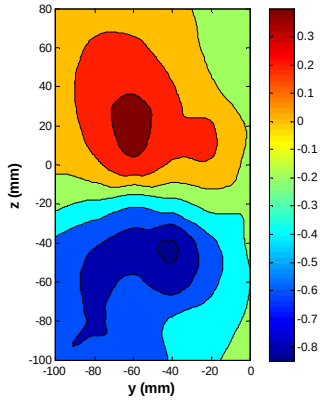	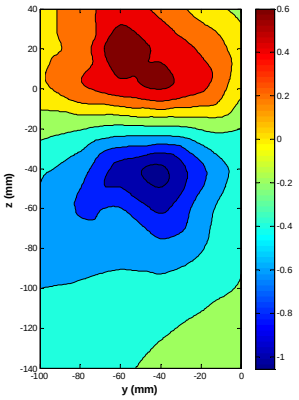	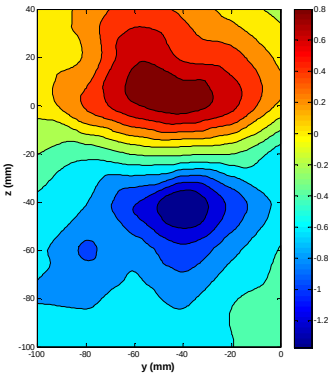
$x=3.74B_s$	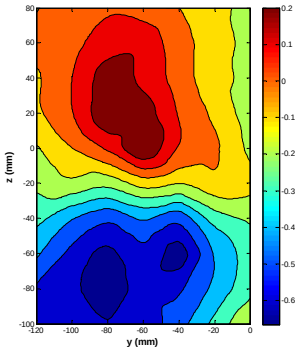	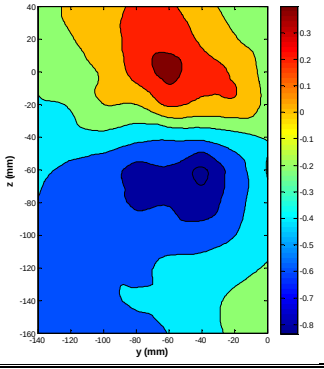	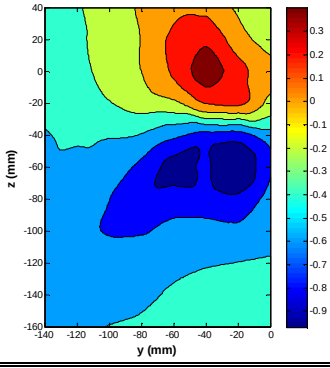

$x=5.61B_s$	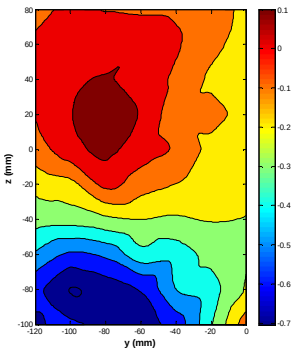	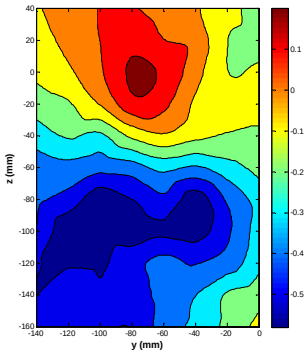	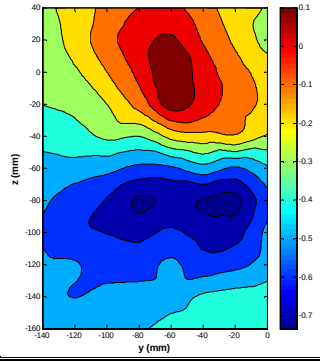
$x=7.48B_s$	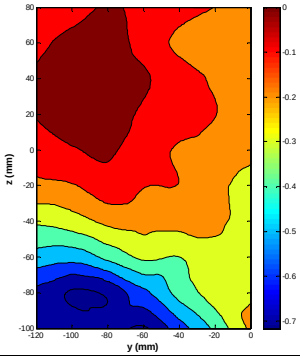	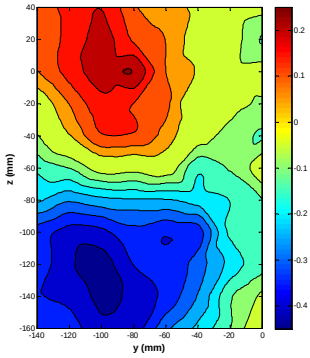	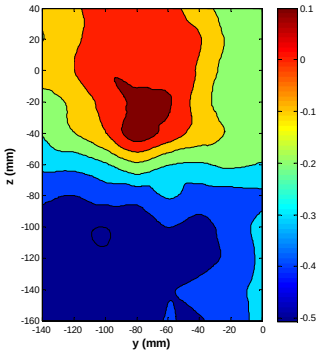

Table 17 Velocity component along y (v) for three wing heights over six different planes

A.2 Static pressure

Table 18 presents the static pressure coefficient map over six planes downstream the wing for the three wing heights tested. Again the vortex well marked by a peak of low Cp_{static} in the near field of the wing, for instance see plane $x=0.18B_s$ for all the heights, becomes difficult to be recognized as the planes get further from the wing trailing edge, eventually impossible. Although a clear region of low pressure, correspondent to the vortex core, quickly disappears, the plots of Table 18 show an elongated region of high Cp_{static} starting from the ground and approximately linking to the descending vortex. This region, again, might be a clear explanation of the vortex diverging in close ground effect and might be the primary cause of the formation of a secondary vortex of opposite vorticity over the ground.

	H=0.93B_s	***H=1.50B_s***	***H=2.24B_s***
x=0.18B_s	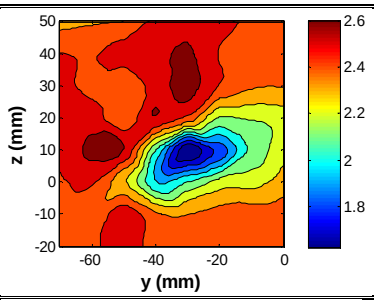	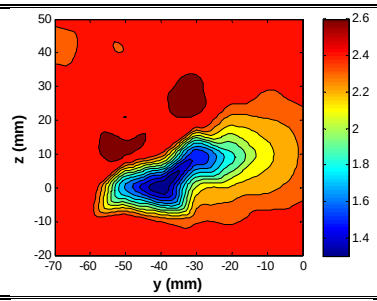	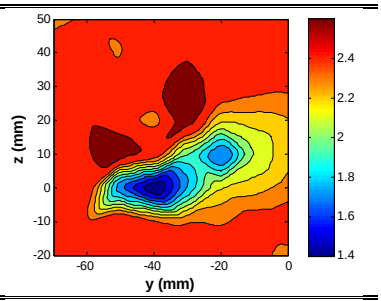
x=1.50B_s	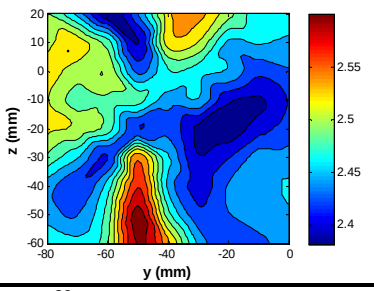	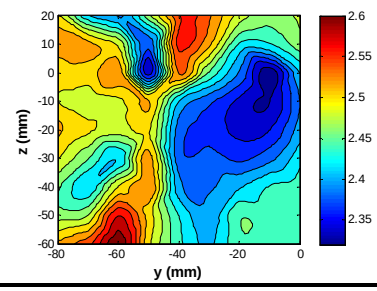	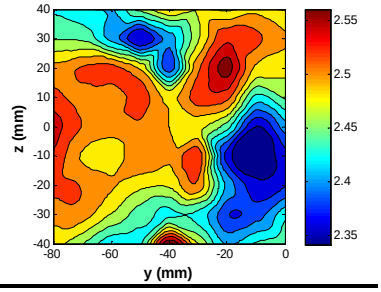
x=2.62B_s	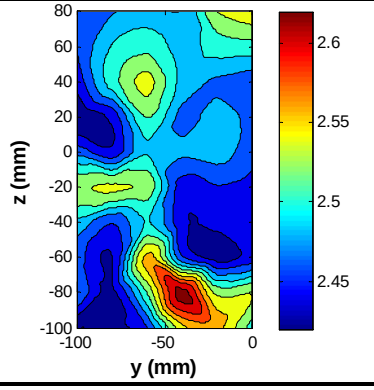	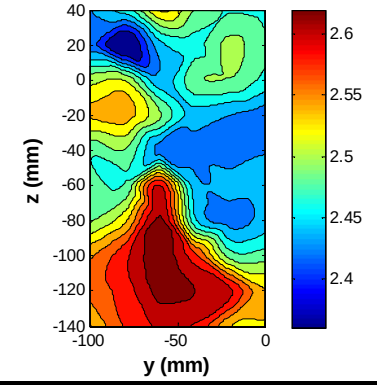	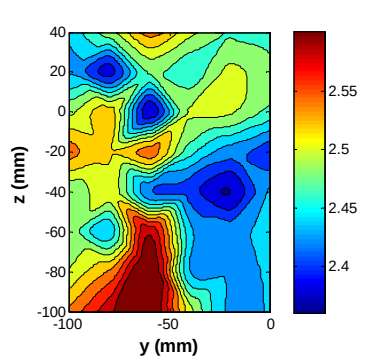

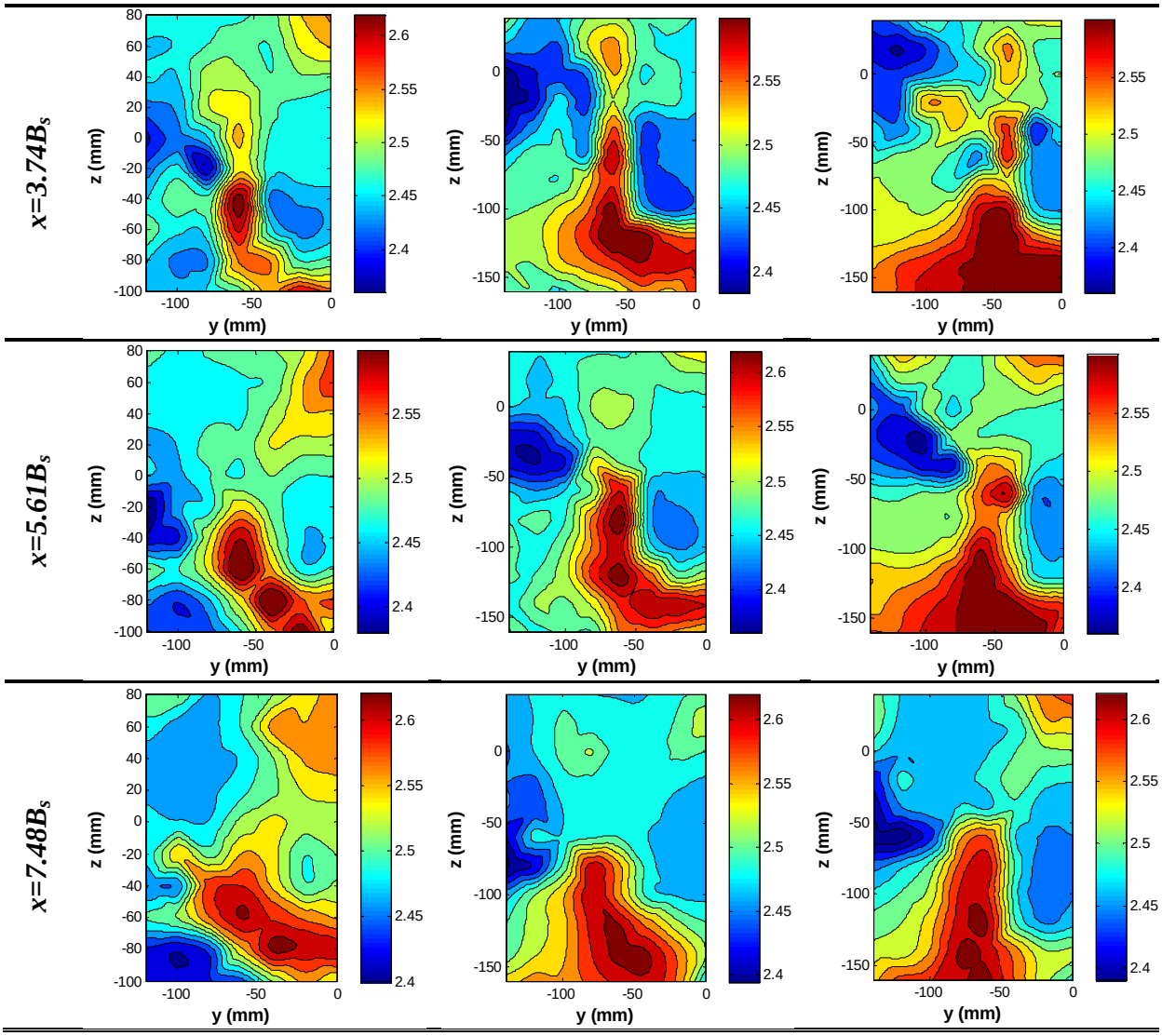

Table 18 Static pressure coefficient for three wing heights over several vertical planes downstream the wing

Appendix B - Further SPIV Results

B.1 Turbulence intensity: $x=3.74B_s$

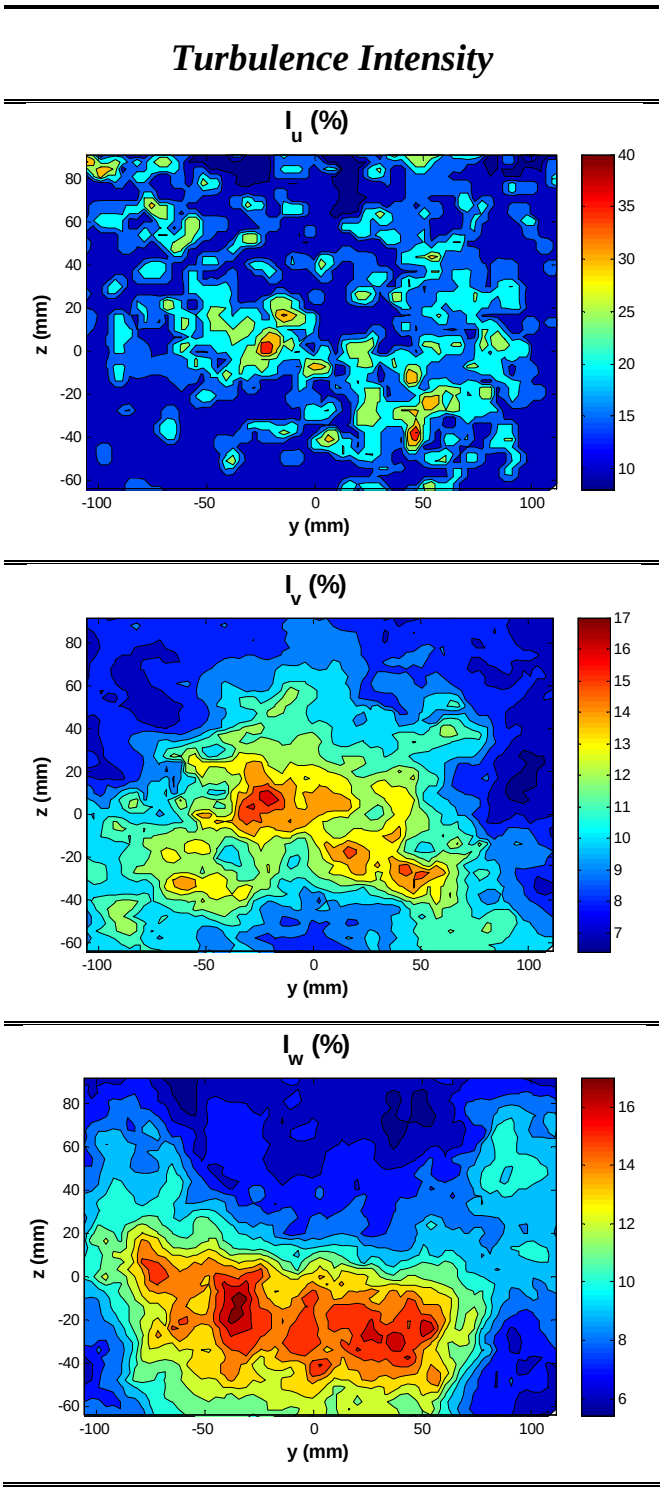

Table 19 Turbulence intensitiy along x (top), along y (middle) and along z (bottom)

B.2 Lateral correlation lengths: $x=0.18B_s$

Lateral Correlation Lengths	
y direction	***z direction***
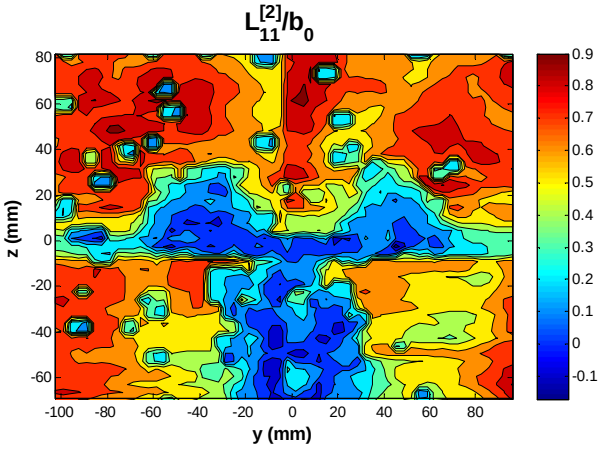	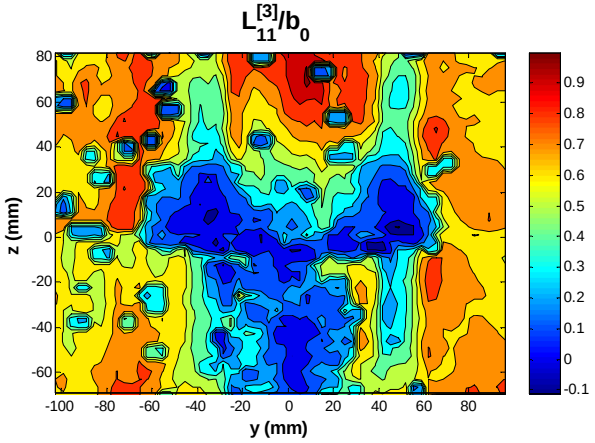
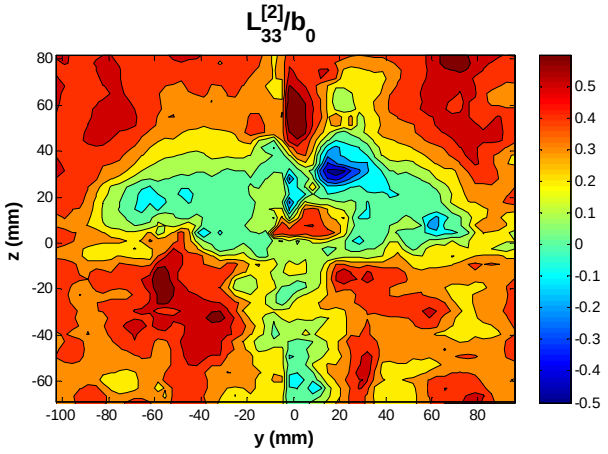	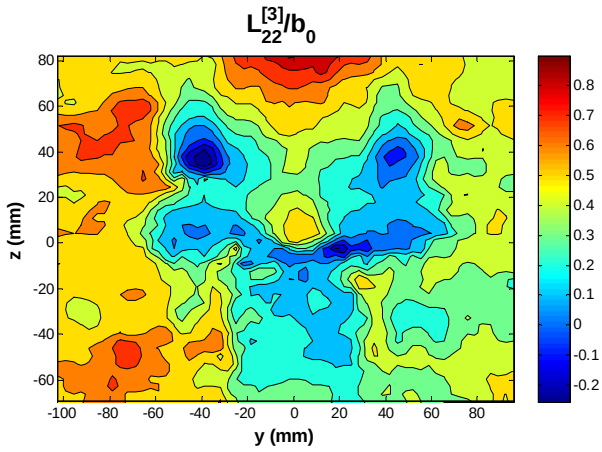

Table 20 Lateral correlation lengths for wing height $H=1.50B_s$ over the plane located at $x=0.18B_s$

B.3 Reynolds stresses: $x=0.18B_s$

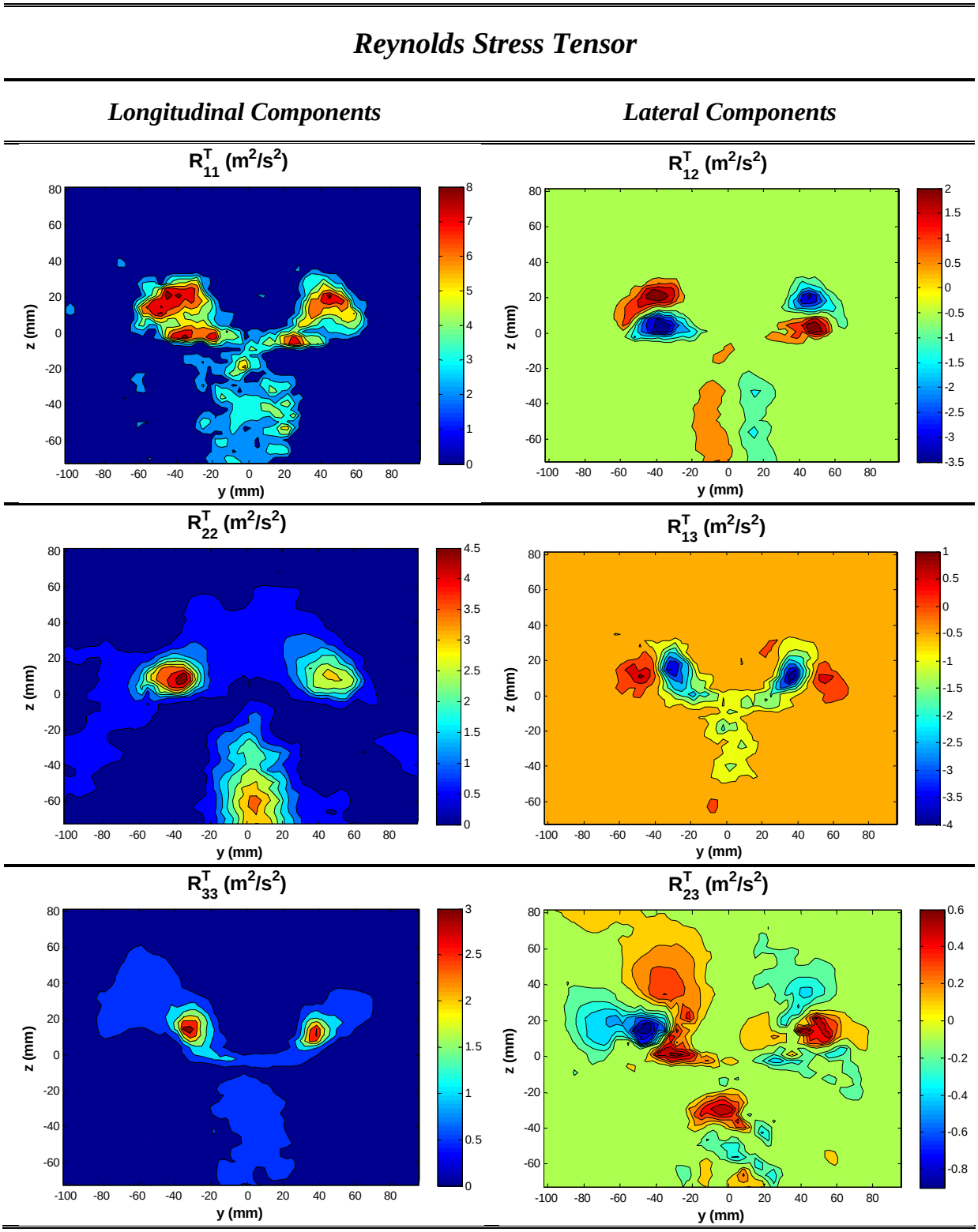

Table 21 Reynolds stresses for wing height H=1.50B_s over the plane located at x=0.18B_s